Stony Brook University

Numerical modeling of blood flow in prosthetic heart valves and cardiovascular pathologies

A Dissertation Presented

by

Yared Alemu

to

The Graduate School

in Partial Fulfillment of the

Requirements

for the Degree of

Doctor of Philosophy

in

Biomedical Engineering

Stony Brook University

May 2010

Stony Brook University

The Graduate School

Yared Alemu

We, the dissertation committee for the above candidate for the

Doctor of Philosophy degree, hereby recommend

acceptance of this dissertation.

Danny Bluestein, Ph. D., Dissertation Advisor
Professor of Biomedical Engineering

Yi-Xian Qin, Ph. D., Chairperson of Ph.D. Defense Committee
Professor of Biomedical Engineering

Shmuel Einav, Ph. D.
Professor of Biomedical Engineering, CEAS Associate Dean of Research

Yuefan Deng, Ph. D.
Professor Applied Mathematics & Statistics

This dissertation is accepted by the Graduate School

Lawrence Martin
Dean of the Graduate School

Abstract of the Dissertation

Numerical modeling of blood flow in prosthetic heart valves and cardiovascular pathologies

by

Yared Alemu

Doctor of Philosophy

in

Biomedical Engineering

Stony Brook University

2010

Despite the many advances in our understanding of cardiovascular diseases and how to diagnose and treat them, they are still the leading cause of death and disability in the Western World. Onset and progression of these diseases is due to interplay between pathologic flow conditions and vessel remodeling altering vessel geometries and composition. Advances in numerical simulation techniques and improvements in computational power have opened new avenues to investigate challenging pathological flow problems that underlie and characterize cardiovascular diseases.

Mechanical heart valves (MHV) represent pathologic flow conditions common in cardiovascular prosthetic devices. Those result in platelet damage leading to thrombus formation and thromboembolism, which are major impediments to these devices. Numerical simulations were conducted to study platelet damage resulting by pathological flow patterns. The simulations included unsteady Reynolds averaged Navier Stoke (URANUS) and highly resolved direct numerical simulations (DNS) formulations. The thrombogenic potential of different MHV designs was evaluated from the sum of the product of stress and exposure time, determining platelet stress accumulation. Platelet cumulative damage due to repeated passages through the valve was also studied.

Vulnerable plaques (VP) and abdominal aortic aneurysms (AAA) are examples of cardiovascular diseases that are driven by pathologic vessel geometries and compositions and compromised hemodynamics. Blood vessel

integrity disruption and rupture in these diseases can lead to stroke, heart attack, and death. Numerical studies of their rupture risk was based on incorporating anisotropic vessel tissue material properties, and inclusion of calcification and intraluminal thrombus in patient specific geometries extracted from clinical imaging modalities, using fluid structure interaction (FSI) simulations to examine risk of rupture due to the contribution stresses and vessel tissue deformation.

Advanced numerical tools that were developed and employed to study the conditions present in pathological blood vessels and in flows through prosthetic heart valves PHV are presented. These studies tackle highly complex cardiovascular disease processes using sophisticated engineering tools, adding to our understanding of biomechanical problems characterized by the interaction of blood flow with cardiovascular devices and pathological vessel geometries. This can aid optimizing the design of future cardiovascular devices and to augment clinical diagnostics of cardiovascular pathologies.

Table of Contents

List of Symbols

μ	viscosity
U	velocity
ρ	density
$\mathbf{V}$	velocity vector
δ_{ij}	kronecker delta
$\mathbf{F}$	force
t	time
p	pressure
v	velocity
λ	second viscosity coefficient
$\tau' = \tau_{ij}$	stress tensor
u	velocity
$\overline{u}$	mean velocity component
u'	fluctuating velocity component
k	turbulence kinetic energy
μ_t	turbulent viscosity
α^*	turbulent viscosity correlation coefficient
ω	specific dissipation rate
Γ_ω	effective diffusivity of ω
Γ_k	effective diffusivity of k
G_k	generation of turbulence kinetic energy
Y_k	dissipation of k due to turbulence
S_k	user-defined source terms
G_ω	generation of ω
Y_ω	dissipation of ω due to turbulence
S_ω	user-defined source terms

u_p	velocity of particle
F_D	particle drag force
F_x	additional particle acceleration
C_D	particle drag coefficient
d_p	particle diameter
ρ_p	density of particle
σ	scalar stress
$\dot{D}$	damage rate
D	damage
SA	stress accumulation
$t_{\exp}$	exposure time
$\dot{\sigma}$	stress rate
Δt	time step
M	mass matrix
C	damping matrix
K	stiffness matrix
$\ddot{\mathbf{U}}$	acceleration vector
$\dot{\mathbf{U}}$	velocity vector
$\mathbf{U}$	displacement vector
$\mathbf{V_g}$	grid velocity
W	strain energy
$W_{isotropic}$	isotropic component of strain energy
$W_{anisotropic}$	anisotropic component of strain energy
C_1	material constant
C_2	material constant
D_1	material constant
I_1	first invariant of Cauchy–Green deformation tensor
I_2	second invariant of Cauchy–Green deformation tensor

k_1	material constants
k_2	material constants
J_4	forth invariant of Cauchy–Green deformation tensor
J_6	sixths invariant of Cauchy–Green deformation tensor
$Strength$	strength of the aneurysmal wall
ILT	ILT thickness
$NORD$	local diameter normalized to non-aneurysmal aortic diameter
$HIST$	family history of the patient
SEX	sex of the patient
RPI	rupture potential index
μ_k	Kolmogorov length scale
V	characteristic velocity
ε	characteristic length

List of Figures

List of Tables

List of publications

- Yin, W., **Y. Alemu**, K. Affeld, J. Jesty, and D. Bluestein, “Flow-induced platelet activation in bileaflet and monoleaflet mechanical heart valves.” Annals of Biomedical Engineering, 2004. 32(8): p. 1058-66.
- Raz, S., S. Einav, **Y. Alemu**, and D. Bluestein, “DPIV prediction of flow induced platelet activation-comparison to numerical predictions.” Annals of Biomedical Engineering, 2007. 35(4): p. 493-504.
- **Alemu, Y.** and D. Bluestein, “Flow-induced platelet activation and damage accumulation in a mechanical heart valve: numerical studies.” Artificial Organs, 2007. 31(9): p. 677-88.
- Bluestein, D., **Y. Alemu**, I. Avrahami, M. Gharib, K. Dumont, J.J. Ricotta, and S. Einav, “Influence of microcalcifications on vulnerable plaque mechanics using FSI modeling.” Journal of Biomechanics, 2008. 41(5): p. 1111-1118.
- Ricotta, J.J., J. Pagan, M. Xenos, **Y. Alemu**, S. Einav, and D. Bluestein, “Cardiovascular disease management: the need for better diagnostics.” Med Biol Eng Comput, 2008. 46(11): p. 1059-68.
- Rissland, P., **Y. Alemu**, S. Einav, J. Ricotta, and D. Bluestein, “Abdominal Aortic Aneurysm Risk of Rupture: Patient-Specific FSI Simulations Using Anisotropic Model.” Journal of Biomechanical Engineering, 2009. 131(3): p. 031001.
- Xenos, M., G. Girdhar, **Y. Alemu**, J. Jesty, M. Slepian, S. Einav, D. Bluestein, “Device Thrombogenicty Emulator (DTE) − Design optimization Methodology for Cardiovascular Devices: A Study in Two Bileaflet MHV Designs”, Journal of Biomechanics, (accepted 2010)
- **Alemu, Y.**, G. Girdhar, M. Xenos, J. Sheriff, J. Jesty, S. Einav, D. Bluestein, "Design Optimization of a Mechanical Heart Valve for Reducing Valve Thrombogenicity – a Case Study with ATS valve" ASAIO, (accepted 2010)
- Xenos, M., S. Rambhia, **Y. Alemu**, S. Einav, N. Labropoulos, A. Tassiopoulos, J. Ricotta, D. Bluestein, "Patient Based Abdominal Aortic Aneurysm Rupture Risk Prediction with Fluid Structure Interaction Modeling" Annals of Biomedical Engineering, (under revision)

Acknowledgments

I would like to thank my advisor Prof. Danny Bluestein for his continued guidance and support throughout my graduate research. Working with him has given me the privilege to work on some of the most interesting and challenging topics in biomedical engineering.

I also would like to thank past and present members of the lab. I have found research to be collaborative effort and not work of one person. It has been pleasure to know and work with such great group of people.

I would like to thank my parents Alemu Sida and Almaz Worgessa. Their continued encouragements and prayers as well as my siblings and friends have been great help during these years. I also would like to thank my fiancée Loule Gebremedhin for her prayers and words of encouragement.

I thank God for the grace He has given me and using these years to shape my life.

Introduction

Cardiovascular diseases are one of the leading causes of death in the industrialized world. These diseases can be broadly categorized into pathological flow conditions affecting blood and others affecting pathological blood vessel geometries, with strong interplay between the blood and vessel geometry.

The studies presented in the dissertation focus on blood flow in the aortic heart valve, coronary artery and the abdominal aorta. Numerical simulation tools were used to explore pathological flow conditions present in prosthetic heart valve and the interaction of blood flow with pathological vessel components in the coronary artery and abdominal aorta.

Numerical simulations of pathologic blood flow through mechanical heart valve were designed to study the resulting platelet stress damage. These studies employed highly resolved computational domains to simulate conditions in mechanical heart valves. Stresses experienced by large population of platelets were used in evaluating valve performance. Platelet stress damage on individual platelets due their repeated passage through the valve geometry was also calculated.

Fluid structure interaction simulations were used to study the risk of rupture from the contribution of flow to vessel tissue deformation and stresses. These studies were conducted to assess the rupture risk of vulnerable plaques and abdominal aortic aneurysms. These incorporated anisotropic vessel tissue properties, calcification and intraluminal thrombus in patient specific geometries extracted from clinical imaging modalities.

Cardiovascular pathologies that are driven by pathological blood flow conditions were addressed in the dissertation according to the following specific aims, addressed in subsections A and B of section III:

Specific Aim: Development of numerical model to quantify flow induced platelet damage, based on the results of numerical simulation.

Specific Aim: Numerical modeling of vulnerable plaque and abdominal aortic aneurysms in order to assess their risk of rupture.

The tools used and developed for these studies can aid in optimizing the design of future cardiovascular devices and to augment clinical diagnostics of cardiovascular pathologies.

I. Background and Significance

A. Mechanical heart valves (MHV)

Mechanical heart valve implants are one of the options used to treat complications caused by heart valve diseases. These diseases result in pathologic blood pressure and flow rates. These pathologic flow conditions, if not treated, can lead to further complications and death. Some of these diseases that require mechanical heart valve implants are aortic stenosis, aortic insufficiency, drug-induced valve disease and aortic valve sclerosis [1-2].

In severe cases, mechanical heart valves are used to treat these conditions. About 100,000 patients in the US receive mechanical heart valves (MHV) per year [3]. Since their introduction in the 1950s, MHV models have gone through many design changes. The first implanted prosthetic valve was a ball and cage design developed in 1951 which was placed in descending aorta of patients with aortic insufficiency [4]. Following the ball and cage design, other valves were developed to overcome its limitations. These limitations tend to distort the dimensions of the ball, critical valve component, reducing valve performance [5]. These efforts led to the development of nontilting disk valves (1962 – 1973), tilting Disk valves (1963 – 1977), bileaflet valves (1963 – 1976), tissue and polymeric valves (1960s) [4, 6].

As mentioned earlier, the limitations of the ball and cage design were one of the motivations that led to the search for alternative heart valve designs. Materials used in the ball and cage valve were susceptible to ball damage, cracks and to being “imbibed/filled” lipid resulting in dimensional distortions [4]. Later valve designs attempted to address these problems by modifying valve configurations and through the utilization of biocompatible materials [7]. Pyrolite carbon, standard material used in constructing MHVs from 1969 onward, was originally developed as a seal on nuclear fuel rods in the 1960s. It is composed of carbon and various ceramics which provides the hardness and biocompatibility

found suitable for MHVs [4-5]. Even with these improvements some problems first encountered in the ball and cage design still persist.

Main problem associated with mechanical heart valves is their thrombogenicity. By utilizing biocompatible materials and geometry optimized for hemodynamic performance, current generation of mechanical heart valves are great improvement over their predecessors [5, 8]. However, elevated risk of thrombogenic potential is still the major persistent problem in mechanical heart valves [9]. To overcome this problem, patients receiving mechanical heart valve implants are placed on lifelong anticoagulant medication. While this regimen does not eliminate the risk of thrombogenic complications, it results in increased risk of uncontrolled bleeding [1, 10].

This thrombogenic complication is due to the action of activated platelets that initiate the clot formation process as the result of flow conditions through MHV. Although the focus of this work is platelet activation due to mechanical stresses, biochemical factors are also known to result in platelet activation [11]. From constant stress experiments, the relation between stress and exposure time that results in hemolysis and in platelet activation has been well established and is referred to as the Hellums criterion [12]. However, under physiological flow conditions including flow through MHVs, platelets are exposed to varying stress levels and prediction based on constant shear stress assumption may not be applicable [13-14]. For blood flow MHV, the contribution of the Reynolds averaged turbulent stresses, based on the fluctuating component of velocity, may become significant in platelet activation and aggregation [15]. In addition to turbulence, repeated passage through the valve expose blood constituents to cyclic loading which may result in additional cell damage that will precipitate activation [16-17].

The blood coagulation process involves platelet activation and can be initiated by various mechanical or chemical factors. In the case of blood flow through MHV, the non–physiologic flow conditions have been shown to be responsible in activating platelets in the absence of chemical agonists [18]. These non–physiologic flow conditions that can result in platelet activation

include adverse pressure gradients, flow separation, and vortex formation known to be present in pathologic flow conditions [19].

When platelets experience these flow conditions, they activate and change their morphology to extend pseudopodia [20]. After activation, they start adhering to surfaces and aggregate promoted by agonists secreted from their α–granules [21-22] and by fibrinogen that binds to the platelet surface via GPIIb/IIIa [23]. Thrombin is generated when factor Xa is combined with cofactor Va on the surfaces of activated platelets expressing anionic phospholipids [24]. The resulting prothrombinase complex cleaves the soluble fibrinogen into insoluble fibrin- the clot material that may lead to thromboembolic complications.

Various components involved in platelet activation and their participation in thrombus formation process are described above. This process of platelet activation can be initiated by stresses generated by flow through MHVs. Measured turbulent stresses in MHV leakage flow [25] indicated that turbulent eddies have similar dimensions as platelets which can result in platelet activation [26]. Platelets activate at shear stress value of 100–300 dyn/cm^2 [27-28]. These flow patterns can stimulate the coagulation cascade and initiate thrombosis [11, 25, 29]. Activated platelets with long residence time in these flow regions may aggregate, leading to free emboli formation [29].

The previous paragraph shows flow stresses contribute to platelet activation. However, the level of stress that may lead to platelet activation has not been settled. Because measuring the stresses experienced by an individual platelet within a bulk flow conditions is a challenging task. In this work, the flow results from the numerical simulations are used to determine the experiences of individual platelets that transverse the different regions of the valve.

3D simulations show the effects of transient flow past MHV and the wake dynamics [30-33]. However, these simulations use laminar flow assumption which negates the presence of turbulence and its contribution thrombogenic potential of MHV. Consideration of turbulent stresses is essential because these may exceed laminar stresses at certain phases of the cardiac waveform and are critical in activating the hemostatic system [13].

Over the years numerical simulations have been used in several investigations to understand the various features of flow through mechanical heart valves. The earliest studies were conducted in 2D ideal MHV geometries. With advances in computational power and algorithms, consideration of realistic 3D MHV geometries with moving boundary conditions is now possible. Current numerical studies are performed on valves in realistic aortic root geometry as well as in experimental test geometries. As mentioned earlier, flow in MHV is dynamic involving various complex phenomenon including intermittent turbulence. In addition to incorporating geometrical intricacies of the valve, calculations have been conducted using laminar and Reynolds averaged turbulence model descriptions of the flow. Valvular flows are dominated by intermittent turbulence in the transition range rendering most turbulence models (which are based on isotropic turbulence assumption) incapable of describing the flow [34]. Continuing advances in computational power and algorithm have made it possible to perform large eddy simulations that capture the larger turbulent eddies and direct numerical simulation (DNS) attempting to capture the smallest turbulence eddies. Current studies focus their attention on DNS of the valve region trying to capture the small scale flow near the valve geometry, while other studies model the rotational motion of the leaflet during cardiac cycle [35-36].

During the cardiac cycle, these valves open and close requiring moving boundaries for complete numerical representation. This requires innovative ways to account for leaflet motion, the moving part of the valve, throughout the cycle. Investigators have used overset mesh [37-38] (interpolating between mesh attached to the leaflet and background mesh for the valve geometry), level set method [39] (fixed mesh with scheme to capture the evolving leaflet-fluid interface), and body fitted mesh requiring incremental remeshing dictated by leaflet motion [35, 40-41]. All of the above techniques can be uncoupled or coupled FSI simulations. Coupling relates to the ability of the leaflet motion, the solid structure, to influence the fluid flow that caused its motion [35, 40, 42]. Pre-generating intermediate leaflet positions has also been used [43].

From these studies clearer picture of the flow conditions present in the valve throughout the cardiac cycle has emerged. For the forward flow phase of bileaflet valves, three main jets and complex vortices were observed downstream of the leaflet [33, 37, 44-45]. During the regurgitant flow phase, jet flows at the various gaps (valve-housing and b-datum gap) were observed [25, 46]. In the case of flow through bileaflet valves, three main jets were observed [19, 33, 44]. In addition to flow conditions, the corresponding leaflet motion is shown to have flutter when leaflet are fully open and experiences slight rebound during closing [43, 47-48]. These results into the flow conditions and leaflet motion have been correlated with numerous experimental observations [19, 35, 49-50].

Numerical studies of flow through MHV can be used to quantify the amount of flow induced blood damage. As presented earlier, no-physiologic flow stresses are present in MHV flows which can induce damage on blood components. These works can be divided into two, quantifying the stresses experienced by red blood cells (RBC) and platelets, quantifying platelet damage that may lead to RBC and platelet damage. Stress accumulation studies used linear and power law product of stress and exposure time to determine platelet stress accumulation [16]. Estimation of platelet damage is the focus of this work which attempts to relate the stresses and exposure time to the resulting platelet damage.

In addition to numerical simulations of flow through MHV, there have been various mathematical models to describe damage to blood components. Many investigators have looked into Red Blood Cells (RBC) damage (hemolysis) as compared to the focus of this work which is platelet damage (activation). Mathematical correlations were developed between hemoglobin release due to hemolysis, shear stress and exposure time [51-52]. Based on percent release of dehydrogenase (LDH), similar models were also developed for platelet activation [51]. These models satisfy certain experimental observations have been shown to underestimate cell damage [52-53].

In physiological flow conditions, blood is exposed to varying stress levels which differ from these ideal cases of constant stress [52-53]. The magnitude

stress accumulation, the combined effect of the fluctuating stresses present in physiological flows and exposure time, which results in platelet activation is not known. In addition, platelet activation needs to consider the role of turbulence that may be significant in blood flows through devices [54]. Additional parameter that needs to be considered is the contribution of repeated passes that may result in platelet damage [34, 55].

B. Vulnerable Plaques (VP) and Abdominal Aortic Aneurysms (AAA)

Atherosclerotic cardiovascular diseases are major cause of death in developed countries resulting in half million deaths per year in the US alone [56-61]. Atherosclerotic lesions may develop in different parts of the arterial network. These lesions are deposits of fat and cellular debris below the intimal layer of the blood vessel which may result in constricting blood flow through the vessel. In the cases that are considered below, the lesions may rupture to release their content into blood stream (in VP) to cause stroke or the vessel wall may fail resulting in blood loss (in AAA).

Vulnerable plaque*.* One of the blood vessels susceptible to the development of atherosclerotic lesions is the coronary artery. These lesions contain fat and cellular debris below the intimal layer which may rupture releasing the content into the blood stream resulting in clot that may lead to stroke and even death. Plaques with less than 70% constriction do not present symptoms but make up 90% of the ruptured plaques that result in death [62]. These are vulnerable plaques which are at higher risk of rupture, mildly restricted vessels with larger necrotic core and greater concentration of macrophages [59, 62-72].

The initiation and development of atherosclerotic lesions is related to endothelial dysfunction. Participating chemical factors involved in this process include, smoking, high blood concentration of low density lipoproteins (LDL) and diabetes. Mechanical factors, that disrupt blood flow conditions, indicate sites susceptible to the development of atherosclerotic lesions [73]. These sites are near the arterial branch points of the carotid artery sinus, coronary artery,

abdominal aorta and superficial femoral arteries [74-75]. Of these numerous sites susceptible to the development of atherosclerotic lesions, this document will concentrate in numerical study of the conditions present in the coronary artery and abdominal aorta.

In coronary artery favorable chemical and mechanical factors initiate endothelial dysfunction which results in the permeability of endothelium to lipoproteins, leukocytes, and other inflammatory mediators [71-72, 76-79]. Activated endothelial cells also recruit monocytes and T lymphocytes to the vessel wall [80]. T lymphocytes and lipoproteins migrate from blood to within the intima stimulate the expression of monocyte receptors for absorbing oxidized lipoproteins [77-79, 81]. After absorbing modified lipoproteins, macrophages transform into lipid–filled foam cells [81].

Endothelial dysfunction also initiates smooth muscle cell (SMC) proliferation in the intima and extracellular matrix remodeling [73, 77-79, 81-84]. Chemotactic and growth factors promote SMC migration and proliferation and result in increased leukocyte recruitment [85-86]. Cytokines and growth factors promote the formation of fibrous cap, composed of SMCs and collagen matrix to encapsulate a lipid core [87].

The lipid core (plaque) is a collection of extracellular lipid pools, inflammatory cells, SMCs, and connective tissue elements [88]. This region, found below the endothelium, contains crystalline cholesterol and cholesterol esters, phospholipids, collagen and cellular debris [85-86, 89-90]. It is rich with thrombogenic factors that can initiate both intrinsic and extrinsic platelet coagulation pathways [91]. Necrotic region can also contain osteocytes, bone cells, which can result in the calcification of atherosclerotic plaque cap.

Deposition of macromolecules, proliferation of SMC and lipid core changes the blood vessel geometry altering the flow conditions and the fluid shear stress experienced by the endothelium. One function of the endothelium is to maintain shear stress in the acceptable physiologic range (10-70 dynes/cm^2) [75, 92]. This is done by constricting or dilating vessel diameter to accommodate short–term shear stress changes [75]. If the change persists, the vessel wall

undergoes permanent positive or negative remodeling. Positive remodeling attempts to reduce the shear stress by increasing blood flow cross–sectional area, while negative remodeling constricts the vessel to increase shear stress [61, 63, 81, 93].

Vulnerable plaque patients are typically asymptomatic and the composition of the plaque plays a role in the vulnerability of the vessel. The weakened state of the vessel in combination of pathologic remodeling and cyclic strain can result in rupture [68]. Risk of rupture assessment can be made using numerical simulation describing vulnerable plaque with detailed material and geometrical description of the pathologic vessel wall composition and flow conditions.

In particular the role of vessel wall components and composition that needs further investigation is the role of calcifications and anisotropy of the vessel wall. Vulnerable plaques are known to contain calcification but their role is still not well understood. Simulations have shown larger calcification to contribute to plaque stability [60, 94-95]. However, other studies have shown correlation between presence of calcification and increased rupture risk. While real vessel tissue is anisotropic material giving it preferred direction of stretch, most of these studies employed isotropic materials [96-97].

Mathematical models have been used over the years by various investigators to determine the risk of rupture, mechanical failure of the coronary artery, due to this disease condition. These studies of vulnerable plaques attempted to identify regions of high stress that may be susceptible to rupture. Rupture is predicted to occur at sites where the stresses are higher than vessel wall material yield strength [98-100].

Vulnerable plaque rupture is a complex problem involving the interaction of pathologic blood flow with vessel wall deformations. Plaque rupture is due to the stresses produced in the vessel wall from the combination of shear and hydrostatic stresses imparted from blood. To generate deformation in the vessel wall, investigators initially used constant and cyclic pressurization [68, 101-102]. These were presided by uncoupled and coupled fluid structure interaction (FSI)

simulations. Coupled FSI simulations relate fluid flow with solid deformation which feedback to influence fluid flow. Current FSI simulations use physiologic boundary conditions including cardiac waveform describing blood flow and pressure, cyclic vessel bending [103].

Blood vessel has multicomponent construction with material property specific to each component. Pathologic vessel conditions result in altered wall composition with weakened vessel wall and the presence of ILT and calcifications. Simulations into evaluate risk of rupture need to consider the contribution of these components. Most of the simulations conducted in 2D geometries contain various layers of the vessel wall and lipid core [55, 113]. Additional material properties can be found from numerical studies performed in 3D geometries describing the vessel components [49, 114, 115].

From these studies, regions of high stress that may be susceptible to plaque rupture, regions of fluctuating wall shear stress and recirculation zones were observed.

Abdominal Aortic Aneurysms. In the abdominal aorta, atherosclerosis is one of the many factors involved in the initiation and development of AAA. Rather than a single cause initiating AAA disease process it results from combination of various factors including atherosclerosis, infections, genetic disposition, smoking, and hemodynamic flow conditions [104-114].

Varying degrees of AAA is present in 9% of humans over the age of 65 [115]. In the developed countries, it is the 10^{th} cause of death of white men over 65 and a burden on the health care system [116-117]. It is the 13^{th} cause of death in the US in which 65% of the patients die of AAA rupture complications [116].

If conditions favorable to the development AAA are present, the disease process results in dilation and permanent remodeling of the abdominal aortic wall. These changes are mainly due to connective tissue degradation of the vessel wall. This destructive remodeling of elastic media results in the depletion of medial smooth muscle cells, destruction of elastin and collagen. The

destruction of these members weakens the elastic property of the vessel wall and may contribute to AAA rupture [118-119].

As stated earlier, atherosclerosis, infections, genetic disposition, smoking, and hemodynamic flow conditions are responsible for the initiation of AAA [104-114]. In addition to those listed above, inflammation and age are known to be involved [109, 114]. Inflammation, one of the factors marking the initiation of AAA disease process, can result from mechanical and biochemical factors. Transmural inflammation leads to destructive remodeling of the elastic media and the depletion of medial smooth muscle cells (SMCs) [120-121]. The development of this disease results in reduced smooth muscle cell density of the abdominal aorta [122]. Age is another factor involved in the initiation of AAA in which age related degradation of elastin and collagen reduces aortic wall tensile strength [123]. Fragmentation of the elastic fibers continues throughout the time of the aneurysm growth until rupture [124-125].

Smooth muscle cells from the media and fibroblasts from adventitia, with inflammatory cells from blood, add to the continued degradation elastin and collagen components of the vessel [118-119, 126]. Degradation of structural media proteins leading to aneurysmal dilation is facilitated by matrix proteases (MMP 2 and MMP 9) [127-129].

Prior to rupture, AAA patients rarely exhibit symptoms. Physicians are alerted to the presence of AAA during diagnosis of high risk patients or in the rare cases when AAA related symptoms are present. Risk factors for the development of AAA were presented earlier. In some cases the presence of AAA may present symptoms of back or abdominal pain as a result of pressure on surrounding tissues.

The anterolateral and posterolateral side are the main locations of AAA susceptible to rupture. Rupture in the anterolateral side, facing away from the spine, is fatal about 97% of the time. Rupture in the posterolateral side, facing the spine, has lower mortality by offering temporary reseal preventing major blood loss due to initial rupture but may soon be followed by larger rupture [130].

Current treatment techniques for AAA are focused in the prevention rupture, the mechanical failure of the abdominal aorta. Treatment for AAA patients may require surgical intervention in form of open surgery or using endovascular techniques. Open surgery in which vascular graft, knitted synthetic textile sealed with collagen or albumin, is placed inside the distended wall, providing structural support, may be preferred for younger patients at low operative risk [131]. Endovascular technique is developed to provide less traumatic alternative open surgery in which vascular graft is placed across the aneurysm using stents to fix it to the normal aortic and iliac walls.

The size of the aneurysm (5.5 cm in men and 5 cm in women) and growth rate greater than 1cm/year are the criterion used to justify surgical intervention. Fitness of the patient to survive surgery is another determinant due to the associated risk of complications that may not be well tolerated by some patients. Physicians place small aneurysm (4.0–5.5 cm) patients on regular scans to see growth rate and size to warrant intervention. However, small diameter aneurysms can and do rupture [132-134]. About 10–24% of the ruptured aneurysms are about 5 cm in maximum diameter [105, 134]. Female patients with smaller aneurysms (<5.5 cm) are at higher risk of rupture than men [135-136].

In the atherosclerotic cardiovascular diseases described above, mechanical failure in the form of vessel wall rupture is the final stage. Vulnerable plaque patients are typically asymptomatic and the composition of the plaque plays a role in the vulnerability of the vessel. Physicians intervene in AAA patients at high risk of rupture based on their aortic vessel diameter.

Vessels at higher risk of rupture may be identified from the numerical simulation results. This may aid physicians in estimating risk and to identify patients that may benefit from intervention. It is able to identify the contribution of the various components of vessel wall and regions of high stress that may rupture. These numerical models need to incorporate patient specific geometries and realistic material properties. The interaction between blood and the vessel wall need to be considered to account for the generated stresses that result from flow and pressure.

Numerical models have been used in the past by various investigators to determine risk of rupture, the mechanical failure, of abdominal aorta. Rupture is occurs at locations of high stress where the stresses exceed the vessel wall material strength [99-100]. Past AAA numerical studies attempted to identify these regions that may be susceptible to rupture based on ideal or patient specific 3D geometries using single material representation of the aortic wall [137-139]. Other studies include the intraluminal thrombus (ILT) as additional component of the aortic wall. Most of these AAA simulations are fluid structure interaction (FSI) studies using physiological waveforms. AAA tissue is anisotropic material that contains calcifications, which are not considered in most numerical studies.

Patient specific geometries of ruptured AAAs were used to identify rupture location from numerical simulation results [140]. Other investigators used numerical simulation coupled with patient specific data to develop rupture potential index (RPI) [99]. The abdominal aorta, similar to other aortic vessels, is constructed from anisotropic multi layered material and in pathologic condition under consideration; ILT and calcifications are additionally present. Ultimately numerical tools are used to determine the stresses present in the vessel wall closely related to blood flow conditions. For this reason various studies have used FSI methodology in their studies. Simulations using coupled or uncoupled solver formulations describing the relation between vessel deformation and the flow conditions have been used in these FSI studies.

II. Research Design and Methods

A. MHV simulations

Flow through mechanical heart valve is complex problem that requires three dimensional considerations for satisfactory description. In these geometries, symmetry plane along the flow axis is present. However two-dimensional description is not sufficient because flow near the hinge region is markedly different from the conditions in the mid plane. Employing the symmetry

plane to consider the problem based on half domain of valve geometry is also not appropriate because turbulence, present in some flow phases, is random phenomenon affected by symmetry boundary conditions [38].

For these reasons, most of the work presented is based on simulations conducted in 3D geometries. Flow through MHV combines characteristics of internal pipe flow with flow around immersed plate conducive for flow separations and generation various vortex structures in the vicinity of the valve. Aortic root and section ventricle wall included in the numerical geometry can be considered pipe wall with leaflet as immersed plates. To reduce the influence of the imposed boundary conditions affecting near valve flow conditions, sufficient entrance and exit lengths (~10 diameters) were provided.

Laminar and turbulent flow assumptions were used to simulate flow through MHVs. Turbulent simulations were conducted using two equation k-ω turbulence model. This model was well suited for intermittent turbulence present at low Re values. Fluid was considered two-phase fluid with fluid carrier phase and dispersed spherical solid particles representing platelets [44]. Blood can exhibit non-Newtonian behavior at low strain rates which was also considered in some of these simulations.

Blood properties at 37°C with a density of ρ = 1.056 g/cm^3 and dynamic viscosity of μ = 0.035 g/cm–s were used. For non-Newtonian studies, the following strain dependent viscosity description in Equation (1) where it can be approximated to have μ = 3.5 cPoise at elevated shear levels (∂U/∂y > 100s-1) was used.

$$\mu = A\left(\frac{\partial U}{\partial y}\right)^{(B-1)} + C$$
$$A = 2.6314\times10^{-2},\ B = 0.47234,\ C = 3.117316\times10^{-3} \tag{1}$$

This is a time dependent problem with inlet velocity corresponding to cardiac waveform. Valve leaflet open and close depending on the pressure gradients at the different phases of the cycle. However for these studies, the deceleration phase to about 300ms from peak systole was considered before the

onset of leaflet motion. At the outlet, downstream of the leaflet, zero gauge pressure boundary condition was used.

Particles, representing platelets, were injected upstream of the leaflet and moved in response to the flow conditions experienced by each individual platelet. To account for the influence of turbulence on particle trajectory, random fluctuations were included computing particle paths [141].

GAMBIT (ANSYS, Inc.) was used for constructing MHV geometry and mesh generation. FIDAP (ANSYS, Inc.), finite element solver, was used in some of the earlier simulations. Fluent (ANSYS, Inc.), finite volume solver was used in the rest of the simulations. The following are equations used to simulate two-phase fluid flow through the MHV geometries. Equations for describing fluid flow, turbulence, two-phase flow, stress and damage accumulation calculations are presented.

Conservation of mass (Continuity)

$$\frac{\partial \rho}{\partial t} + div\, \rho \mathbf{V} = 0 \tag{2}$$

Blood is an incompressible fluid and thus the above general equation is rewritten as the following.

$$div \boldsymbol{V} = 0 \tag{3}$$

Conservation of Momentum (Navier–Stokes equations)

$$\rho \frac{D\mathbf{V}}{Dt} = \rho \mathbf{g} - \nabla p + \frac{\partial}{\partial_j}\left[\mu \left(\frac{\partial v_i}{\partial x_j} + \frac{\partial v_j}{\partial x_i} \right) + \delta_{ij}\, \lambda\, div\, \mathbf{V} \right] + \mathbf{F} \tag{4}$$

Gravity and other body forces were neglected. So the above can be rewritten in the following form.

$$\rho \frac{D\mathbf{V}}{Dt} = -\nabla p + \nabla \mu \left(\nabla \mathbf{V} \right) = -\nabla p + \nabla \tau'_{ij}, \quad \text{where } \tau'_{ij} = \left(\frac{\partial v_i}{\partial x_j} + \frac{\partial v_j}{\partial x_i} \right)$$
$$\rho = \text{density}, \mathbf{V} = \text{velocity vector}, \mu = \text{viscosity},$$
$$p = \text{pressure}, \tau' = \text{stress tensor}, v = \text{velocity} \tag{5}$$

Reynolds average formulation. The presence of turbulence accounted for using Reynolds average formulation of N-S equations. Vector and scalar

quantities in these equations and were decomposed into mean and fluctuating terms, as shown in Equation (6).

$$u_i = \overline{u}_i + u_i' \tag{6}$$

The Reynolds average formulation results in generating additional terms in the momentum equations. After inclusion of turbulence, turbulent stresses terms are present in the momentum equations.

$$\rho \frac{D\mathbf{V}}{Dt} = -\nabla p + \nabla \tau_{ij}, \quad \text{where } \tau_{ij} = \underbrace{\left(\frac{\partial v_i}{\partial x_j} + \frac{\partial v_j}{\partial x_i} \right)}_{\text{Laminar}} + \underbrace{\rho \overline{u_i' u_j'}}_{\text{Turbulent}} \tag{7}$$

The presence of the turbulent stress terms in Navier–Stokes equations results in closure problem, more unknowns than the available number of equations. There are various techniques to tackle this closure problem from zero equation turbulent models to LES [142-143]. In these studies two-equation Wilcox k–ω turbulent model Equation (8) is used for its ability to handle intermittent turbulent flows present in MHV flows [144]. The two additional equations presented below in Equations (9) and (10) are for turbulent kinetic energy, *k*, and the specific dissipation rate, *ω*, Boussinesq hypothesis Equation (14) [142-143].

Wilcox k–ω turbulent model

$$\rho \overline{u_i' u_j'} = \mu_t \left(\frac{\partial v_i}{\partial x_j} + \frac{\partial v_j}{\partial x_i} \right) + \frac{2}{3} \left(\rho k + \mu_t \frac{\partial u_k}{\partial x_k} \right) \delta_{ij}, \text{ where } \mu_t = \alpha^* \frac{\rho k}{\omega} \tag{8}$$

$$\frac{\partial}{\partial t}(\rho k) + \frac{\partial}{\partial x_i}(\rho k u_i) = \frac{\partial}{\partial x_i} \left(\Gamma_k \rho \frac{\partial k}{\partial x_j} \right) + G_k - Y_k + S_k \tag{9}$$

$$\frac{\partial}{\partial t}(\rho \omega) + \frac{\partial}{\partial x_i}(\rho \omega u_i) = \frac{\partial}{\partial x_i} \left(\Gamma_\omega \rho \frac{\partial k}{\partial x_j} \right) + G_\omega - Y_\omega + S_\omega \tag{10}$$

Two–phase fluid flow. The following formulation in Equation (11) describes platelet motion and the interaction between fluid and solid phases. It was assumed that platelets are spherical particles with diameter of 6μm.

$$\frac{du_p}{dt} = F_D \left(u - u_p \right) + \frac{g_x \left(\rho_p - \rho \right)}{\rho_p} + F_x, \text{ momentum for particles} \tag{11}$$

$$\text{where: } F_D = \frac{18\mu}{\rho_p d_p^2}\frac{C_D \,\mathrm{Re}}{24} \text{ and } \mathrm{Re} = \frac{\rho d_p \left|u_p - u\right|}{\mu} \tag{12}$$

Stress calculation. For specific particle paths, values of viscosity, turbulent viscosity, turbulent kinetic energy and components of mean velocity gradient were extracted from the flow results. These values were used to calculate the stress tensor with the corresponding exposure time to obtain the amount of stress accumulation along a particular path line. Components of the stress tensor were condensed into a scalar stress value based on the formulation presented below [34]. Stress accumulation was calculated for selected particle paths from the values the mean flow and turbulent stresses. For the turbulent stresses, Boussinesq approximation, described in Equation (14) was used.

$$\tau_{ij} = \underbrace{\left(\frac{\partial v_i}{\partial x_j} + \frac{\partial v_j}{\partial x_i}\right)}_{\text{Laminar}} + \underbrace{\rho\overline{u_i' u_j'}}_{\text{Turbulent}} \tag{13}$$

$$\tau_{ij} = \underbrace{\left(\frac{\partial v_i}{\partial x_j} + \frac{\partial v_j}{\partial x_i}\right)}_{\text{Laminar}} - \frac{2}{3}\rho k \delta_{ij} - \mu_t\left(\frac{\partial v_i}{\partial x_j} + \frac{\partial v_j}{\partial x_i}\right) \tag{14}$$

$$\sigma = \frac{1}{\sqrt{3}}\sqrt{\tau_{11}^2 + \tau_{22}^2 + \tau_{33}^2 - \tau_{11}\tau_{22} - \tau_{11}\tau_{33} - \tau_{22}\tau_{33} + \left(\tau_{12}^2 + \tau_{23}^2 + \tau_{13}^2\right)} \tag{15}$$

Linear product of stress and exposure time in the form outlined in Equation (16) was used in some of the studies.

$$\sum_{i=t_0}^{t_{\max}} \sigma_i \times \Delta t \tag{16}$$

In addition to the above stress accumulation formulation used until section A.4. Formulation which includes the stress rate was used for analyzing results in section A.5.

$$SA = \sigma \times t_{exp} = \int_{t_0}^{t_{exp}} \sigma(t)dt + \int_{t_0}^{t_{exp}} t\,\dot{\sigma}(t)dt \approx \sum_{i=1}^{N} \sigma_i \times \Delta t + \sum_{i=1}^{N} t_i \times \left|\sigma_i - \sigma_{i-1}\right| \tag{17}$$

Boundary conditions. Physiological cardiac velocity waveform was applied at the inlet. The simulation was conducted for the deceleration phase of the cardiac cycle until 300ms from peak systole [29]. No–slip boundary condition was

imposed at all solid boundaries which includes the vessel walls and the leaflet surfaces. At the outlet, zero gauge pressure was imposed.

Stress accumulation distribution (Bulk measure of stress accumulation). Stress accumulation for each platelet calculated using Equations (16) or (17). The final stress accumulation value of each platelet was used to construct the stress accumulation distribution specific to a valve geometry. Differences in stress accumulation distribution were used to compare different valve geometries.

Damage accumulation. The relation between stress, exposure time, and platelet damage can be described in a damage rate equation. In this formulation, the damage has values between 0 and 1 [145].

$$\dot{D}(t) = \left(\frac{\sigma(t)}{\sigma_0} \right)^r \frac{1}{\left[1 - D(t) \right]^k} \tag{18}$$

$$D(t) = D(t_0) + \int_{t_0}^{t} \left(\frac{\sigma(t)}{\sigma_0} \right)^r \frac{dt}{\left[1 - D(t) \right]^k} \tag{19}$$

The above transcendental equation requires prior knowledge of the stress and damage accumulation behavior to determine the relation between stress and platelet damage. The stress values are obtained from numerical simulation and vary in time and location for each individual platelet.

Model constants, *k* and *r*, were adjusted to give desired behavior of damage rate equation that will produce appropriate damage accumulation behavior. Platelet damage accumulation model needs to capture platelet damage behavior observed in experiment, which is comprised of initial lag, constant accumulation, and refractory phases of tapering off approaching full activation. For this behavior *k* needs have negative value while there is less restriction imposed on the model constant *r* [44]. The discretized form of the damage accumulation model used in this work is presented below.

$$D(t) = D(t_{i-1}) + \left(\frac{\sigma(t_i)}{\sigma_0} \right)^r \frac{\Delta t}{\left[1 - D(t_{i-1}) \right]^k}, \quad i = 1, 2, ..., \max \tag{20}$$

Damage accumulation behavior for ideal cases where the stress is monotonously increasing, decreasing or is kept constant is given in Figure 1. These plots show platelets with initial damage (D_0) of 0 and 0.5. In these plots the *k* and *r* values of the damage accumulation function were fixed at -1 and 5 respectively. In this methodology it was assumed platelets to have “perfect memory”, meaning that damage is additive and there is no recovery process.

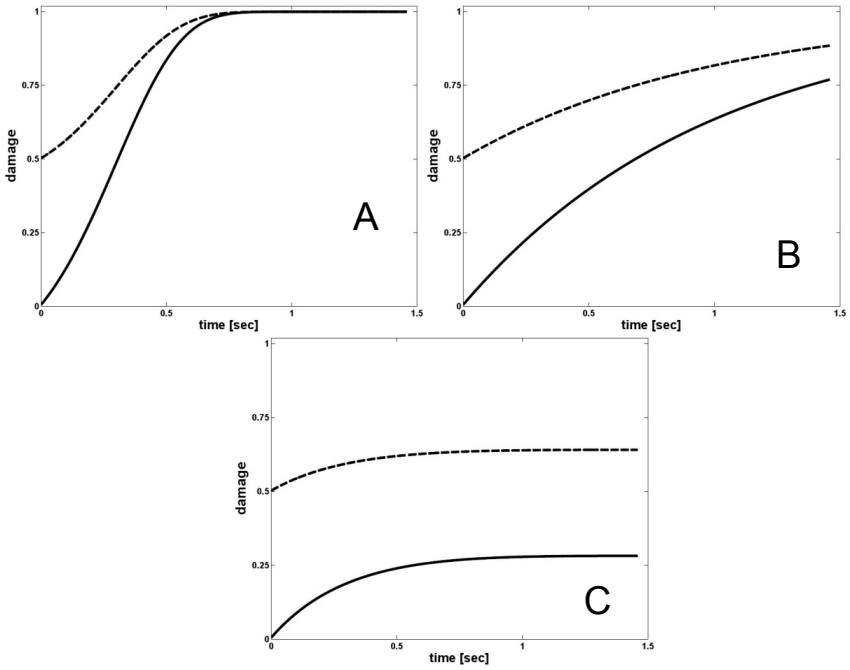

Figure 1 Damage accumulation from stress that is monotonously increasing (A), decreasing (B) and constant (C) [44]

Damage model described in Equation (20) was designed to quantify platelet damage due to mechanical stresses generated by fluid flow. As mentioned in the background, platelet activation can be initiated through biochemical or mechanical stimuli. The focus of this work is platelet activation due to flow stresses. Figure 2 shows platelet activation resulting in shape change due to flow stresses [146]. This releases various factors from the platelet that convert prothrombin into thrombin [147]. Thrombin in turn converts soluble fibrignen into fibrin, clot material [148]. It also feeds back to activate additional platelet [148]. The platelet coagulation cascade, describing these steps of activation and aggregation is outlined in Figure 2.

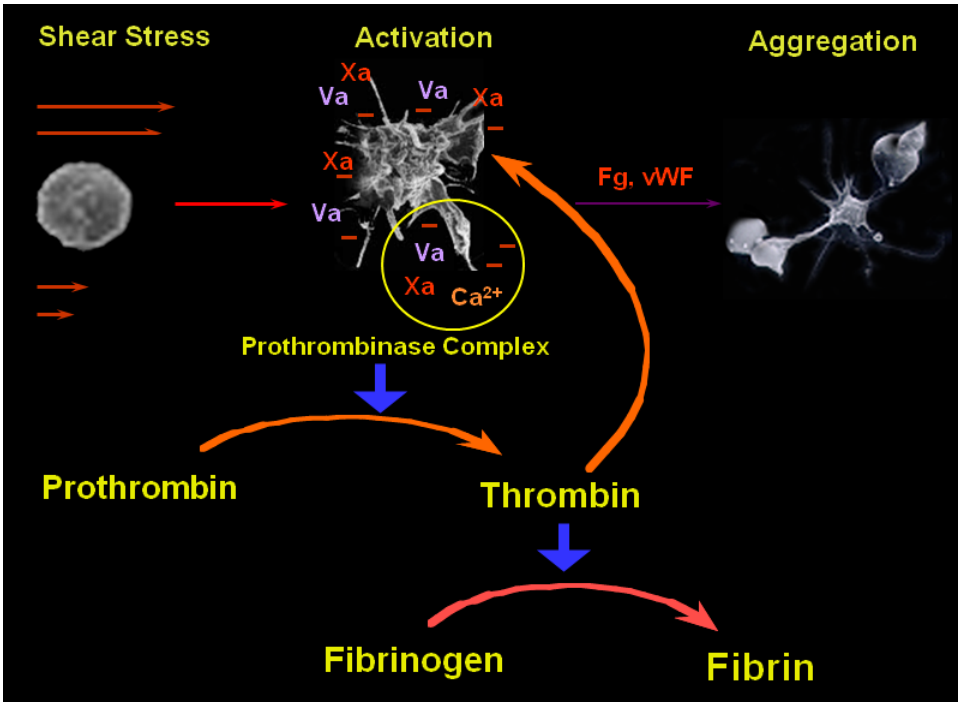

Figure 2 part of the platelet coagulation cascade

Damage model described in this section, does not include mechanism to account for change platelet morphology that occurs during activation. It also lacks mechanism to account for platelet aggregation that follows activation. Future improvements to the damage model will incorporate these features.

Incorporating these steps of the coagulation cascade into the damage model requires user defined subroutines for computing damage accumulation for each platelet at each time point of the simulation. Additional user defined subroutines can account for platelet activation which results in shape change thus changing particle drag coefficient and diameter in Equation (12) ultimately leading to aggregation, by writing subroutine to describe particle-particle interaction.

This damage model predicts platelet specific damage based on the conditions along each particle trajectory. The number of particles simulating platelets was at much lower concentration than physiologic concentration. In whole blood platelet concentration is 2×10^5 platelets/μL [149], which would mean about 1.6×10^{10} platelets in the numerical geometries. The numerical solver allows up to 12% of the volume (about 5×10^{11} particles) to be taken up by

discrete particles, which is more than required to represent physiologic platelet concentration. However due to our limited computational resources, maximum number of particles seeded in the simulations could not exceed 4×10^5.

To overcome this limitation, bootstrapping approach was used to increase platelet population during post processing. This is data resampling scheme used to test the predictions based on small seeded particle population can extrapolated to conditions present in physiologic concentration. Both open source software package ("R" package http://www.r-project.org/) from Bell Laboratories and Matlab (The MathWorks, Inc.) were used for this scheme. The results indicate population above 2×10^3 was sufficient to represent conditions in physiologic MHV flows [150]. As mentioned earlier 4×10^5 particles were seeded for these simulations.

This damage model includes the term (D_0) to account for past platelet damage. This term lumps damage due to platelet age and stresses experienced in the past. Platelets stay about a week in normal circulation and new are produced from progenitor megakaryocyte cells to replace old platelet [149]. With age platelets lose their hemostatic effectiveness [151].

For this study, we assume platelet age in circulation to have normal distribution, with few young and few old platelets. The model assumes older platelet can be damaged to reach full activation, quicker than younger platelet for same stress exposure, in line with experimental observation [152].

Information regarding platelet age can be incorporated into the current damage model by assigning random values (between 0 and 1) for (D_0). In section A.2, value of 0 and 0.5 was assigned for particle trajectory that takes platelet through same path during repeated passes. In addition to changing value of (D_0), random particle trajectory can be assigned during each repeated passes for closer approximation of realistic particle pass over many cycles.

B. VP and AAA simulations

Risk of rupture analysis in vulnerable plaque and AAA requires consideration of the conditions in the solid and fluid domains. This requires

geometrical descriptions and the interaction between these domains. The geometries can be either idealized, as in some of the VP and AAA studies that will be presented, or constructed from patient specific medical images.

For patient specific geometries, lines delineating the various vessel components identified from the medical images with consult and guidance of physicians. These patient specific geometries were obtained with an approved protocol of the Stony Brook University Institutional Review Boards (IRB) Committees on Research Involving Human Subjects. Informed consent was obtained retrospectively.

Spatial coordinates from these images were used to construct the simulation geometries. Image reconstruction of patient specific AAA geometry is described in the following section.

AAA image reconstruction. There are two routes taken to convert patient specific CT scans to numerical geometries. The medical images were obtained either as raw CT data or composed into 3D images (MMS Inc, NH, USA) which are used by physicians to view the AAA, composition and measure dimensions of the aneurysm.

For the raw CT images, Mimics (Materialise, Leuven, Belgium) was used in image reconstruction tool were used and for the MMS composed images, in house code used to convert to acceptable format. The MMS format contains surface coordinate of the ILT, calcifications and blood flow domains in finite element format.

Surface coordinates of the various components of AAA in these composite images are in finite element mesh format. These coordinates were converted into discretized geometry (GAMBIT and ADINA) using in–house C and Matlab codes [153]. The AAA patient geometries created contain fluid and solid domains consisting of healthy vessel tissue, ILT and calcification, part of the solid domain. The AAA vessel wall was assigned a uniform 2mm thickness. In Figure 3 the image reconstruction approach is presented.

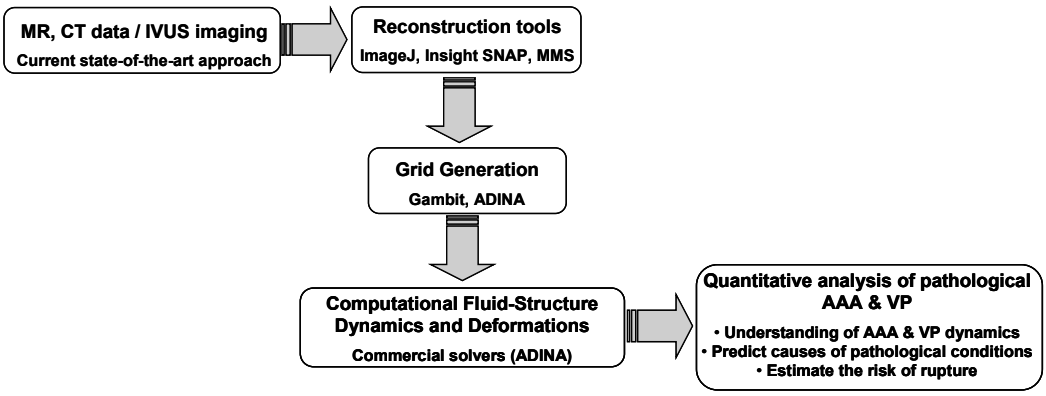

Figure 3 Image reconstruction flowchart

The vessel wall constituents considered in these studies include, the healthy vessel tissue, intraluminal thrombus (ILT), calcification and lumen. Constructing geometries containing every anatomical detail of these geometries is challenging. For this reason, simplifications were made regarding the number of calcifications, size and locations of ILT and small vessel branching from the main geometry of interest. The focus of these simulations is evaluating the risk of rupture and for this purpose the simulation is restricted regions in the vicinity of the aneurysmal dilation.

Identical finite element formulation was used for solving coupled fluid flow and solid deformations in VP and AAA. For the fluid domain, Newtonian fluid properties were used to describe blood at 37°C with a density of $\rho = 1.056$ g/cm^3 and dynamic viscosity of $\mu = 0.035$ g/cm–s. The strain energy density function used to describe the hyperelastic vessel wall material is presented in Equations (24) - (26). Material property constants are presented in Table 1.

A commercial finite-element based software ADINA (ADINA R&D Inc., MA) was used for performing the FSI analysis. This tool strongly couples solid deformations result from fluid stresses transmitted through the fluid–structure interface. Due to this solid–fluid coupling, solid wall deformation in turn changes the flow domain resulting in changing conditions in the flow field.

$$M\ddot{\mathbf{U}} + C\dot{\mathbf{U}} + K\mathbf{U} = \mathbf{R} \tag{21}$$

M, C and K, represent mass, damping and stiffness matrices. $\mathbf{R}$ is the vector for externally applied loads. $\ddot{\mathbf{U}}$, $\dot{\mathbf{U}}$ and $\mathbf{U}$ are the vectors of acceleration,

velocity and displacement vectors of the structural domain. For the fluid domain, the momentum and continuity equations are presented below.

$$\nabla \cdot \mathbf{V} = 0 \tag{22}$$

$$\rho\left(\frac{\partial \mathbf{V}}{\partial t} + \left(\mathbf{V} - \mathbf{V_g}\right)\cdot \nabla \mathbf{V}\right) + \nabla p = \mu \nabla^2 \mathbf{V} \tag{23}$$

$\mathbf{V}$ and $\mathbf{V_g}$ represent the fluid velocity and local grid velocity vectors used for the Arbitrary Lagrangian Eulerian (ALE) moving mesh approach. Static pressure p, time t, density ρ and viscosity μ are the other terms in the momentum equation.

The strain energy density functions describing the anisotropic material behavior of the vessel are shown below in Equations (24) - (26).

$$W = W_{\text{isotropic}} + W_{\text{anisotropic}} \tag{24}$$

$$W_{\text{isotropic}} = C_1\left(I_1 - 3\right) + C_2\left(I_2 - 3\right) + D_1 e^{(I_1 - 3)} - 1 \tag{25}$$

I_1 and I_2 are the first and second invariants of the Cauchy–Green deformation tensor ($C_{ij} = 2\varepsilon_{ij} + \delta_{ij}$, where ε_{ij} and δ_{ij} =Kronecker delta). C_1, C_2, D_1 and C_2 are material constants.

$$W_{\text{anisotropic}} = \frac{k_1}{2k_2}\left\{\exp\left[k_2\left(J_4 - 1\right)^2\right] + \exp\left[k_2\left(J_6 - 1\right)^2\right] - 2\right\} \tag{26}$$

J_4 and J_6 are the forth and sixths invariants of the Cauchy–Green deformation tensor. k_1 and k_2 are material constants. Anisotropic property arises due to fiber orientation information contained within J_4 and J_6 invariants.

Orthotropic material was used to represent the vessel wall. This model describes fiber-reinforced hyperelastic material to represent vessel wall and its collagen component. Real vessel tissue has preferential stretch direction which was approximated using the orthotropic material model. Formulation and model constants for orthotropic vessel wall description are presented below.

Material	C_1 [Pa]	C_3 [Pa]	D_1 [Pa]	D_2	k_1 [Pa]	k_2	a_a^o	a_b^o
Anisotropic Wall	8,888	164,900	48.7	53.46	1,886	94.75	5^0	265^0

Table 1 Material properties for the fibrous wall used in the FSI simulations

Boundary and initial conditions. For these FSI simulations, appropriate boundary condition is needed for both the solid and fluid domains. For the solid domain, inlet and outlets are set to remain static for the case of AAA while the outlet may have some restrictions for the case of VP. For the fluid domain, inlet velocity and outlet pressure is applied. The geometry is pressurized to physiological pressure. For some of the VP simulations, initial pre stretching is performed. The interaction between the fluid and solid domains is through the stresses and displacements at the common fluid-solid surfaces.

Wall strength and Rupture Potential Index. Clinical and geometric rapture predictors were lamped to calculate local vessel wall strength.

$$Strength = 71.9 - 37.9\left(ILT^{1/2} - 0.81\right) - 15.6\left(NORD - 2.46\right) - 21.3\,HIST + 19.3\,SEX. \quad (27)$$

Where *ILT* is local ILT thickness in cm, *NORD* local diameter normalized to the non-aneurysmal aortic diameter, estimated from the patient's age and sex [154], *HIST* is family history (½ with history, -½ without history) and *SEX* is patient's gender (½ male, - ½ female). Some of these parameters (family history, gender, AAA size) were from patient specific medical data while others were measured from the medical images.

Based on local stress values, rupture potential index (RPI) was calculated as the ratio of local stress and local wall strength.

$$RPI = \frac{Local\ wall\ Stress\ obtained\ \ from\ FSI\ [N/cm^2]}{Local\ wall\ Strength[N/cm^2]} \quad (28)$$

III. Numerical studies of blood flow in cardiovascular pathologies

Validation study of the numerical methodology – a case study of platelet activation in stenotic coronary arteries

Numerical simulation techniques can be used to investigate pathological flow problems that underlie cardiovascular diseases. These predictions from numerical simulations need to be validated through flow visualization techniques.

The aim of this validation study was to determine flow conditions in idealized geometry of stenotic coronary artery and quantify the stresses platelet experience in this geometry from simulation and visualization results. This was performed by comparing the stress along similar particle trajectories extracted from the simulation and visualization studies. Validation of the stress accumulation and the corresponding platelet activation was done by comparing against *in-vitro* platelet activation measurements.

Numerical simulation of flow through ideal eccentric stenosis 3D geometry with 84% constriction was conducted [155]. Flow equations can accommodate the presence of intermittent turbulence and spherical particles used to represent platelets. The flow results were used to study platelet stress accumulation that results from the presence of stenosis.

Results of computational fluid dynamics (CFD) simulations were compared against Digital Particle Image Velocimetry (DPIV) and against Platelet Activation State (PAS) measurements performed by others in our group. DPIV and PAS studies were used to validate the capability of numerical simulation of flow induced platelet stress accumulation.

Result Various cross sections showing the axial velocity vectors obtained from the numerical simulations are presented in Figure 4. From these figures parabolic profile upstream of the stenosis becoming fully developed turbulent jet at the apex of the stenosis can be seen to relaminarize downstream of the stenosis. Complex 3D trajectories presented in Figure 4 show the affect of turbulence on platelet paths by stochastic particle tracking model representing turbulent platelet trajectory. Platelets experience the highest stresses are at location of maximum constriction and for short duration.

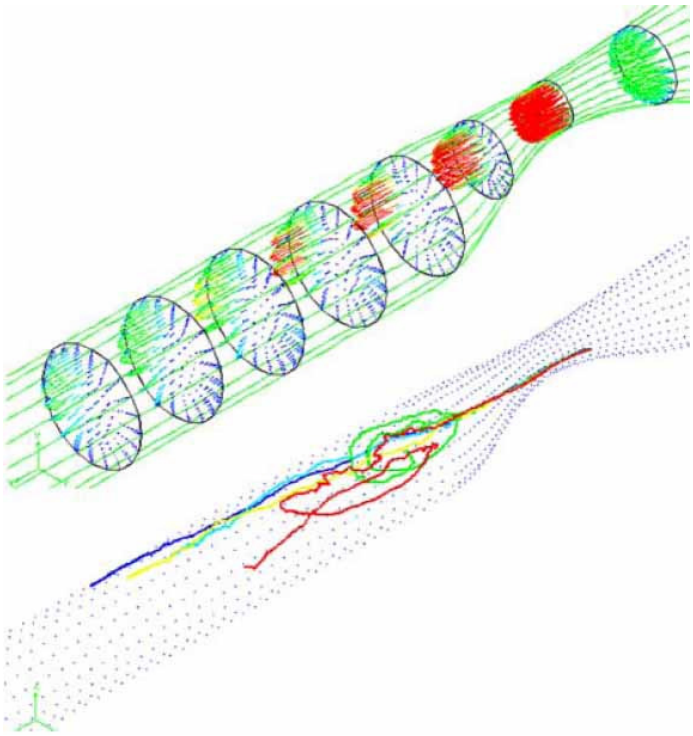

Figure 4 Axial velocity vectors and trajectories for flow through stenosis [155]

Platelets trapped in recirculation zones experience longer durations of low shear stress. Mid plane velocity vectors and shear rate contour maps are presented in Figure 5 showing in blue the recirculation zone and in red accelerated jet flow and regions of elevated stresses. Values of velocity range between -0.20 to 2.00 m/s and shear rate values are between 0–7500 s^{-1}. High shear stress regions are near the wall and at the interface between recirculation zone and the jet.

The difference in magnitude of the CFD and DPIV results is due to the dimensional differences between the two. Keeping dynamic similarity enabled the comparison of simulation results and experimental measurements. The DPIV model was 5 times larger, resulting with velocity and shear rate values 5 and 25 times smaller.

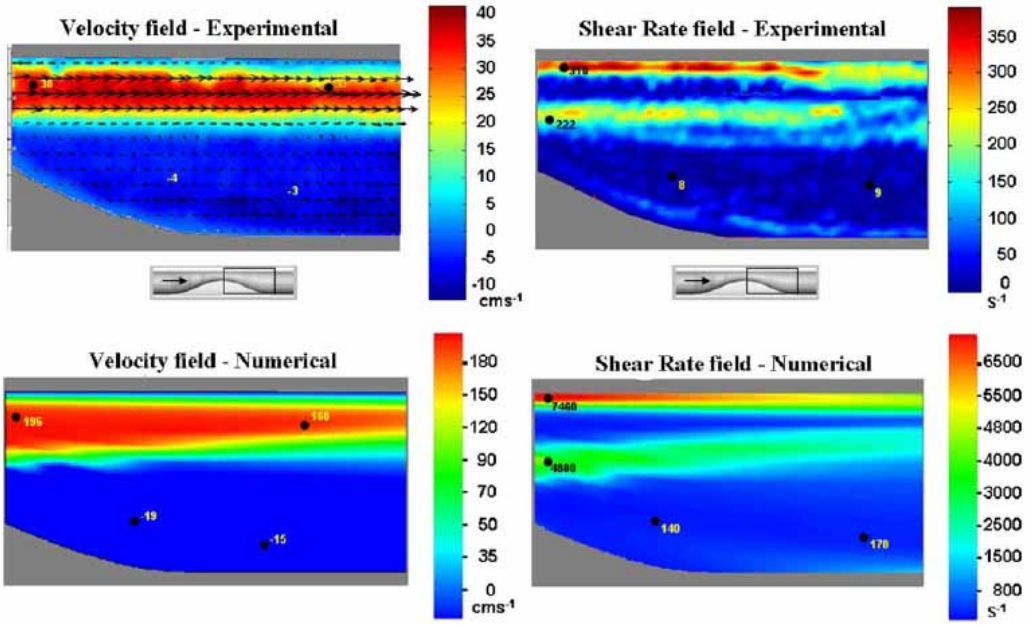

Figure 5 Velocity magnitude and shear rate contour maps comparing the CFD and DPIV results [155]

Discussion This study shows the contribution of mechanical factors of flow dynamics involved in platelet activation. Results of stress accumulation along pertinent trajectories from numerical simulation were compared against flow visualization and using PAS assay measurements in recirculation flow loop. In this study, shed vortices and flow reattachment were observed in regions similar to past numerical and experimental observations [156].

Both the CFD and DPIV measurements used similar trajectories to calculate platelet activation level. This study demonstrates the viability of CFD to use flow condition information to compute the resulting platelet activation in complex 3D geometries. It also shows the advantages CFD over current capabilities DPIV systems. CFD can provide much higher temporal resolution than DPIV measurements which have resolution limited by the camera frame rate.

Dynamic similarity was maintained between the geometries used in the numerical and experimental studies. Rigidity of the model was one difference between the numerical and experimental geometries. While compliant material was used in the DPIV study, the CFD model was perfectly rigid. This produced

negligible difference in flow conditions. The numerical study used non-Newtonian fluid behaviors while Newtonian fluid was used for the DPIV. Non-Newtonian behavior is known to dominate at low strain rates and is negligible in most flow phases.

These studies are in line with previous studies which show stenosed coronary arteries to cause significant platelet activation, depend on both shear stress and exposure time [18]. While the CFD/DPIV considers single passages through the stenosis geometries, the PAS recirculation results were conducted over 30 min of repeated platelet exposure to the stenosed region. Even though the recirculation results were based on repeated passage, the same trend predicted by the CFD/DPIV was found in–vitro, in which the symmetric activated more than eccentric stenosis geometry.

Numerical simulation of flow through idealized stenosis geometry was used to validate the capability of numerical simulation to generate realistic particle trajectories as seen in the DPIV measurements. Computed stress accumulation values were correlated against PAS platelet studies. These validation studies demonstrate the capability of numerical simulations to identify individual platelet trajectories and compute the stress accumulation, which is shown to correlate with platelet damage.

This platelet activation estimate can be used in the design of various cardiovascular prosthetic devices, and/or studying pathological flow conditions involving disturbed flows. Several approaches are available for combining exposure time and shear stress which are used to estimate activation level of formed elements in blood [16]. The development of platelet damage/activation accumulation models which accounts for exposure time and shear stress will be explored in section A.2. In the following section (A.1), stress exposure time and the resulting platelet activation is used to compare two valve geometries.

A. 2–D mono/bileaflet valves, 3–D bileaflet and development of platelet damage model, stress accumulation distribution, valve design optimization

To study the relation between geometry and flow stresses affecting platelets, numerical simulations were conducted in geometries that generate pathologic flow conditions. In these numerical studies, spherical particles were used to represent platelets. Flow results were compared with flow visualization and In–vitro platelet activation measurements.

The studies presented below are: (i) comparison platelet stress accumulation in monoleaflet and bileaflet MHV geometries, (ii) platelet stress accumulation and the development of a platelet damage model for flow through 3D MHV geometry (iii) development of stress accumulation distribution to evaluate valve performance, and (iv) design optimization study based on stress accumulation distribution.

A.1 Comparison of mono and bileaflet mechanical heart valves

Numerical simulations of blood flow through monoleaflet and bileaflet MHVs were conducted to study the resulting flow induced platelet activation by these valve geometries [157]. The valve geometries for the numerical simulations were based on St. Jude bileaflet and monoleaflet valve from Bjork–Shiley. These calculations were conducted in 2D valve geometries with non–Newtonian fluid representing blood experiencing intermittent turbulence. Particles, representing platelets, were seeded upstream of the leaflet in these geometries and relevant values for stress accumulation calculation extracted. The results obtained from the numerical predictions compared to experimental Platelet Activation State (PAS) measurements performed by others for bileaflet and monoleaflet valves [157].

Result Velocity vector field through the bileaflet MHV 198 ms after peak systole (Figure 6) shows flow separation leading to decreased flow area between leaflets resulting in stronger turbulent jets. The maximum velocity for this geometry at this phase was 134 cm/s. At later times (approaching 300ms), the

shed vortices subside because inlet velocity decreases depriving shed vortices of energy.

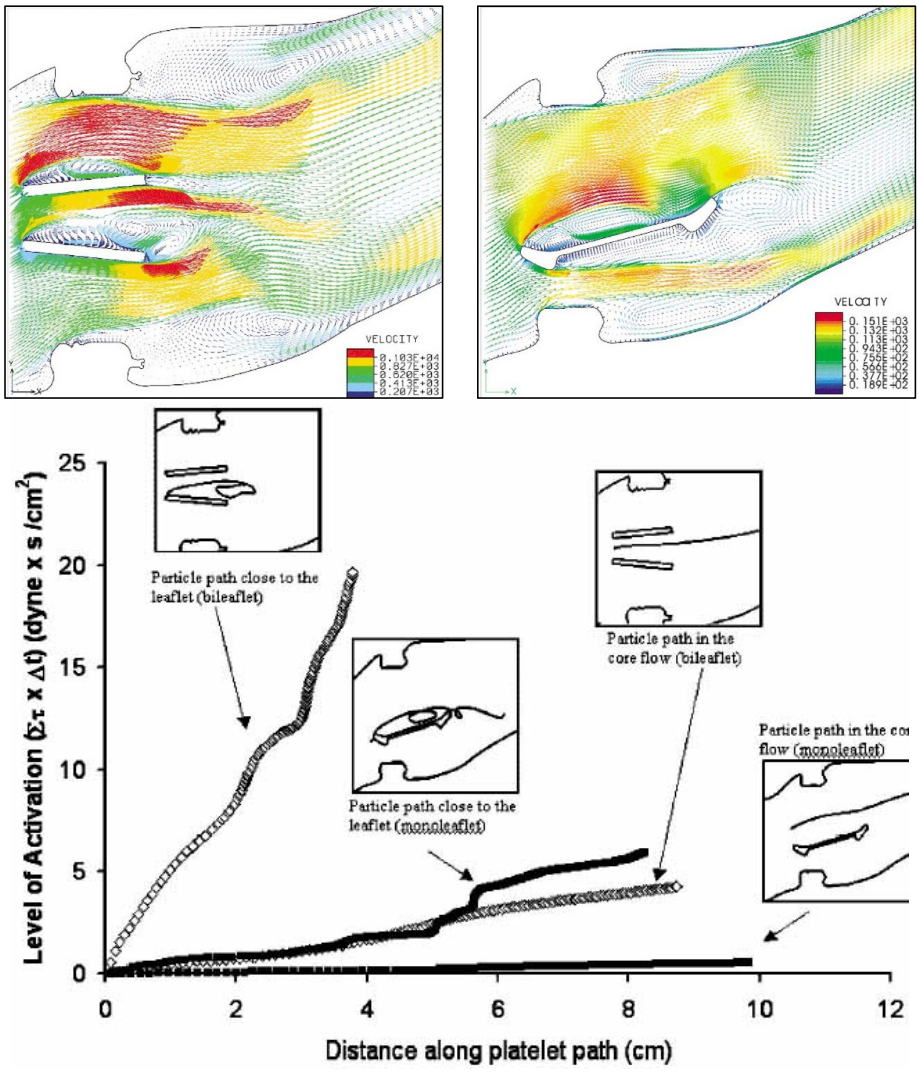

Figure 6 Velocity vectors for bileaflet and monoleaflet MHV and shear stress histories for various paths in the mono and bileaflet valves [157]

The numerical study compared the stress accumulation for flow through bileaflet and monoleaflet MHVs and compare with experimental results. Level of platelet activation observed in the Carbomedics bileaflet and a Bjork–Shiley monoleaflet MHVs is presented in Figure 7. The rates of activation values were 8.11×10^{4} min^{-1} for the bileaflet and 3.14×10^{4} min^{-1} for the monoleaflet valve [157]. The numerical models included misaligned valve implantation with 15° off the major blood flow axis. The experimental study also included misalignment different from one in the numerical study.

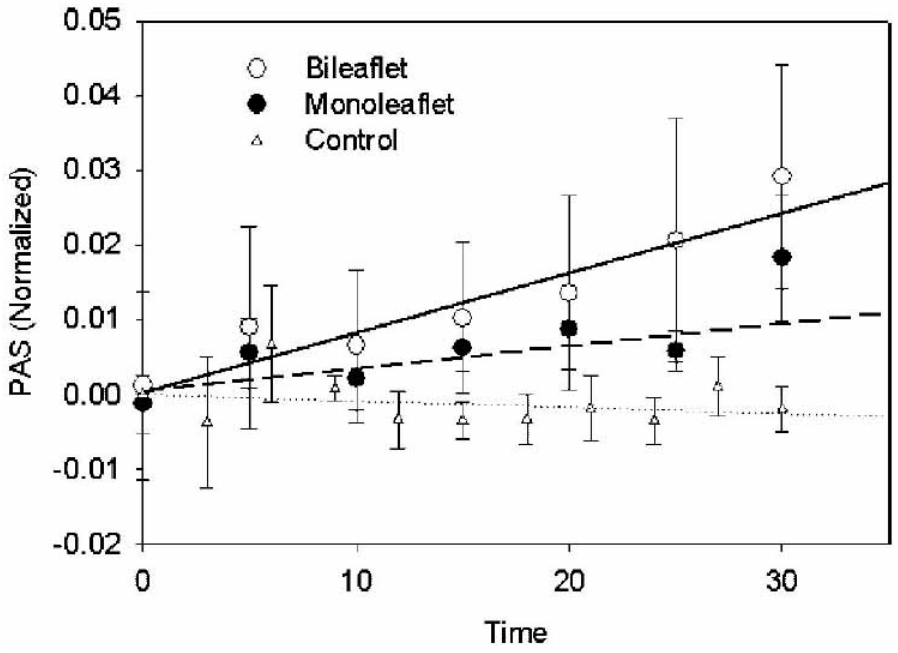

Figure 7 Level of platelet activation observed in the Carbomedics bileaflet and a Bjork–Shiley monoleaflet MHVs [157]

Geometry differences of monoleaflet and bileaflet MHVs generate different flow patterns. In the monoleaflet MHV, rapid deceleration of the blood flow and shed vortices appear at the earlier phase of the flow. Stronger wake of shed vortices persist longer (198ms) in the bileaflet than the monoleaflet. Because the shed vortices appear at different times, same time points cannot be used for comparison. In the monoleaflet geometry the shed vortices appear 20 ms after peak systole. Bjork–Shiley monoleaflet MHV generates vortices around the leaflet due to its geometry with shorter wake form two or three vortices were shed behind the leaflet. In the monoleaflet geometry, the imposed misalignment of the valve housing with respect to the flow axis improves the leaflet alignment with the flow, reducing the valve's effect. Of these two geometries, the monoleaflet results in higher velocity (167 cm/s) than the bileaflet MHV. Unlike the bileaflet MHV, the velocity jets through the monoleaflet decay at faster rate to the bileaflet.

Platelet stress accumulation was calculated on selected trajectories out of the large number of particles seeded upstream of the valve leaflet(s). These selected trajectories of interest include, high stress region near the leaflet(s) and in the low shear region of the core flow. Stress accumulation was calculated for

these selected trajectories. For trajectories close to the leaflet, the maximum values of particle stress accumulation are 20 dyne-s/cm^2 and 5 dyne-s/cm^2 for the bileaflet and monoleaflet MHVs respectively. These values show the stress accumulation to be lower in the monoleaflet as compared to the bileaflet. Similar values of stress accumulation were obtained in core flow region of the bileaflet as in the high stress region of the monoleaflet valve Figure 6.

Discussion This work, in a well-controlled in vitro system, shows platelet activation to be dependent on the valve geometry. The experimental study was able to measure flow induced platelet activation but was not equipped to identify regions of high stress and length of exposure time that led to platelet activation. In the numerical simulation, particle stress accumulation was calculated for flow through valves implanted in physiologic geometries.

The experimental setup does not identify individual platelet trajectories and their specific stress accumulation values.

Unlike the experimental measurement, the numerical simulation can identify specific trajectories of interest for particle stress accumulation calculation at any position in the flow field. In the numerical studies, two valves implanted in physiological geometries that include left ventricle and aorta was used to simulate the in vivo flow patterns after implantation. The numerical results due to valve geometry differences were compared against the experimental measurements.

Good correlation between 2D turbulent simulations and DPIV measurements in a wake of a bileaflet MHV was found in past study [158]. Geometric differences between the monoleaflet and bileaflet MHVs produced shed vortices at different time points after peak systole. Peak activities that occur at different time points where used to compare the two geometries (198 ms for the bileaflet and 20 ms for the monoleaflet MHV). In the bileaflet valve, flow separation followed by a wake of shed vortices decreased the orifice area between the valve leaflets facilitating conditions for stronger turbulent jet flow compared to the monoleaflet valve as shown in Figure 6.

Turbulent energy from the largest eddies cascades to smaller eddies until dissipated by the smallest eddies at the Kolmogorov scale. The smallest eddies dissipate energy to blood formed elements [159]. If the dimensions of the Kolmogorov scales are in the cellular range, turbulent stresses can activate or damage blood cells. Dimensions of the smallest eddy from CFD was $\mu_k \approx \left(V^3/\varepsilon\right)^{1/4} = 4.66\mu m$, which is about the size of platelets (4 μm) leading platelet damage [26] by imparting higher strain energy to platelet membranes making them more susceptible to stress induced activation [159].

Higher shear stresses present in the bileaflet valve are more favorable for platelet activation. The monoleaflet valve provides larger flow area and better alignment of the leaflet with the major flow axis resulting in smaller flow separation above the leaflet. The wake near trailing edge of the monoleaflet was shorter and produced smaller region of high shear stress.

A mild misalignment 15° was included in the numerical geometry to account for the difficulty to place the valve in the optimal alignment during surgery. This produces stronger jet due to the narrower cross–section available for forward flow producing wide wake and shed vortices in bileaflet MHV. Particles that pass near the valve leaflet experience higher stresses and may soon after get trapped within the shed vortices in the valve's wake, Figure 6. These types of paths result in rapid increase in the shear stress value up to 20 dyne-s/cm^2 over a short span during just a single passage (distance along the trajectory of 4 cm). The equivalent trajectory in the monoleaflet MHV results in stress accumulation value of about 5 dyne–s/cm^2 for 8 cm along the trajectory.

Lower shear stress values are found in the core region of the two valves. There is a difference in shear-stress histories of the two geometries with the bileaflet producing five times higher values than the monoleaflet. In addition to elevated shear stresses, the rapid acceleration–deceleration exposes platelets to deformation stresses [13].

The experimental study includes all phase of flow through the valve. However, the numerical study was conducted for fully open position of the valve

with no regurgitant flow, no leaflet closure, and without considering the flow in the hinge regions. Simulation considered the deceleration phase, the first 300ms after systole, when there is no leaflet motion. In this phase, shed vortices are generated resulting in increased platelet aggregation potential, source of thromboemboli. This phase results in rapid stress accumulation due to the combination of stress and longer residence time for particles trapped in the recirculation zones. Shed vortices and elevated stresses present during this phase are hypothesized to be the source of cerebrovascular microemboli associated with MHVs.

This study showed stress accumulation to be a viable tool in assessing the thrombogenicity of MHV design. In the following section, its use in evaluating 3D MHV geometry which includes physiologic near valve regions is presented. The development of platelet damage model which is used to explore the relation between stress and the resulting damage is also detailed.

A.2 A damage accumulation model for platelets

In this numerical simulation study of blood flow through 3D MHV geometry, blood was considered to be two–phase, non–Newtonian fluid experiencing intermittent turbulence [44]. The 3D valve geometry is based on the St. Jude bileaflet design implanted in the aortic position with slight misalignment. Flow results were used in the development of new damage accumulation model, to quantify the damage that results from flow stresses.

The CFD study was done to understand the flow conditions through physiologic MHV geometry and determine stress induced platelet damage. Transient and turbulent flow calculation was conducted for two–phase non–Newtonian fluid with spherical solid particles (6 μm) representing platelets. Particle path calculation considers the influence of intermittent turbulence known to be present during parts of the cardiac cycle.

Turbulent and mean flow stress values were extracted for pertinent particle paths. These values were used to calculate platelet stress accumulation and the resulting damage accumulation. Platelet damage accumulation was

calculated based on a new damage model that accounts past damage history, outlined in Equation (20).

Results *Flow field.* The following cross–sections are chosen to illustrate some important features of the complex time dependent 3D flow field Figure 8. Flow results show the presence of a complex flow field with flow separation, present above both leaflet, can clearly be seen above the lower leaflet. Three strong jets are present above, in between and below the leaflets. The presented cross–sections also show the presence of recirculation zones above and below the leaflet and in the expansion downstream of the valve housing. Blood from the sides of the leaflet gets entrained towards the center in establishing counter rotating spiral vortices. This can be clearly seen from the particle path plot Figure 8.

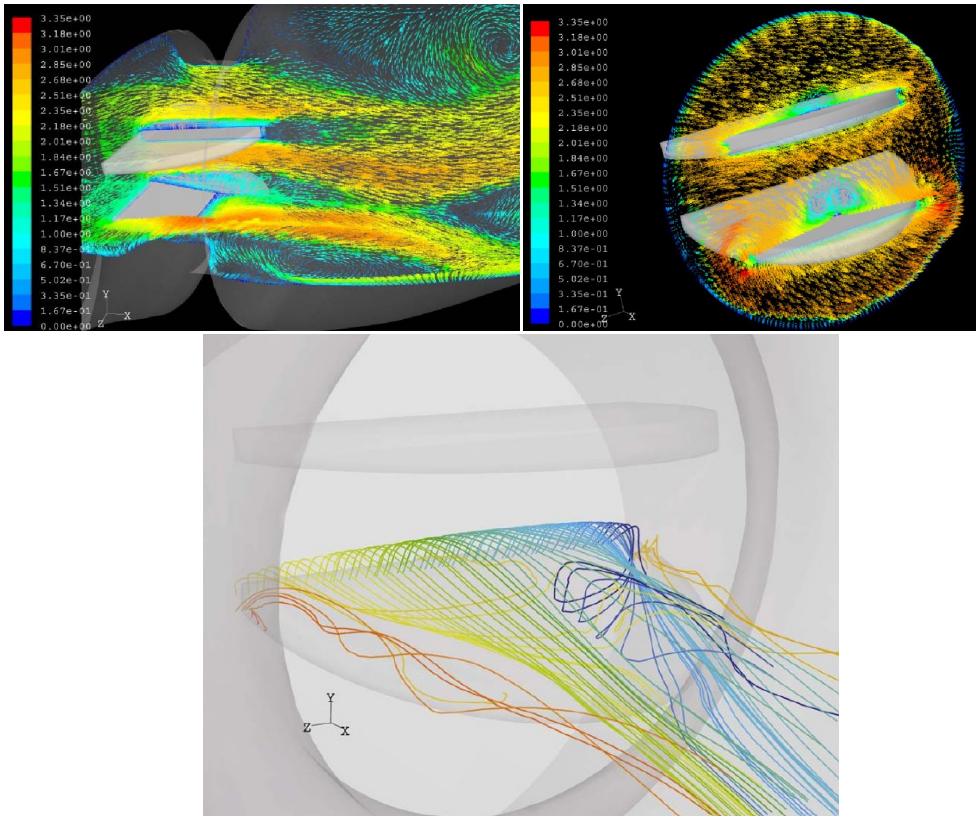

Figure 8 Orthogonal planes along the flow axis and cross sectional cut showing velocity vectors near the leaflet flow field showing spiral-helical flow patterns which can also be seen from pathlines near the lower leaflet [44]

Stress accumulation. As mentioned earlier, this two–phase flow simulation included solid particles to represent platelets. Some pertinent particle paths that go through recirculation zones, in strong jets and spiral vortices were chosen for stress and damage accumulation calculations. Plots of four representative particle paths and their corresponding stress accumulations are presented in Figure 9. The highest values stress accumulation was obtained for particle paths in the recirculation zones or in the spiral vortices.

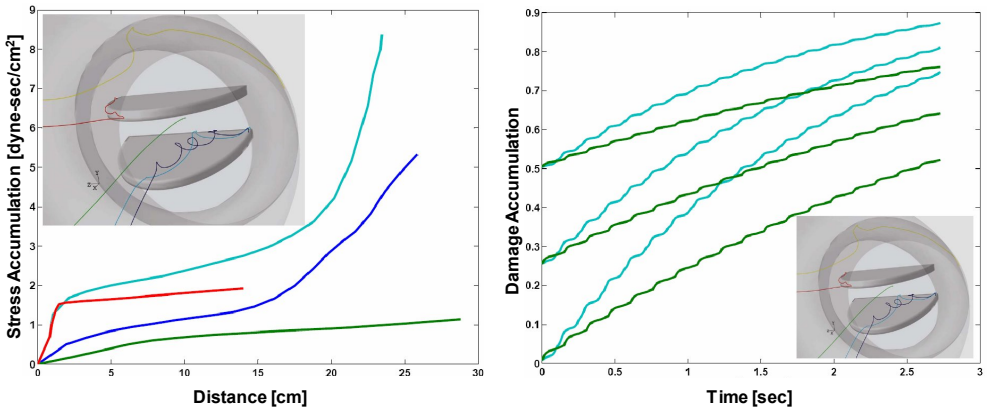

Figure 9 Stress accumulation (left) and damage accumulation for selected platelet paths in high and low stress flow regions near the valve leaflet [44]

Damage accumulation. From the particle paths used in stress accumulation calculation two were selected to be used to determine the resulting damage accumulation. The selected paths are in the recirculation zone and in the region between the valves with the highest and lowest stress accumulation values respectively. To assess the damage model behavior, three cases of initial damage value ($D(t_0)$ = 0, 0.25, 0.5) were imposed on these particle paths. The damage accumulation plot shows platelets that complete 18 repeated passes through the valve region Figure 9. For this case of repeated passes, the final damage value calculated during one pass is used as the initial damage value of the subsequent pass. The plot show paths with high stress accumulation also have high damage accumulation.

Discussion *Flow field.* The model used in this study incorporates slight misalignment of the implanted valve geometry. This misalignment establishes a

low pressure region above the leaflet that result in flow separation and counter rotating spiral vortices. Counter rotating spiral vortices generated between the MHV leaflets entrain fluid towards the center [30]. These flow structures result in decreased flow area resulting in strong jets, high velocity gradient and high shear stresses which contribute to platelet stress damage. As mentioned earlier the particles were initially placed upstream of the valve leaflet. Most of them are ejected away from the high stress regions. However, some have much longer residence time, being trapped in recirculation zones or spiral vortices.

Stress accumulation. The presence of various recirculation zones increases the chance of being trapped in regions with long residence times and result in higher stress accumulation values. This is evident from the particle paths that result in the highest and lowest stress accumulation values which are in the spiral vortices and core flow regions respectively. From the stress accumulation plots the two paths that have the highest and lowest values of stress accumulation were selected for damage accumulation calculation.

Damage accumulation. The path in the low stress region which has low stress accumulation also has slower damage accumulation rate. Stress is time dependent and along the particle path can hold different values. The small “wiggles” of the damage accumulation curve are manifestation of stress value fluctuations along particular path line. Similar behavior was observed by others in which the hemolysis accumulation curve has the imprint of the imposed sinusoidal stress [51].

This and the preceding section used information extracted from individual platelet trajectories to calculate stress and damage accumulation specific to individual paths. These showed the relation between flow stresses and the resulting stress and damage accumulation specific to individual platelet trajectories.

In the following sections, stress accumulation methodology was expanded to bulk stress accumulation distribution of population of platelets. This may identify the overall valve performance due to design specific geometrical features based on stress accumulation distribution. It also can be used in design

optimization of MHV geometries and in the evaluation of other blood recirculating devices.

In the following section, platelet stress accumulation distribution is used to study the influence of valve geometry to dictate flow induced stresses in idealized 2D mechanical heart valves (MHV). The capability of stress accumulation distribution to identify design differences was demonstrated for simulations conducted in realistic 3D valve geometries.

A.3 Stress accumulation distribution for whole valve evaluation – 2D validation studies

Idealized, 2D mechanical heart valve geometries based on ball and cage, monoleaflet and bileaflet valves were used to investigate the capabilities of the stress accumulation distribution to identify design differences. Statistical distribution of flow induced stress accumulation for population of platelet trajectories is defined as the stress accumulation distribution. Stress accumulation distribution from these valves was compared against control, flow through straight tube. Except near the vicinity of the valve mechanisms, these geometries have identical mesh upstream and downstream of the valves. Identical boundary conditions were imposed and identical number of particles, simulating platelets, were seeded upstream of the valves. Time dependent simulation with constant inlet velocity was conducted for two-phase fluid representing blood [44, 155, 157].

Flow stresses and trajectories for each particle were extracted from the simulation. Stress accumulation for each particle is calculated using Equation (16). Statistical stress accumulation distributions plots were used to evaluate performance of the different valve geometries. This may be used to identify differences in the valve geometries from stress accumulation distribution.

Results The ball and cage design was observed to have the highest velocities of the three valve designs followed by the bileaflet and then monoleaflet valves. Maximum velocity values were 2.5m/s for ball and cage, 1.8m/s for bileaflet and 1.6m/s for monoleaflet. All these were higher than what was observed in the control geometry. In addition to producing the highest

velocities, the ball and cage design also has the largest flow separation region followed by the bileaflet geometry. The monoleaflet valve produced the smallest flow separation, Figure 10.

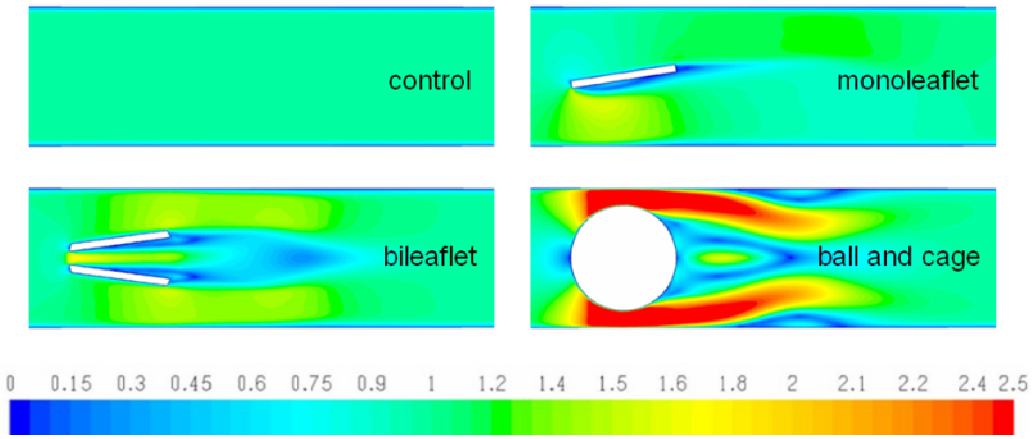

Figure 10 Velocity contour plots in various simplified 2D MHV geometries

The ball and cage valve geometry had the highest velocities and also produced the highest mean value of platelet stress accumulation. Similarly, the bileaflet has higher stress accumulation values than the monoleaflet geometry. These values were higher than the stress accumulation produced by the control geometry. Graphical representation of the stress accumulation distributions are presented in Figure 11.

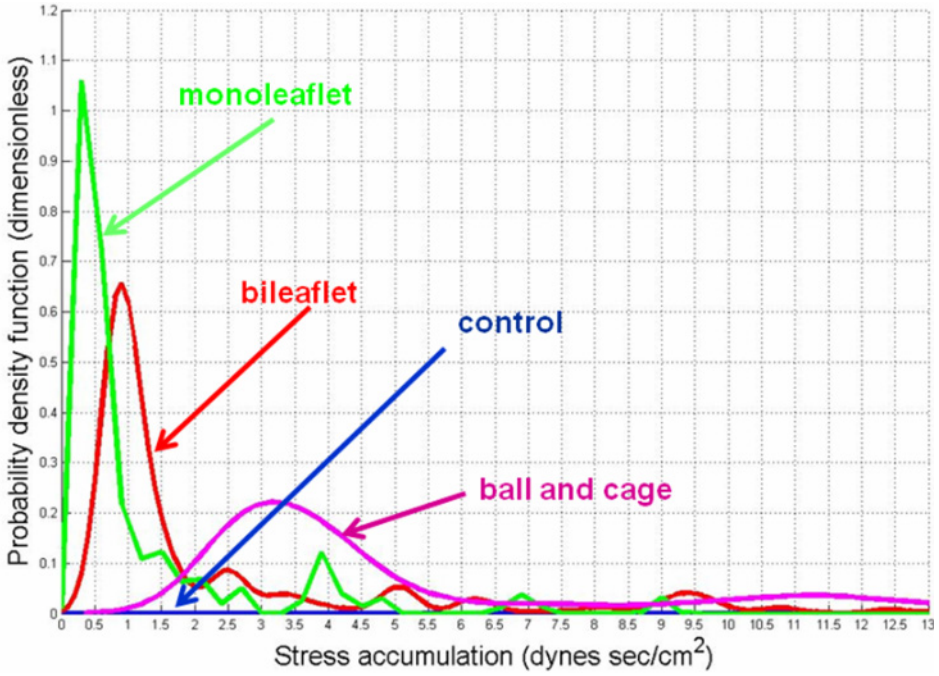

Figure 11 Stress accumulation distribution in 2D valve geometries

Discussion Velocity magnitude contour plots for valve geometries considered in this study, shown in Figure 10, reveal flow conditions and regions of high stress generated by valve geometry. Flow conditions were specific to the individual valve geometry. This was reflected in the stress accumulation distribution of the valve.

These simulations used stress accumulation distribution as bulk measure of valve performance, demonstrating its potential use for virtual valve design evaluations. The results were in line with past numerical and experimental studies from our group which used selected individual platelet trajectories to show lower amount of platelet stress exposure in monoleaflet than bileaflet valve [157].

In these validation studies, constant inlet velocity was imposed for flows through simplified 2D geometries. Results show the differences that arise in stress accumulation distribution due to geometrical features. Complex flows due to 3D valve features and the acceleration-deceleration phases of the cardiac cycles were absent in these simplified geometries. While blood is non-Newtonian multi-component fluid, two phase Newtonian representation of blood was used.

This was sufficient for the focus of this work, which is the relation between valve geometry and the flow stresses platelet experience.

In this section, the valves with markedly different geometrical features were evaluated based on their stress accumulation distribution. The possibility of this methodology to identify minor changes present in realistic MHV geometries is explored in the next section.

A.4 Comparison of two MHV designs using stress accumulation distribution – 3D simulations

The ability of platelet stress accumulation distribution to identify geometrical differences was demonstrated above in 2D geometries. In this section, stress accumulation distribution was used to compare the performance of 3D bileaflet MHV geometries from St. Jude and ATS medical. The main difference between the two valves is the design of their hinge region [7, 40].

Simulations were conducted for the open and closed positions for these two valve geometries. During the forward flow phase, the valves are in the open position and are in the closed position during the regurgitant flow phase. Identical boundary conditions, appropriate for each flow phase, were used for both valve geometries. Two-phase fluid representing blood was used in this study.

These geometries were discretized into large number of finite volume cells (>5 million), with large number of particles (>10,000) representing platelets. Scalar stress values were extracted for all particle trajectories to compute the stress accumulation distribution. These distributions were used to compare the performance of the valves.

Results Simulation results for the valves in the open position show higher velocities to be present in the ATS geometry, Figure 12. In the open position, both geometries show the presence of counter rotating vortices in slightly different locations near the hinge regions. Flow separations were shown to be present in both geometries (Figure 12).

Closed position results show stronger jet in the b-datum (gap between closed leaflets) in the ATS geometry and in the gap between the leaflet and

housing in the SJM design. Flow downstream of the leaflets resembles jet flow. Recirculation was present in these geometries, Figure 13.

Particle path data and flow conditions along each particle trajectory were extracted to calculate platelet stress accumulation. The statistical stress accumulation distribution is presented in Figure 14 and Figure 15 for forward and regurgitant flow phases respectively.

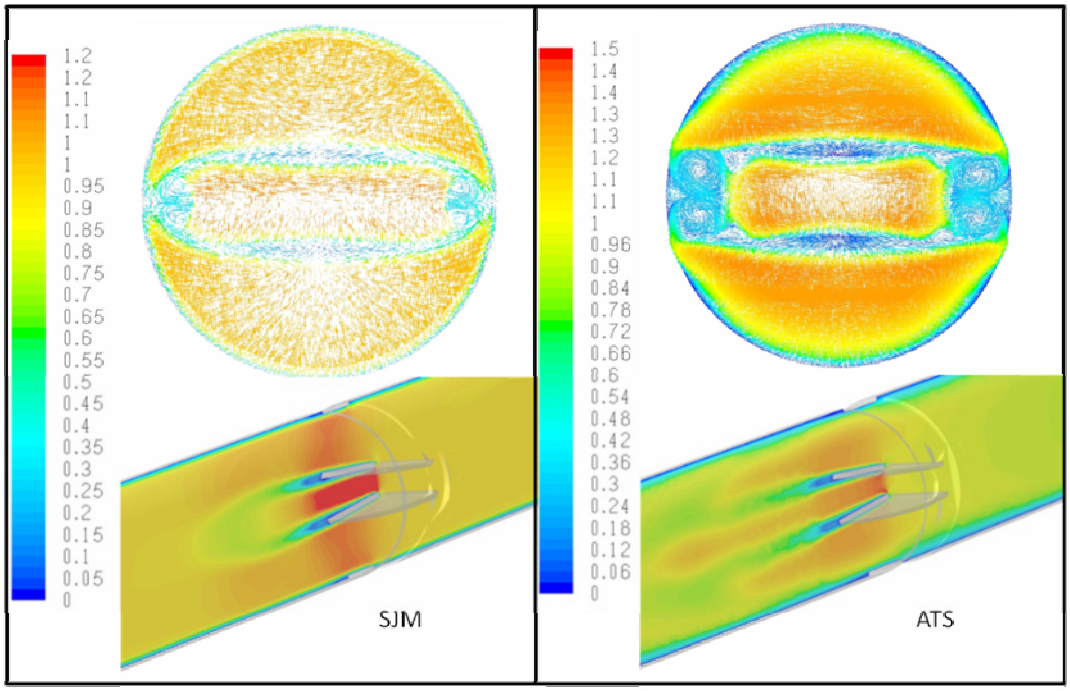

Figure 12 Velocity vectors and contour plots showing flow separations and counter rotating vortices in SJM and ATS valves

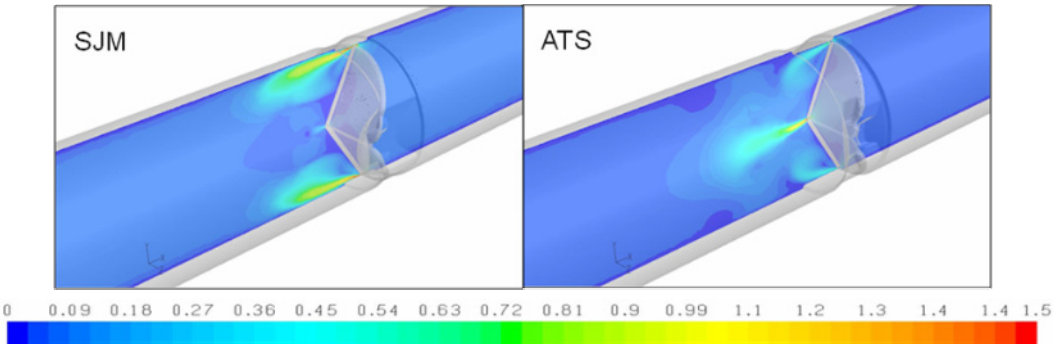

Figure 13 Velocity contour plots showing velocity jets downstream of the leaflet for the SJM and ATS valve geometries

Simulations were conducted for actual leaflet sizes. Measurements for the various components of these valves are presented in Table 2.

	SJM	ATS
Valve inner diameter [mm]	21.0	20.8
Gap clearance between hinge and leaflet [mm]	0.180	0.038
Gap clearance, closed position, leaflet and housing [mm]	0.173	0.127
B-Datum gap [mm]	0.074	0.253

Table 2 Dimensional parameters describing the SJM and ATS valve geometries

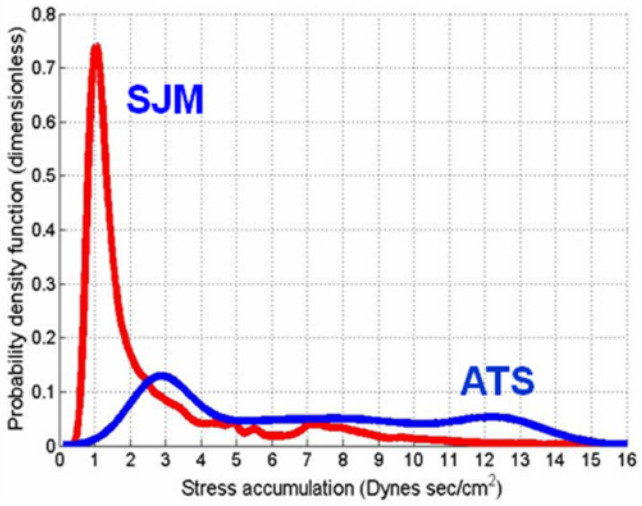

Figure 14 Comparison of stress accumulation distribution for ATS and SJM valve during forward flow phase

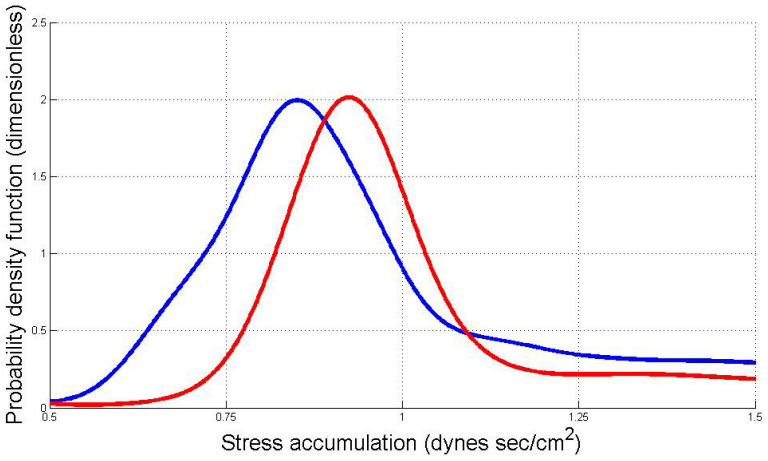

Figure 15 Stress accumulation distribution for the SJM (red) and ATS (blue) valves during regurgitant flow phase

Discussion Platelet stress accumulation distribution values for the flow phase under consideration show SJM to perform better than the ATS design during forward flow phase, Figure 14. In the regurgitant flow phase, the stress

accumulation distributions indicate ATS to offer performance advantage Figure 15. These plots show the strengths of the two valve designs.

During forward flow phase, higher velocities are present for flow through the ATS geometry, which will generate higher flow stresses. The resulting higher mean stress accumulation value during forward flow phase is due to these stresses. During the regurgitant flow phase, jets are present at the leaflet – housing gap of the SJM and the leaflet – leaflet gap (b-datum) of the ATS. These surface area offered by the ATS and SJM

Stress accumulation distributions arising from geometrical features of two valve designs were investigated. Simulations were conducted for valves placed in straight tube which may underestimate conditions due to physiologic near-valve regions and possible valve misalignment [33, 44]. The study neglected the disturbances that may arise due to leaflet motion and associated transient effects for the open and closed valve positions. Non-Newtonian blood properties, shown to amplify recirculation zones, were not considered in these studies.

Previous work from our group has shown SJM design to offers slightly better performance in the forward flow phase while ATS valve to have performance during regurgitant flow phase [150]. This improved performance may be due to the geometrical features of the SJM design which “shields/deflects” platelets from the hinge region during forward flow phase. Performance advantage of the ATS design during regurgitant flow may be due to its larger b-datum gap and shorter exposure time.

Geometries dictate the flow conditions in these valve geometries, reflected in the stresses experienced by platelets. This will be explored further in the following sections by varying aspects of the ATS valve geometry. Statistical distribution of platelet stress accumulation was used as a global performance measure of two valve geometries. Valve geometrical features such as hinge regions, specific to the valve, can be singled out to assess the resulting stress accumulation distribution. These studies are intended to demonstrate the use of stress accumulation distribution in performing parametric evaluation of changes

to the various valve geometrical features and the corresponding valve performance.

A.5 Identifying changes due to valve opening angle, hinge region and other valve features – stress accumulation distribution studies

In the previous section, the ability of platelet stress accumulation distribution to identify differences stemming from the designs of SJM and ATS valves was demonstrated. This was in agreement with previous study by our group [150]. ATS valve geometry was observed to have larger population of platelets near the hinge region than the SJM. Using this methodology, valve features, such as hinge regions can be singled out to assess region specific stress accumulation distribution. This can be useful for performing parametric studies of possible design changes to improve thrombogenic performance of the mechanical valve.

In this section, total of eight design changes of the ATS valve geometry were considered, three cases of hinge region modification, three cases dealing with gap clearance and two cases considering changes in valve opening angle. In all these cases 3 μm spherical particles representing platelets were seeded upstream. For each particle, flow stresses were extracted and used to construct the stress accumulation distribution for each design change. The results were compared against original ATS design opened to its maximum opening angle which was used as a control. Simulation results for all the design changes were correlated to our experimental Platelet Activation State (PAS) assay studies.

Design changes to ATS valve geometry. These design changes were used the ATS valve geometry, which is currently on the market and available for implantation. Goal of these studies was to explore small modifications of the current ATS design that improve thrombogenic performance.

These simulations were conducted for the forward flow phase until 300ms from peak systole (deceleration phase). Blood was represented as two-phase Newtonian fluid. For all cases, distance between leaflet and the plane from which the particles were released was identical. This was intended to eliminate

variations due seeding locations that may affect platelet stress accumulation. These geometries were discretized using 5-8 million finite volume cells containing *15,000 – 30,000* particles.

The various design changes considered in this study are presented below. Before describing these changes, the original non-modified ATS valve geometry is presented in Figure 16. The ATS geometry uses open pivot configuration which has open and closed leaflet stops, protruding into the flow field.

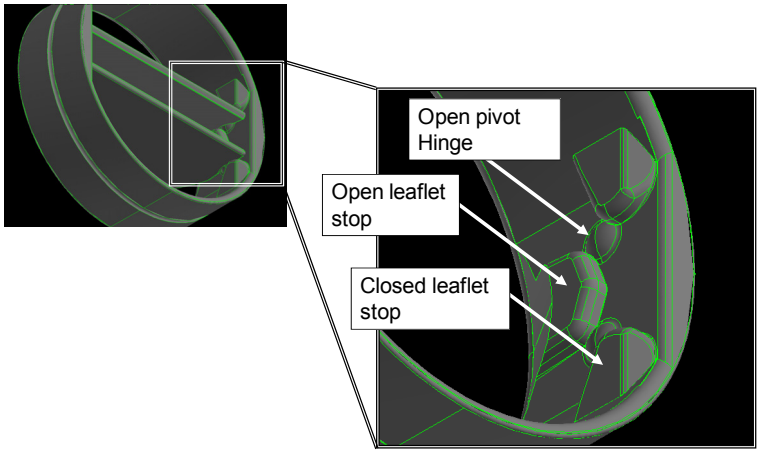

Figure 16 Original ATS geometry and features of the valve

Changes in leaflet-housing gap clearance. In the original ATS valve geometry, the gap clearance, distance between the leaflet and housing, near the hinge region is 38 μm. Studies considering changing the leaflet – housing gaps were conducted for the SJM valve [160]. In our study, this distance was increased to 130 and 250 μm to identify the contribution of gap clearance to the flow stresses experienced by platelets (Figure 17).

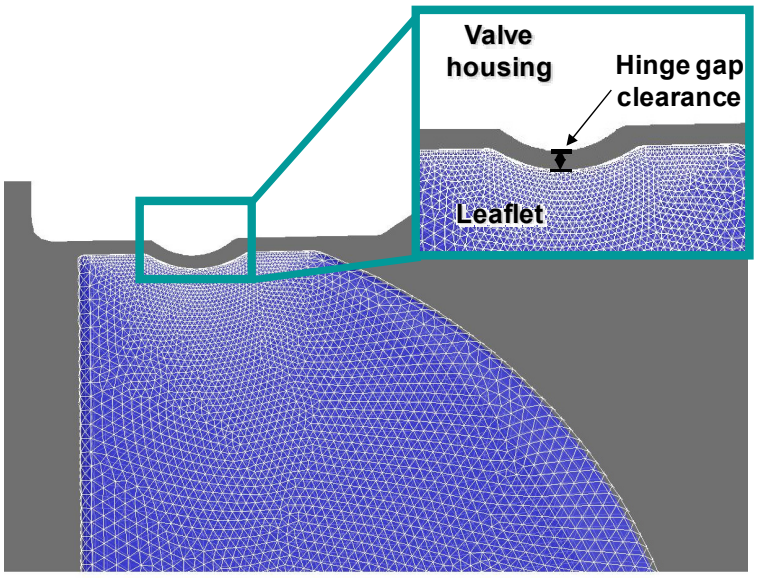

Figure 17 Valve-housing gap clearance. In this study three different gap clearance distances were considered (38, 130 and 250 μm)

Changes in valve opening angle. Platelet stress accumulation distribution resulting from changing the maximum opening angle for the ATS bileaflet valve was considered. According to the valve manufacturer, the maximum opening angle for the ATS valve is 85° which is greater than the experimentally measured value of 80° [7, 150, 161]. To investigate the role of maximum opening angle on stress accumulation distribution, two valve cases with maximum opening angles of 80° and 85° (original) were considered. Particle paths near the hinges, within region of interest (ROI), were chosen for comparing the performance of these two geometries.

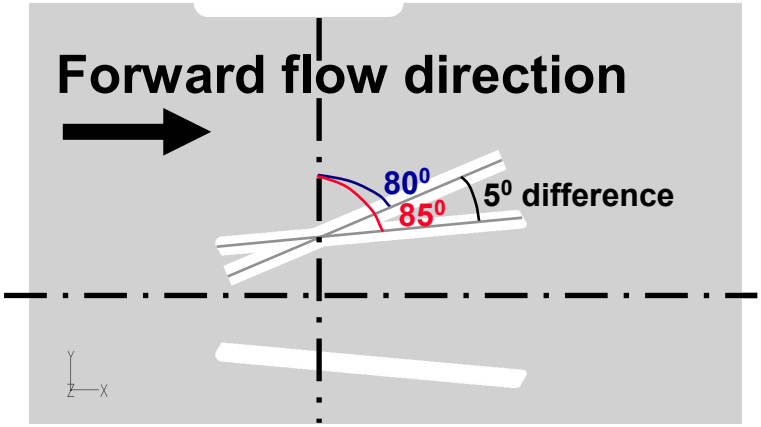

Figure 18 Maximum valve opening angle of ATS valve (80° and 85°)

In the previous sections, considering changes in gap clearance and valve opening angle maintain the general ATS valve geometry. The following sections deal with cases where material was added or removed from the valve housing.

Hinge region modifications

1. Channel below the closed leaflet stops. Some of the material was removed from the valve housing in the regions below the closed leaflet stops, Figure 19. These form streamlined channels intended to increase the flow area near the hinge regions reducing flow stresses. It also increases the flow cross-sectional area that may reduce the valve maximum velocity.

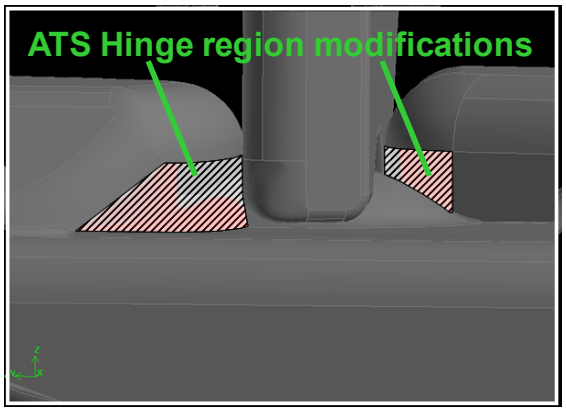

Figure 19 Modified channel below the leaflet stops

2. Diverter case 1: Diverters were added to the valve housing near the closed leaflet stops upstream of the leaflet, Figure 20. These additions protrude into the flow field and extend farther back from the original valve housing shielding the hinge region flow coming upstream of the leaflet. This may reduce the number of platelets heading to the hinge regions. Additionally, it may redirect some of the flow away from these regions.

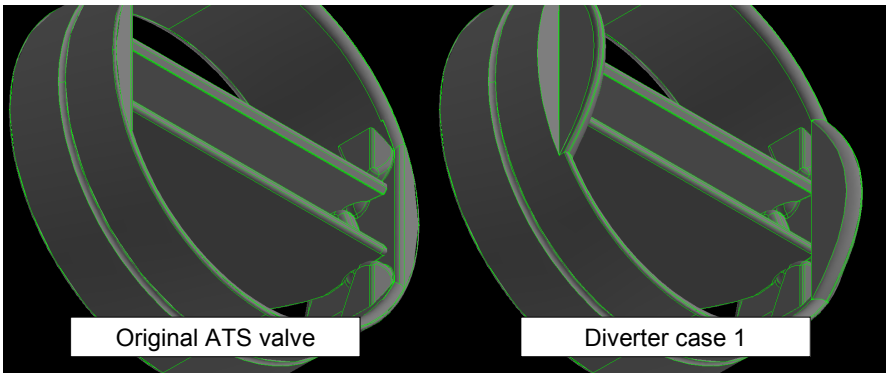

Figure 20 Diverter case 1

3. Diverter case 2: Streamlined leading edge sections were added to the valve housing upstream of the leaflet, Figure 21. This can be considered as design evolution of the Diverter case 1. This may facilitate in the formation of flow separation upstream of the hinge regions reducing the stresses for platelets that travel near the hinge regions.

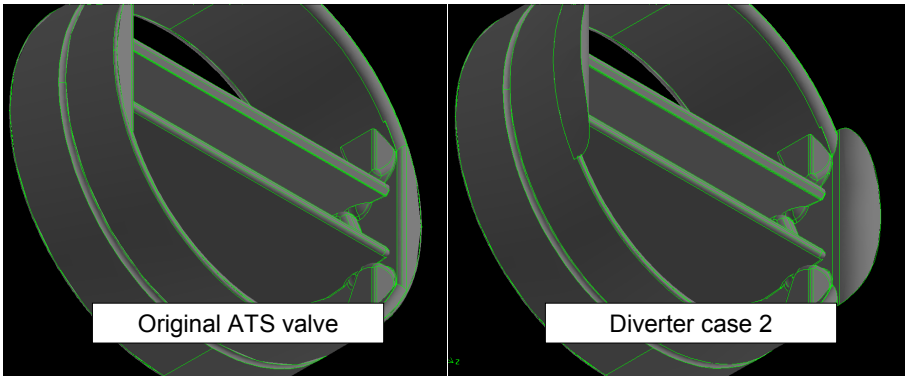

Figure 21 Diverter case 2

Results The velocity contour plots, the stress accumulation distributions and the experimental outcome due to design changes are presented in Figure 22 to Figure 25. These show regions of flow separation and recirculation zones during forward flow for the different designs. The figures also show the flow conditions which play a major role in stress accumulation of each platelet.

Changes in leaflet-housing gap clearance. Simulations were performed for 3 hinge gap clearances: 38 μm (control), 130 μm, and 250 μm (Figure 17). Stress accumulation was determined for all particle trajectories in the hinge region of interest (ROI). The stress accumulation distribution of these geometries is presented in Figure 22. These show a shift in the mean stress accumulation to

lower values as the gap clearance increases. Total stress accumulation for the 250 μm gap clearance (9.8 dyne s cm^{-2}) was lower than the 38 μm (14.97 dyne s cm^{-2}) and 130 μm (9.98 dyne s cm^{-2}) clearances ($p < 0.01$). Furthermore, stronger jets are observed in the smallest gap clearance, with shed vortices and complex flows present near the leaflet tip (Figure 22).

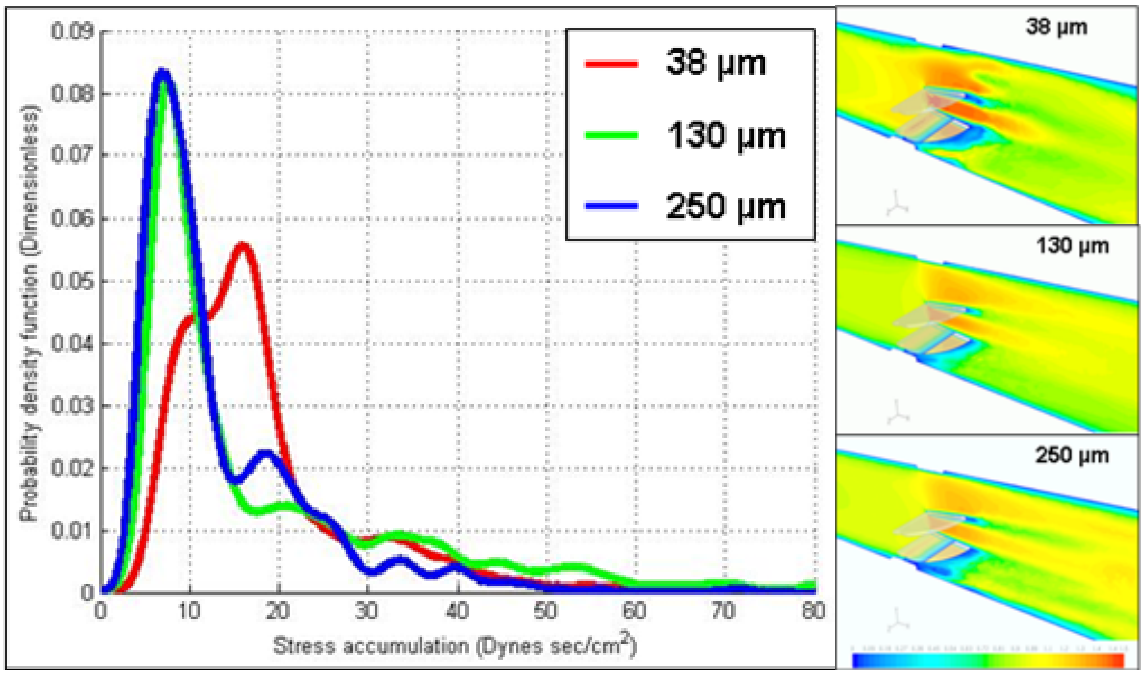

Figure 22 Stress accumulation probability densities of the three gap clearances and non parametric statistics. While not significant, total stress accumulation for the 250 μm gap clearance is lower than the 38 and 130 μm clearances

Changes in valve opening angle. Higher velocity magnitude, flow separations and stronger jets were found in the 80° opening angle (Figure 23). The 80° valve also produced larger flow separation, larger counter rotating vortices and stronger jets. The 80° ATS geometry consequently produced higher mean values of platelet stress accumulation distribution than 85° opening angle (Figure 24).

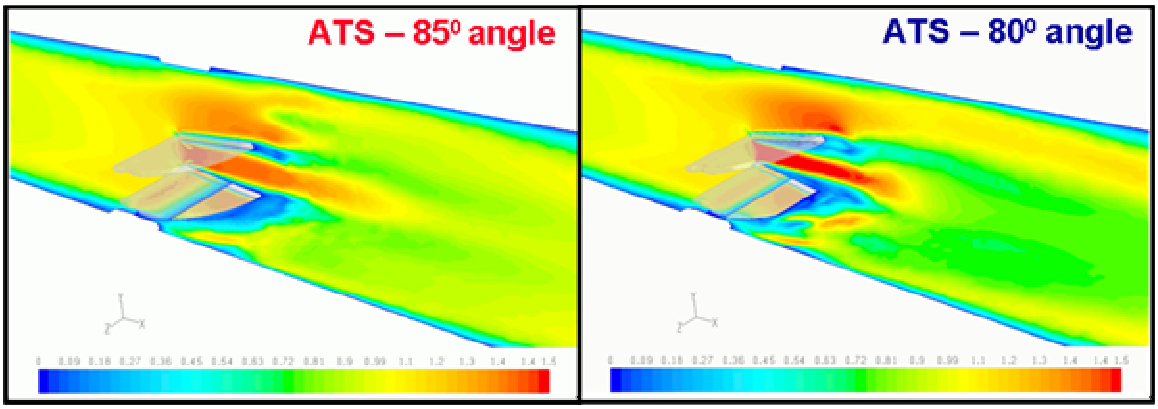

Figure 23 Velocity contour plots for 80° and 85° opening angles of ATS valve

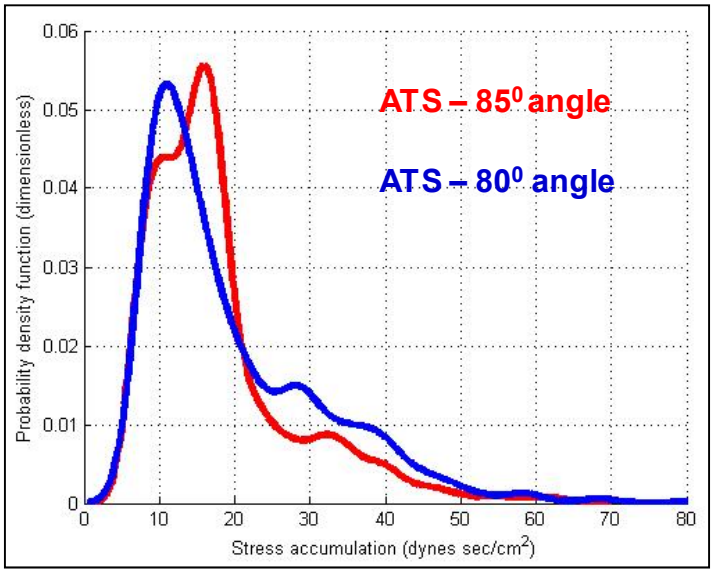

Figure 24 Stress accumulation distribution for 80° and 85° opening angles of ATS valve

Hinge region modifications. The hinge regions were farther investigated using three ATS geometry modifications. As mentioned earlier, material was removed for the first geometry consideration and for the next two cases diverters were added on the upstream side to reduce and redirect flow from the hinge regions. The results show shift in the stress accumulation distribution to lower values with the diverter case 2 offering the lowest of the three changes, Figure 25.

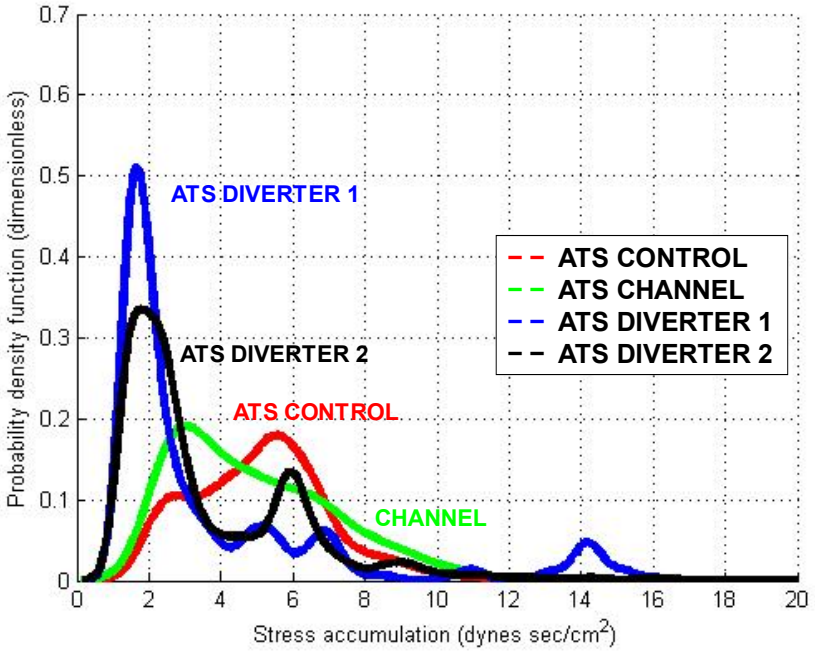

Figure 25 Stress accumulation distribution for hinge region modifications (based on Equation (16) formulation)

Discussion The stress accumulation distribution (Figure 22, Figure 24 and Figure 25), represents the flow conditions experienced by population of platelets dictated by geometry. Correlation of the stress accumulation distribution with PAS studies, describes the thrombogenic performance of the valve.

Changes in the flow conditions stemming from the opening angle affect the stress accumulation distribution, Figure 24. The failure of valve to open to the manufacturer specified maximum opening angle results in larger flow separation above the leaflet. Larger flow separation accelerates the flow due to reduced cross sectional flow area. Reduction in cross sectional area produces higher velocity gradients and higher stresses. This exposes particles to higher stresses thus moving the platelet stress accumulation distribution to higher mean value.

Gap clearance studies show the contribution of the hinge regions to impart high stress to platelets. It also shows the impact of these regions to the overall performance as evident from the results. Stress accumulation distribution presented here is not statistically significant but it shows the general trend observed dictated by the leaflet – housing gap. The smaller gap clearance may generate stronger jets increasing the platelet residence time in the counter

rotating vortices thus producing higher stress accumulation values. This trend was observed by others for SJM valve which shows arbitrary increase in gap clearance does not guarantee improved performance, indicating the existence of optimum gap clearance [160].

In the first design change case when material was removed from the stops, the flow area near these regions was increased reducing the flow stresses. This change was shown to benefit valve performance in reducing the stresses platelet experience. The second design change was able to divert flow and particles away from the high stress hinge regions. This helped to reduce the stresses platelet experience, as seen in stress accumulation distribution (Figure 25). Due to this change, the number of particles that pass through the hinge region, velocity and velocity gradient in these regions were reduced. The third design change created regions of flow separation near these hinge regions, reducing the stress accumulation for platelets navigating these regions.

Statistical comparison of the three proposed design changes and the control case also confirm that diverter case 2 provides the best solution for optimizing the ATS design (non-parametric ANOVA was performed for the statistical comparison).

These cases show the capability of stress accumulation distribution to identify differences that arise due to minor geometrical changes. They are presented as examples to guide valve designers to virtually evaluate changes for improved valve performance.

These studies into geometrical changes of the ATS valve geometry were focused on the forward flow phase. The disturbances that may arise due to leaflet motion and associated transient effects, absent in these simulations, may add to stress that platelet experience. Other phases of the cardiac cycle also contribute to the stresses experienced by platelet. During forward flow phase, the possibility of stress induced platelet damage that may lead to thromboembolic complications is high [29].

Even though the simulation was based on laminar flow assumptions, the large mesh density employed (5-8 millions finite volume cells) approaches that

required for direct numerical simulations (DNS). Additionally, these studies were for valves placed in straight tube without physiologic features such as the sinus regions that increase geometrical complications. Realistic near-valve regions and valve misalignment may amplify the differences observed in this study [33, 44, 157]. Physiologic, non-Newtonian blood properties, shown to amplify recirculation zones thus increase stress exposure time, were also neglected.

Summary of numerical studies into flow induced platelet stress and damage accumulation

Numerical simulations of flow through mechanical heart valve have previously been performed by others. These studies used simulation results as qualitative tool to study flow filed, pressure and shear stress distribution. Work outlined in this dissertation goes beyond these qualitative measures to quantify the thrombogenic potential of such devices in order to be able to optimize their performance. To achieve that, stresses that act upon individual platelet and the resulting shear induced platelet stress accumulation that can lead to activation was computed along multiple trajectories within the flow field. Geometries that produced highest stress accumulation had longer platelet residence time, resulting in higher stress accumulation values and these results agree with *in-vitro* PAS measurements performed by others in the group.

Hellums criterion, based on constant stress exposure has been the standard for determining the value of stress accumulation that results in platelet activation. However this criterion does not depict the conditions platelet experience in physiologic flow conditions. In the work of this dissertation a platelet damage model was developed to describe damage due to repeated passes an individual platelet may complete thorough high stress regions and account for its past damage.

In this dissertation, valve performance was evaluated based on stresses experienced by large number of platelet seeded in the flow domain. For these studies, highly resolved numerical meshes were constructed and were seeded with large number of particles, representing platelets. The capability of stress accumulation distribution was demonstrated to distinguish differences between

realistic valve geometries. Stress accumulation distribution as virtual design tool was demonstrated by performing design changes on specific valve geometry.

These studies used the flow conditions generated by flow domain geometries to determine the flow stresses. This was to determine the flow induced stresses platelet experience. Stress accumulation, stress and exposure time, which may lead to activation. Platelet damage model was developed to determine the relation between flow induced stresses and the possible platelet activation. Geometry of the flow domain determines the resulting flow stresses and damage platelet experience. The relation between geometry and flow induced stress accumulation can be exploited to develop methodology for MHV optimization.

The last group of studies use stress accumulation distribution, flow induced stress accumulation on platelet population, to evaluate valve performance. Flow stresses experienced by platelet population, is related to valve design and with its distinctive geometry. Stress accumulation distribution can be used to evaluate the contribution of various design changes. Design changes presented in the above studies, focused on the hinge regions of the ATS valve and the open and closed valve leaflet stops.

- Numerical simulations and DPIV measurements correlated with PAS measurements to show geometries generating higher stress accumulation also higher platelet activation.
- Numerical simulation and PAS measurements show longer residence time, observed in bileaflet valves, to produce higher stress accumulation than monoleaflet design.
- 3D simulations showed platelet trajectories with higher stress accumulation also produced higher platelet damage.
- Simulations conducted in 2D valve geometries show correlation between higher velocity gradients which result in higher flow stresses and higher mean value of stress accumulation distribution.
- Stress accumulation distribution was shown to identify design differences between realistic 3D valve geometries.

- Slight change in the maximum opening angle of a valve effects flow induced stresses and was expressed in the stress accumulation distribution.
- Stress accumulation distribution can be used as parametric design tool to numerically evaluate numerous changes in the geometrical features of valve design.
- Increasing the flow area, in general, seems to reduce the stresses platelet experience, further evidence for using numerical tools to improve valve design.

B. Numerical studies of conditions present pathologic blood vessels (Vulnerable plaque and AAA)

Pathological blood flow conditions that arise from geometrical features expose platelets to high stresses and may result in thromboembolism. This was demonstrated in the previous sections for pathological flows through MHVs. Pathological flow conditions also contribute in altering the vessel wall stresses. In diseased blood vessels, this will be amplified and may result in blood vessel rupture.

The following studies use fluid structure interaction (FSI) simulations in idealized and patient specific geometries to study the rupture risk in vulnerable plaques (VP) and abdominal aortic aneurysms (AAA). Contribution from vessel wall material composition, material properties, and geometrical features to the stresses present in the vessel wall was explored. (i) Vulnerable plaque rupture risk due to the presence of micro–calcification in the fibrous cap (ii) Inclusion of anisotropic material property and the resulting wall stresses in assessing AAA rupture risk (iii) Parametric study into the correlation of iliac bifurcation and AAA vessel wall stresses (iv) Identification of rupture locations in ruptured AAA geometry.

B.1 The role of calcification in vulnerable plaques

The role of microcalcification in affecting stresses in ideal vulnerable plaque geometries varying levels of constriction was studied [162]. Streamlined 3D eccentric stenotic geometries were constructed to study the stresses present in severe and mild stenosis cases, with 80% and 34% constrictions respectively. For each of these cases, models with and without calcification were constructed to study their contribution to the overall stress present in the vessel wall. In addition to calcification spot, these geometries were composed of healthy vessel tissue, lipid core and fluid domain Figure 26.

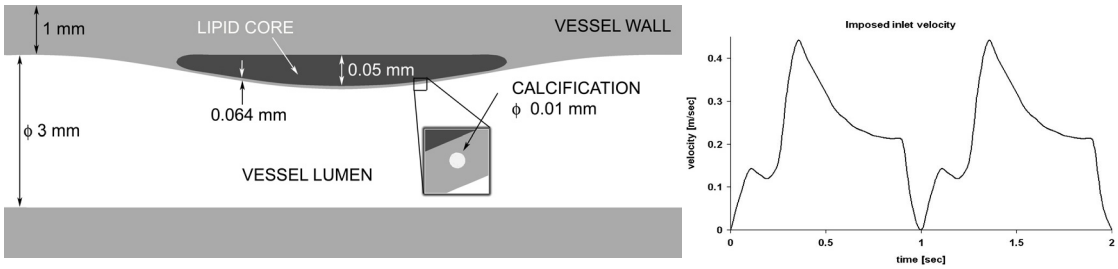

Figure 26 Mildly stenotic ideal vessel geometry identifying vessel wall, lipid core and calcification with their dimensions and imposed inlet velocity waveform

Results The peak velocity and stress values for the vulnerable plaque geometries correspond to the peak value of the inlet velocity waveform. Figure 27 shows the velocity and stress values in the transverse cross–sections of the fluid domain with recirculation zone distal to constricted region. The presence of microcalcification in the solid domain does not seem to affect the flow field.

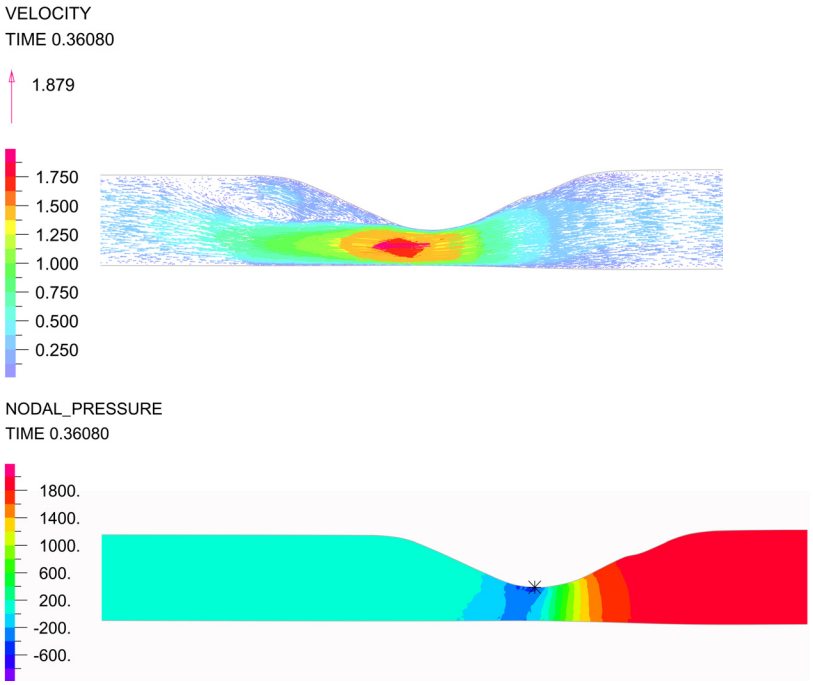

Figure 27 Velocity and stress values in the transverse cross–sections of the fluid domain[162]

On the other hand the solid domain results were sensitive to the presence of microcalcification in the fibrous cap. Figure 28 and Figure 29 show transverse cross sections for the mildly stenotic vessel. These depict stress and strain fields present in the solid domain at peak flow. The plane for the axial cross section is

through the central plane (x = 0 cm). The stress results present in these figures are Von–Misses stress, scalar value (magnitude) of the stress tensor [162].

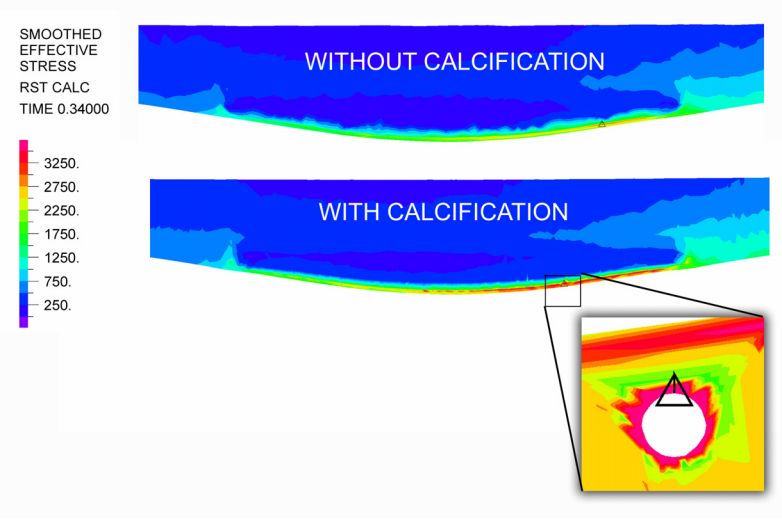

Figure 28 Peak stresses in the mildly stenotic vessel transverse cross section showing the high stresses present at the calcification–fibrous cap interface

The presence of calcification produces different responses in regions upstream and downstream of the constricted zone. The higher values of stress and strain near the calcification propagate upstream while downstream no difference was observed between the models with and without calcification. Similar trend was observed the strain distribution Figure 29.

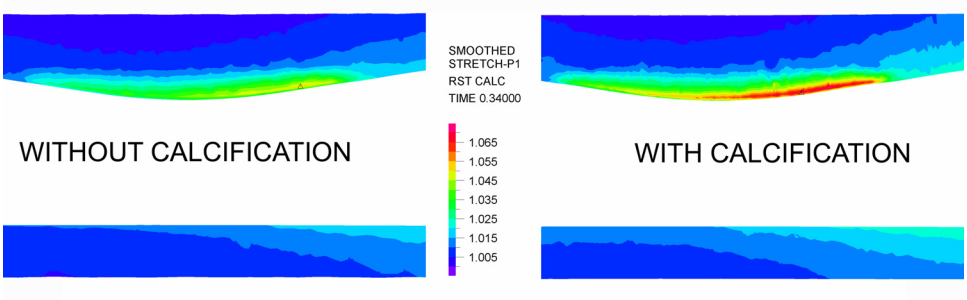

Figure 29 Transverse cross sections of the mildly stenotic vessels without and with calcification showing the peak strains

For models containing calcification spot, the maximum stress values were obtained at peak flow at the calcification–fibrous cap interface. The maximum stress values for the severe and mild stenosis cases respectively were 11.480 kPa and 2.871 kPa. The maximum principal stretches were 1.283 and 1.051 for the severe and mild stenosis cases respectively. For the geometries that contain

calcification spot, higher stress values (30.549 kPa and 5.561 kPa severe and mild stenosis cases respectively) were obtained.

At the calcification–fibrous cap interface, the highest values of stress were obtained which are about three times of the cases without calcification. From the region of high stress near the calcification, stress propagates upstream towards the plaque shoulder, and circumferentially. For the geometries without calcification spot, the maximum principal stretches were 1.410 and 1.164 for the severe and mild stenosis cases respectively.

Discussion While their role in plaque rupture is not well understood, atherosclerotic lesions are known to commonly contain calcification. When large pieces of calcification are present in the plaque seem to have stabilizing affect [89, 94]. Other studies have shown the presence of calcification to increase plaque vulnerability [95, 163]. A new hypothesis asserts vulnerable plaque rupture to be the result of stress–induced debonding of microcalcification from the surrounding tissue [95].

This theoretical model predicted two fold stress increase as the result of calcified macrophages or an iron deposits in the high stress region may cause plaque rupture if cap thickness is <65 μm, which is in close agreement of cap instability criterion [164].

In this study, 3D FSI analysis of vulnerable plaque with microcalcification was performed to obtain the stresses present within the wall of the vulnerable plaque. It shows inclusion calcification to increase stresses. This may lead to increased plaque vulnerability.

Predictions made by these simulations indicate stress concentration to be at calcification–vessel wall interface; this is in agreement with the new hypothesis for vulnerable plaque rupture due to stress–induced debonding. However the geometry used in the analytical solution by Vengrenyuk et al. was a thin planar material under unidirectional tension compared to the 3D geometry experiencing various stresses [95].

In the following sections, fluid structure interaction simulations were used to study stresses present in the abdominal aortic aneurysm vessel wall. The

relation between vessel wall stresses and anisotropic vessel wall material properties is the focus.

B.2 Risk of rupture in abdominal aortic aneurysm based on isotropic and anisotropic vessel wall models

Anisotropic vessel wall material properties of abdominal aortic aneurysms were studied using FSI tools to determine their role in AAA risk of rupture based on stress distribution [153]. Orthotropic material properties which have preferred direction of stretching, similar to aortic tissue, were used to describe the AAA tissue. The orthotropic material model constants were obtained from published material properties data for AAA determined from bi-axial tests [165].

Results Figure 30 shows the velocity vector fields in patients *A* and *B* present 0.2 seconds after peak. During the deceleration phase, the flow destabilizes resulting in formation of several recirculation zones which contribute for the increased intraluminal pressure. The peak stress values and stress values averaged over all solid elements are presented Table 3 for both patients.

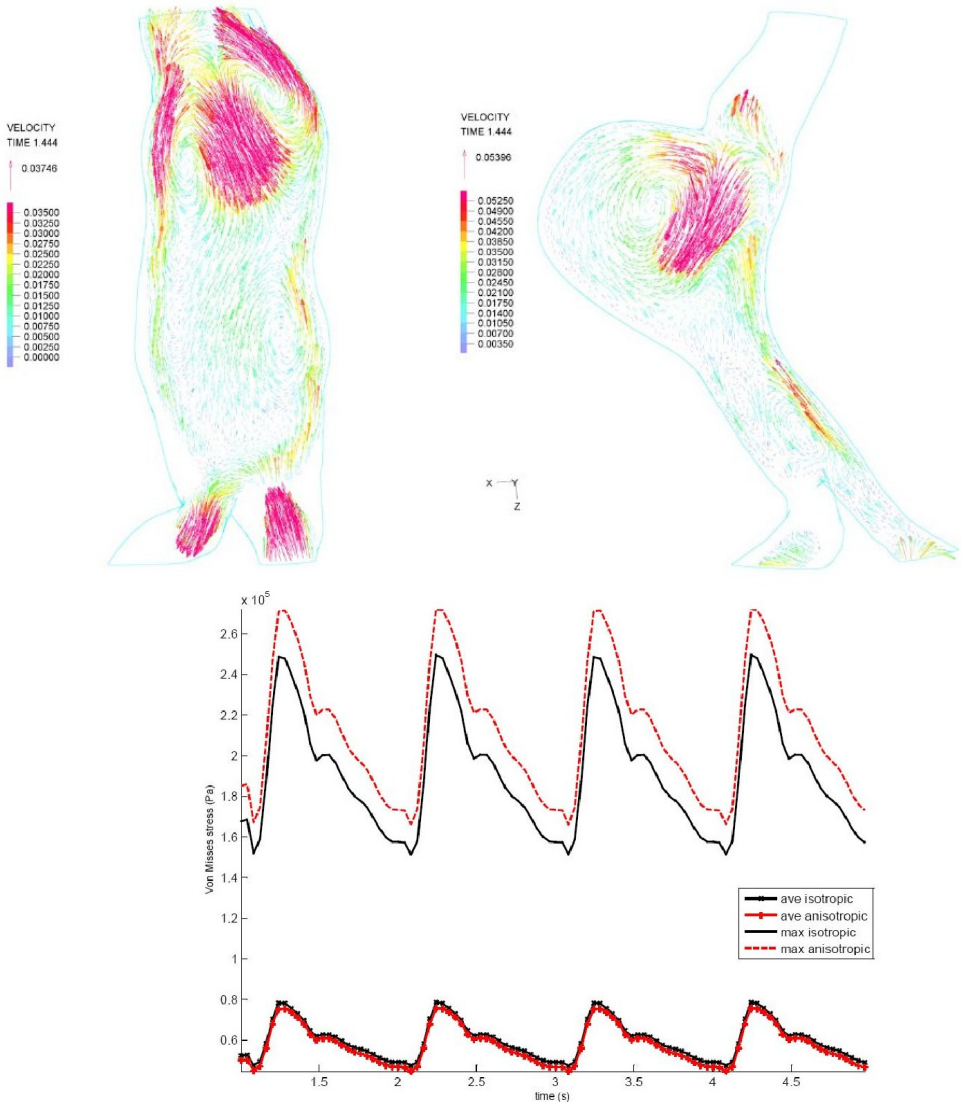

Figure 30 Velocity vectors for patient *A* and *B* geometries showing recirculation zones and Von Misses stress as a function of time averaged over the entire wall of patient *A* for anisotropic and isotropic cases [153]

For patient *A*, plot of Von Misses stress as a function of time averaged over the entire wall is presented in Figure 30. In the isotropic model, the maximum and minimum stress values were 395.2 kPa and 235.0 kPa respectively. In the anisotropic model, the maximum and minimum stress values were 414.3 kPa and 217.0 kPa respectively. The maximum average stress values for isotropic and anisotropic models were 111.8KPa and 116.6 kPa, resulting in 4% change. The respective minimums for these two material models were 69.0 kPa and 62 kPa.

In patient *B*, the isotropic model had maximum and minimum stress values of 879.5 kPa and 533.3 kPa respectively. And for the anisotropic model, the maximum and minimum stress values were 1536.5 kPa and 951.1 kPa respectively. The maximum average stress values for isotropic and anisotropic models were 78.9 KPa and 272.1 kPa, resulting in 71% change. The minimums for these two material models were 47.3 kPa and 166.4 kPa. Figure 31 shows Von Misses stresses distribution for patient *A* and *B* geometries when isotropic and anisotropic material models were employed.

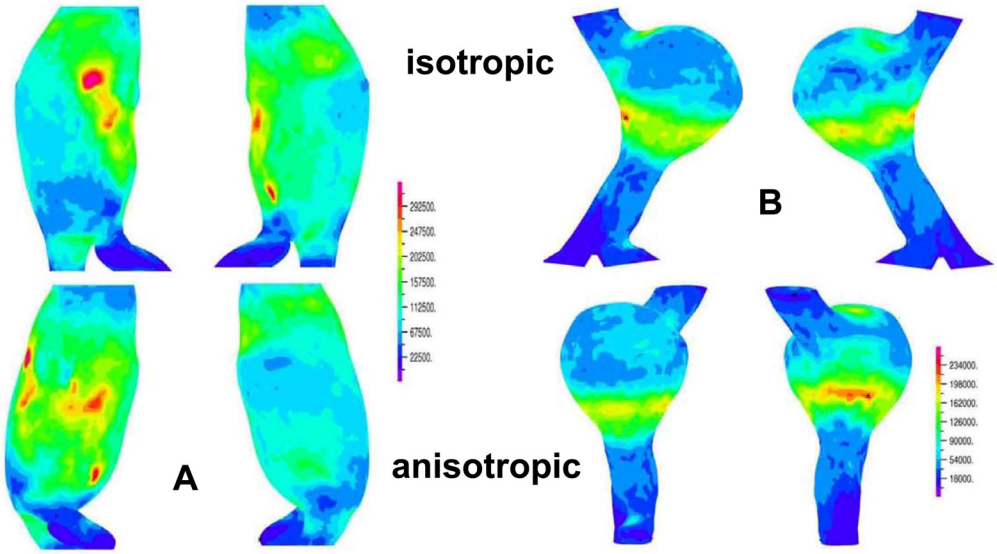

Figure 31 Stress distributions from isotropic and anisotropic simulations for patient *A* and *B* geometries [153]

Discussion Two patient specific abdominal aortic aneurysm geometries were reconstructed from clinical images to study the interaction of blood flow and resulting aortic wall stresses that may result in rupture. In this study, the wall stresses resulting from isotropic and anisotropic material models were compared. In the past, AAA numerical modeling studies used isotropic hyperelastic models [138-140, 166-167]. However, data from biaxial stretching of AAA describes wall tissue to be anisotropic [165]. Based on experimental data, orthotropic formulation [96] of anisotropic material model was employed and compared the predictions of isotropic model.

Lack of information about vessel wall thickness was limitation of this work. As the result, uniform vessel wall thickness of 2mm was constructed around patient specific AAA geometries. In addition to this the current geometry does not include calcification (this will be addressed in section B.4).

Regions of low pressure resulted in flow separations leading to the formation of various recirculation zones, present in both AAA geometries. These non–physiologic flow conditions are absent in healthy abdominal aortas. Growth and progression of the AAA may correlate with flow patterns by facilitating regions that promote the formation and growth of ILT.

The locations of high and low stresses in the AAA wall were identical for both material models. However, the values for peak stress and the range of average stresses were higher for the anisotropic material model. Using isotropic material model gave lower value for the peak stresses present in the AAA geometry underestimating the risk of rupture.

The AAA geometry displacement, movement of AAA mid region, for the anisotropic model was twice that of the isotropic model. The trends of stresses and displacements, observed in patient *A*, were similar to those of patient *B* as shown in Table 3.

	Isotropic wall material		Anisotropic wall material	
	Patient *A*	Patient *B*	Patient *A*	Patient *B*
Peak σ_{max}	395.2	249.7	414.3	272.1
Peak σ_{min}	235.0	151.3	217.0	166.4
Ave σ_{max}	111.8	78.9	116.6	75.6
Ave σ_{min}	69.0	47.3	62.0	44.6

Table 3 Maximum, minimum and average stresses present in patient A and B geometries [153]

The above sections demonstrate the role of material properties, calcification in VP and anisotropic vessel wall in AAA, to the stresses present in these pathological blood vessels. In the following section, FSI was used to study the role iliac bifurcation and neck angels to the generated stresses.

B.3 Parametric studies, iliac bifurcation and neck angles

Various AAA geometrical features from 26 reconstructed patient specific medical images (MMS software) were measured. Measured AAA features were the iliac angles, aneurysmal bending angle, tortuosity, diameters and AAA lengths. The iliac bifurcation angles were measured as the lateral bifurcation and the anterior-posterior bifurcation angle with respect to the sagittal plane. AAA was measured at the region of maximum dilation for these 25 patients.

Mean AAA diameter for these patients was 38.37mm ±7.99mm with values ranging from 28.1mm to 58.9mm. The average length was 80.74 mm ±24.43mm with values ranging between 35.4mm and 128.3mm. Other measured values are presented in Table 4.

Angulation measurements (*n*=26)	**Lateral bifurcation angle**	**Anterior bifurcation angle**	**Aortic bending angle**
Mean (degrees)	41.7	42.5	40.1
SD (degrees)	± 9.7	± 21.8	± 16.3

Table 4 Patient specific AAA measured parameters

Stresses generated due to these variations in the neck and iliac bifurcation angles were studied based on idealized AAA geometries constructed of single material with uniform 2mm wall thickness. These geometries have maximum diameter of 5cm (4.8 inner, 5.2 outer). The bifurcation angles range from $\varphi=30°$ to $\varphi=150°$ with constant length of 12.5cm from the neck to the base of the bifurcation. AAA neck angle between $\theta=0°$ to $\theta=40°$ were considered (Figure 32).

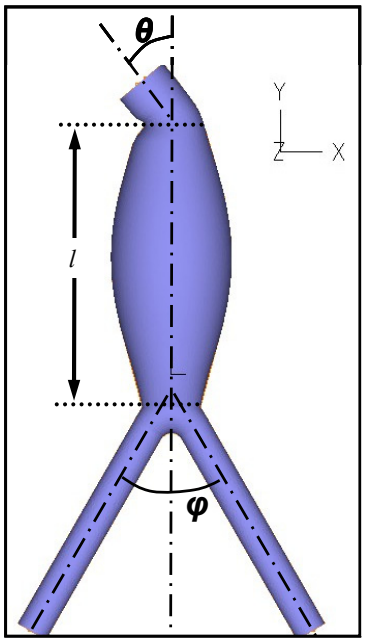

Figure 32 Idealized AAA geometry showing parameters of interest

Results Fluid flow results of these fluid structure interaction simulations show the presence of recirculation near the neck of the aneurysm. As neck angle varies from the straight the two recirculation zones combine to one larger recirculation. The aneurysmal region had uniform pressure distribution while there was pressure drop starting near the bifurcation and extending to the legs.

If the whole solid domain was under consideration, increase iliac angle shows increase in the maximum stress value. If the focus was restricted to the region of aneurysmal dilation, two local minima were observed for iliac angle of 60^o and 120^o (Figure 33). Patient specific measurements show the average iliac angle to be 42.5^0 $\pm 21.8^0$, within the range of 60^o iliac angle. Similarly, there was increase in the value of stress with increasing neck angle.

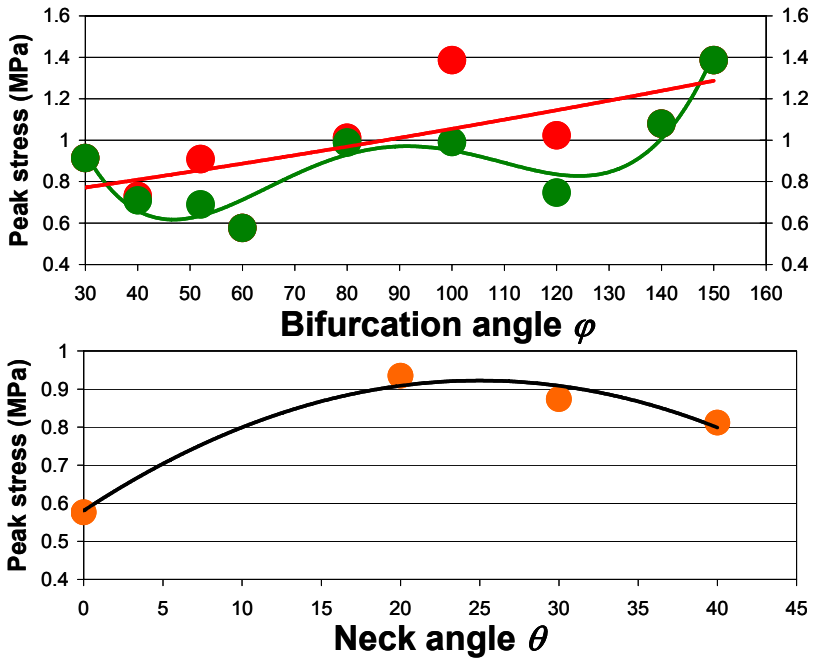

Figure 33 Vessel wall stresses due to iliac and neck angle variations in idealized AAA geometries

Discussion The focus of this work was to understand the relation between angular variations and the resulting aneurysmal wall stresses. The problem was simplified by using idealized AAA geometries that restrict angular variations into coronal plane, neglecting tortuosity and variations in neck-to-bifurcation length present in patient specific geometries. In addition to geometrical simplifications, vessel wall was composed of single material of constant thickness. The results demonstrated geometrical variations and vessel wall stresses involved in AAA rupture vulnerability.

Change in iliac bifurcation and neck angle may be physiological remodeling mechanisms attempting to reduce stresses in the aneurysmal geometry. These results, though based on ideal geometries, may be indicative of additional parameters used in evaluating rupture risk of AAA. In addition to size and growth rate, geometrical features specific to each patient, may need consideration prior to surgical intervention.

In the following section, the relation between calcification and vessel wall stresses was explored in patient specific AAA geometries.

B.4 The role of calcification in AAA

Patient specific AAA geometries were used to study the contribution of calcification to the stresses present in the aneurysm. In this FSI simulation material properties for healthy tissue, ILT and calcification were used for the solid domain and blood properties were used to represent the fluid. Physiologic pressure and velocity waveforms were applied at the inlet and outlet of the AAA geometry. Location and magnitude of maximum stress identified from this FSI simulation was used to investigate the role of calcification in AAA rupture risk.

As mentioned earlier, the objective was to find the relation between calcification that could be present in various regions of the aneurysm and the generated stresses. For this purpose, representative cases for calcification located in the healthy tissue and another embedded in ILT were chosen. For the geometry without calcification, material property of the surrounding tissue was ascribed to the volume occupied by calcification.

Results The presence of calcification in the stiffer thinner vessel wall elevated the stresses (Figure 34). However calcification present in the softer ILT resulted in minimal increase of the maximum stress [168].

Flow entering the aneurysm decelerates resulting in regions of flow separation and recirculation at different phases of the flow. Pressure throughout the aneurysmal dilation was almost uniform with higher pressures present in the iliac bifurcations.

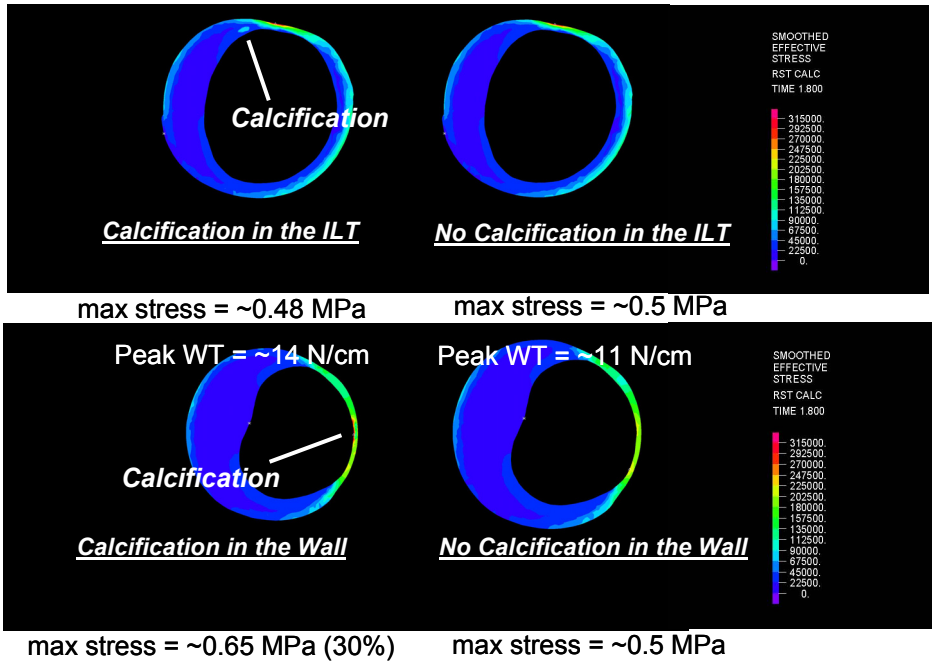

Figure 34 Stress distribution in vessels with (left) and without calcification (right)

Discussion Interactions between numerous calcified pieces that could be present and the stress propagation that may result were not considered. While patient specific AAA geometries often contain many calcified pieces, attempting to construct model with all pieces can be challenging. The propensity of calcification to elevate stresses depends on the thickness and stiffness of the surrounding tissue. If present in the thinner healthy tissue, it produces higher stresses than when located in the ILT. This is indication for the role of AAA vessel wall composition and its role in the stresses present in the aneurysm. It may be another parameter that needs to be considered in assessing AAA risk of rupture.

The relation between high stress regions and location of rupture is explored in the next section. These simulations are based on ruptured patient specific AAA geometries.

B.5 Ruptured AAA geometry

Patient specific CT scans of contained ruptures were used to construct the abdominal aortic aneurysm geometries used in this study. Anisotropic tissue material, intraluminal thrombus (ILT) and wall calcification (Ca) materials were

used to represent the vessel wall. FSI simulations were used to identify possible location of rupture based on the generated peak stresses. These were compared with actual rupture locations and peak stresses that have been reported to cause rupture. In addition to identifying location and magnitude of high stresses, ratio of the local wall stress and its estimated strength was used to calculate Rupture Potential Index (RPI).

Locations of ILT and calcification are shown in Figure 35. These are reconstructed fusiform aneurysm geometries.

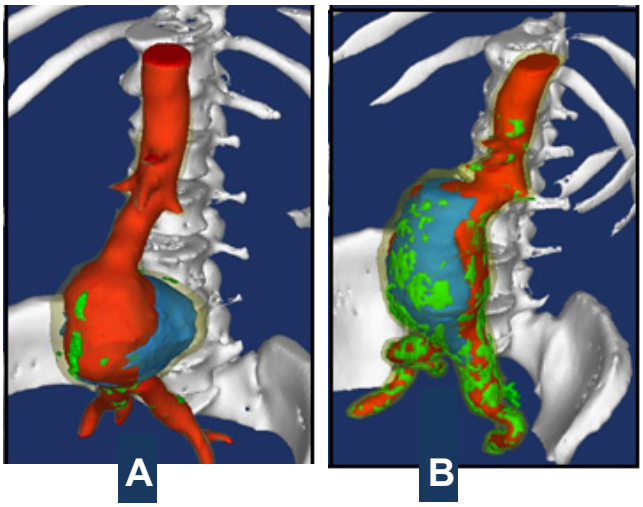

Figure 35 (A) rAAA 1 structure showing the ruptured area below the left vessel at the iliac bifurcation, (B) rAAA 2 rupture superior to the ILT along the widening inlet of the aneurysmal bulge. Lumen shown in red, skeletal bone structure in white, calcifications, green, and intraluminal thrombus (ILT) in blue and the outer wall is in yellow surrounding the lumen, ILT and calcifications.

Results The results presented in Figure 36 show the flow patterns 0.15 sec after peak systole when discernable flow patterns are present. At peak systole, the normal aortas have maximum velocity values of v_{N1} = 0.36 m/s and v_{N2} = 0.37 m/s. At diastole, the velocities drop to v_{N1} = 0.03 m/s and v_{N2} = 0.023 m/s. Simulation results show no visible recirculation zones for normal subject 1 during diastole and distinct recirculation zone for normal subject 2 due to slight widening of the lumen superior to the iliac bifurcation.

In the ruptured geometries, peak velocities were v_{rAAA1} = 0.04 m/s and v_{rAAA2} = 0.07 m/s in the aneurysmal area. For these geometries velocity at the

neck of the neck of the aneurysms were 0.36 m/s and 0.34 m/s. These values were obtained at peak systole. During diastole, large diffuse recirculation zones were present in both geometries. Velocity during diastole was v_{rAAA1} = 0.015 m/s and v_{rAAA2} = 0.023 m/s.

During peak systole, wall shear stress (WSS) distribution show the ruptured geometries to have lower values (WSS_{rAAA1} = 0.3 Pa, WSS_{rAAA2} = 0.27 Pa) compared to normal aortas (peak values WSS_{rN1} = 1.87 Pa, WSS_{rN2} 2.4 Pa). Regions close to aneurysmal necks and superior to the ILT, the WSS values were high throughout the cardiac cycle.

Results for isotropic and anisotropic simulation results are presented in Table 5 and Figure 36 B and C. Von-Mises stresses were used to represent isotropic simulation results. For the anisotropic cases, principal axis (p_1) stresses were used. These showed the trend of increasing wall stresses with the progression of the disease.

Normal aorta isotropic simulations generated maximum von Mises stress values of 0.35 MPa and 0.44 MPa. Ruptured AAA geometries produced higher stresses, with maximum von Mises stresses of $\sigma_{vM\ rAA1}$ = 1.09 MPa and $\sigma_{vM\ rAA2}$ = 2.1 MPa.

Subject	Max diam. (cm)	Peak wall stress (Isotropic, von Mises, MPa)	Peak wall stress (anisotropic, p_1 stress, MPa)	RPI
N1	1.63	0.35	0.37	--
N2	1.80	0.44	0.54	--
n-rAAA	4.60	0.50 wILT	0.65 wILT	--
		-- wILT & 1 Ca	0.70 wILT & 1 Ca	
rAAA 1	7.10	1.09 wILT	1.37 wILT	0.8
		1.23 wILT & 3 Ca	1.54 wILT & 3 Ca	
rAAA 2	4.90	2.10 wILT	2.17 wILT	0.9
		2.16 wILT & plaque Ca	2.18 wILT & plaque Ca	

Table 5 von Mises and principal axis, p_1, stresses for the normal and pathological aortas.

The anisotropic simulations follow similar trend as the isotropic studies with principal axis stresses p_1 value significantly increasing from normal to

pathological cases. Normal subjects have maximum values of p_{1N1} = 0.37 MPa and p_{1N2} = 0.54. For ruptured AAA cases, maximum values were p_{1rAAA1} = 1.37 MPa and p_{1rAAA2} = 2.17 MPa.

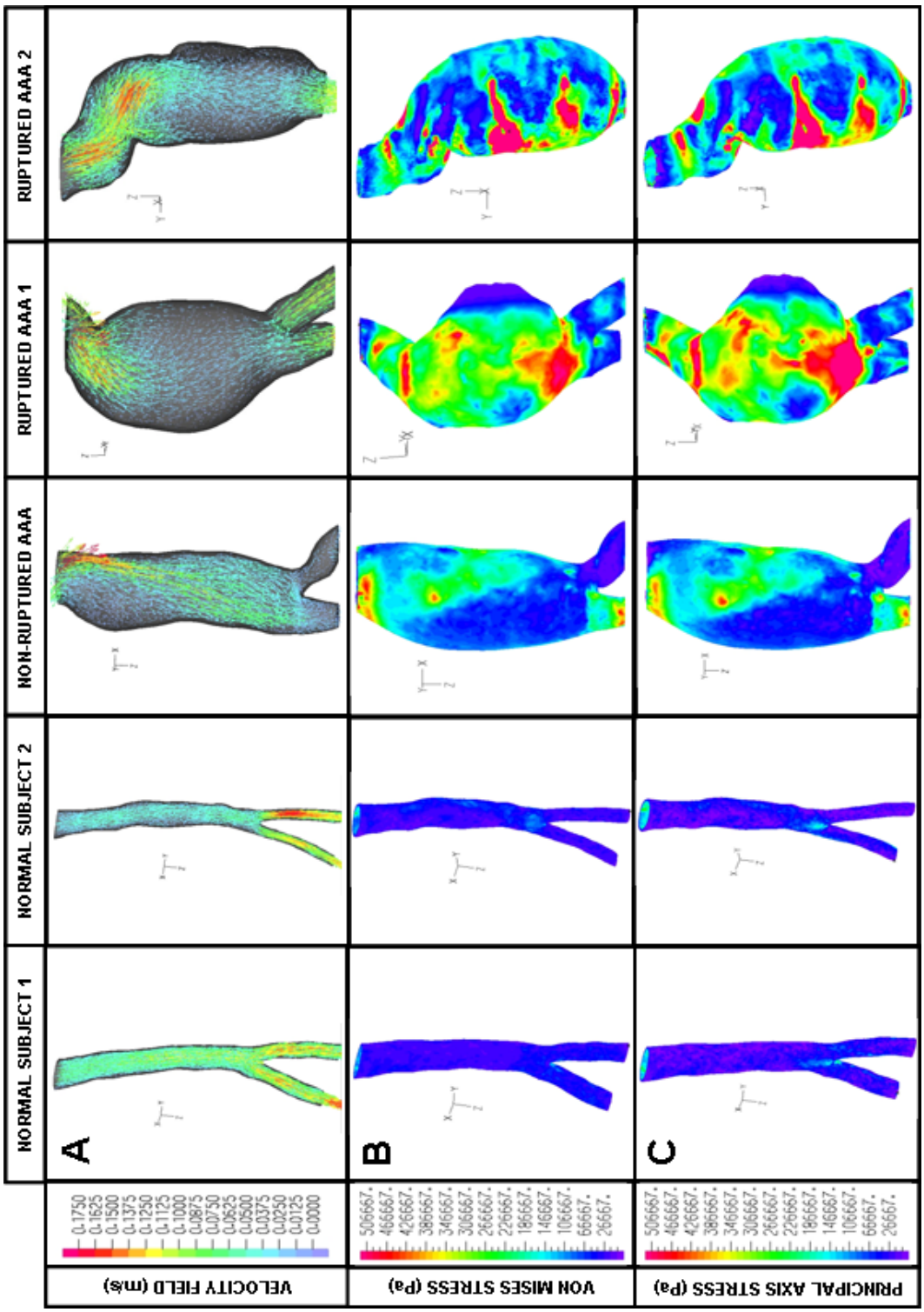

Figure 36 (A) Velocity vector fields 0.15 sec after peak systole. (B) Von Mises stress for the isotropic material model (C) Principal axis stress, p_1 for the anisotropic material model.

For the first ruptured AAA geometry, the highest stresses were along the actual rupture line Figure 37. The FSI simulation identified the location of rupture and another close to the aneurysm neck. The other location of high stress, identified from the simulation results, could be possible of secondary rupture. However, anisotropic peak stress values 1.37 MPa that occur at peak systole were prominent in the rupture area.

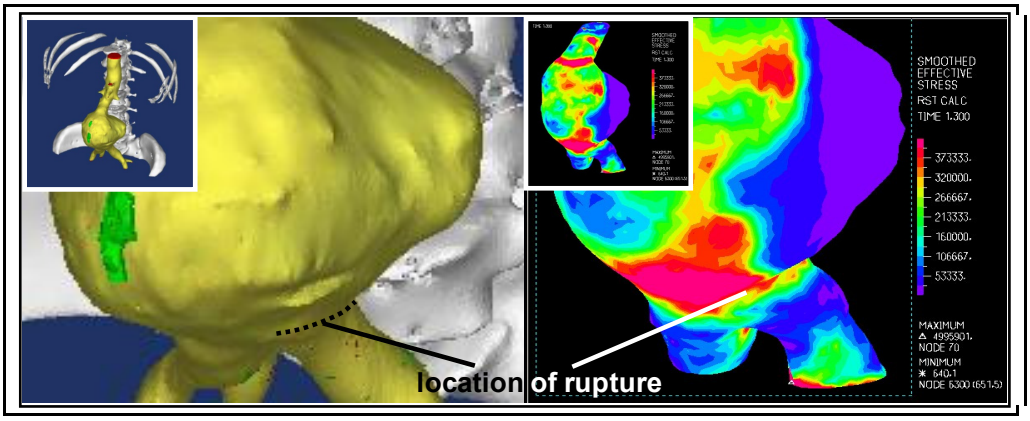

Figure 37 Maximum stress and its correlation with location of rupture

The simulation predicted regions of elevated stresses along the actual rupture line which coincided with calcification spot locations Figure 37 (left inset). Calcified spots considered in the study can be categorized into two groups. Small calcified pieces, maximum diameter less than 4.0 mm, present near rupture locations were the first group. The second group was for large plaque-like calcified regions.

In the non-ruptured AAA geometry, calcification embedded in the wall, distal to the ILT location, increased the local stress by 36.8% for the anisotropic case [168]. In the first rAAA, three calcification spots near the rupture location also increased the peak stresses by 12.8% for the isotropic case and by 12.4% for the anisotropic case. The plaque-like calcifications reduced the local wall stresses near the calcification by 21% for both material models. Summary of results into the effect of calcification are presented in Table 5.

Geometrical features and patient specific data were used to map the wall strength for geometries considered in the study Figure 38. For rAAA1, the values were from 50 to 109.2 N/cm^2 and from 68.7 to 131.6 N/cm^2 for rAAA2. Based on

local stress values, rupture potential index (RPI) was calculated as the ratio of local stress and local wall strength Figure 38. Values for RPI for both ruptured geometries were close to unity, indicating high risk of rupture. RPI values are presented in Table 5 show maximum values of RPI_{rAAA1}= 0.8 and RPI_{rAAA2} = 0.95, with at least one of the high RPI value regions coinciding with the actual location of rupture.

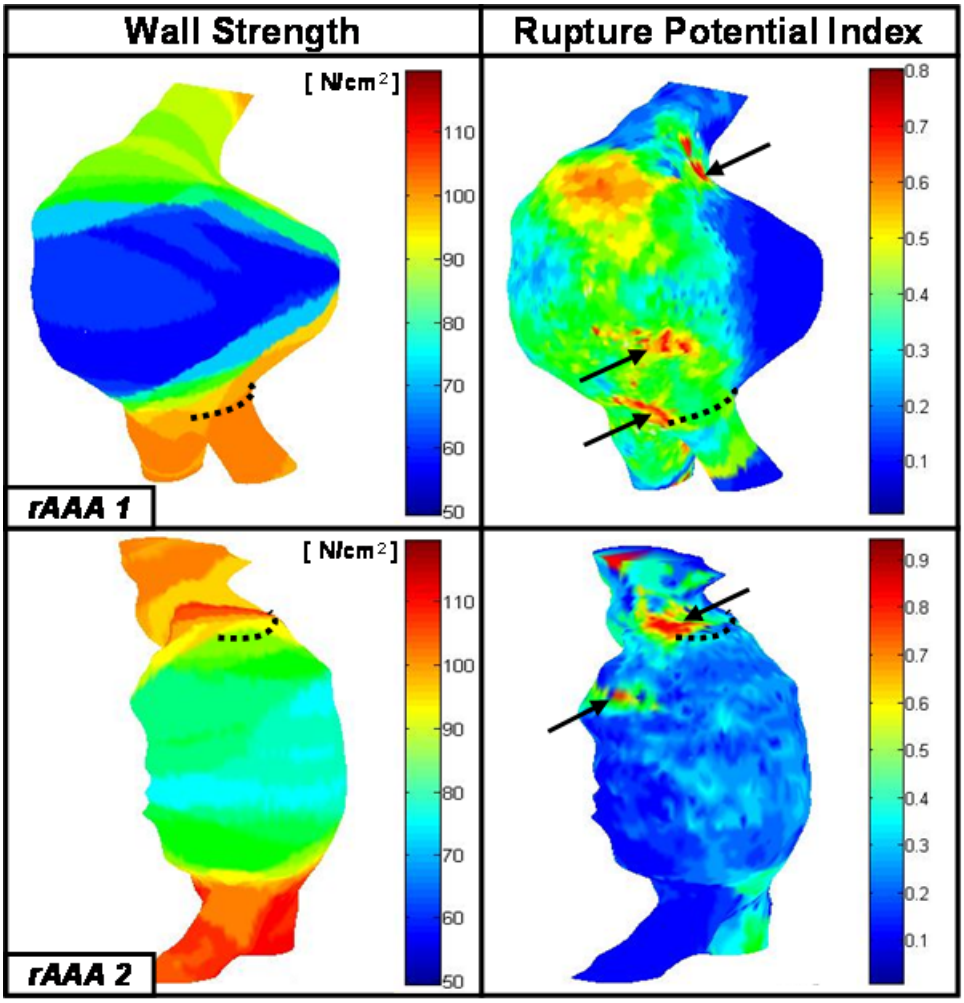

Figure 38 Wall strength estimation for the ruptured AAA and evaluation of the rupture potential index (RPI).

Discussion The ruptured geometries can be considered advanced disease state of the AAA condition. At this state, multiple high stress regions were present. Based on FSI results, locations of highest stresses identified potential to rupture sites. The peak stress at peak systole, 0.305 sec from the start of the cardiac cycle, was prominent in the actual rupture location.

From the medical images, multiple calcified pieces were known to be present in these geometries. Calcifications embedded near the rupture location appear to elevate the risk of rupture by creating stress concentrations. The large calcified pieces had the opposite effect by stiffening the wall to the local stresses.

Anisotropic simulations produced higher stresses than isotropic material representation Table 5, in agreement to our previous studies [153] and studies by other groups [140]. ILT appeared to have provided a cushioning effect, reducing the local stresses.

The ultimate goal of these studies is to quantify AAA risk of rupture by determining whether the wall actually fails. This requires weighing the local wall stress against the local wall strength. While the stresses can be extracted from the simulation, obtaining material strength requires indirect estimate of biomechanical and clinical parameters and patient specific medical history.

RPI [169], used in this study, was an attempt towards achieving this goal. Reduction in wall strength, compromising the integrity of the aneurism at the aneurysmal bulge was seen from the strength map of the aortic wall Figure 38. For both ruptured geometries, location of maximum RPI coincided with actual rupture location (indicated by a dashed line). Higher RPI value or 0.95 was obtained for the smaller, 4.9 cm, ruptured aneurysm than the larger 7.1 cm geometry with RPI value of 0.8. This was indicative for augmenting the criterion for surgical intervention solely based on the size of the aneurysm. This was in agreement with the fact that smaller aneurysms known to rupture and some larger ones could remain intact. It might aid to improve our understanding of AAA disease progression and improve our ability to quantify rupture risk.

These simulations were conducted assuming uniform wall thickness which may distort of the stress values and their distribution. The anisotropic material properties, based on specimen obtained either post mortem or during surgical procedures, were not specific to the patients considered in this study. This study only considers the mechanical stresses present in the aneurysmal geometry and did not consider the physiological and biochemical mechanisms involved in AAA wall degradation.

Results from these simulations show more than one region of elevated stress. These high stress regions and stress gradient, the distribution of stress near these regions, may indicate regions with higher rupture potential. However, understanding the relation between stress gradient and rupture will require detailed analysis the magnitude and location that produces elevated rupture potential.

The highest stresses were not at observed location of rupture. Additional mechanism such as local weakening of the vessel wall due to depleted of stiffening fibers (smooth muscle cells, elastin and collagen [118-119]) may also need to be considered. The presence of calcification as shown previously elevates the stresses. Interaction between many calcified regions and the stress propagation that may result was not considered.

Based on biomechanical considerations were shown to produce predictive capability that could improve the evaluation of AAA patients. This can spare patients from risky surgical interventions, which are currently based on size of the aneurysm. The patient specific evaluation of rupture risk, presented in this study uses FSI to evaluate the stresses within the aneurysmal wall due to the interaction of AAA geometry, hemodynamics, and the mechanical response of the aneurysmal wall.

Summary of VP and AAA numerical studies in ideal and patient specific geometries into the role of vessel wall material property and geometry

Numerical simulations have previously been used by others study conditions present in vulnerable plaque (VP) and abdominal aortic aneurysms (AAA). Most of these studies were based on either static pressurization or fluid flow studies. The studies presented in this dissertation, are all fully coupled fluid structure interaction (FSI) simulations that account for the interaction of fluid flow and vessel wall deformations, similar to conditions present in the physiologic conditions.

The presented vulnerable plaque simulations explore the role of micro calcification in altering the stresses present in the fibrous cap. These FSI studies

show the propagation of stresses near micro calcification and its contribution elevating its VP rupture risk.

Realistic blood vessel tissue is known to be anisotropic having preferred direction of stretching. In this dissertation anisotropic vessel wall properties, derived from published data, were used. While anisotropic and isotropic simulations identified similar high stress regions, the results show isotropic simulations to underpredict these stresses.

Most of these studies were based on patient specific AAA geometries that include the various vessel wall components of AAA. One study presented in this dissertation is parametric consideration of the role of iliac bifurcation and neck angle in idealized AAA geometry. These show geometrical features, in addition to aneurysmal diameter has a part in elevating stresses present in the vessel.

Past AAA numerical simulations identify possible locations of rupture from high stress present in the vessel. Some of these studies are for larger diameter AAAs at later stages of the disease process.

Numerical simulation performed at various stages of the disease process may add to our understanding into the role of mechanical stresses in the growth of aneurysms. The last group of studies presented in this dissertation considers conditions present in normal abdominal aorta and ruptured AAA geometries. For ruptured geometries rupture potential index (RPI), developed by others, that accounts for patient specific risk factors were used to augment the simulation result in assessing their risk of rupture.

The above groups of studies were based on the interaction of blood flow and solid vessel wall deformations to determine the stresses generated in the vessel wall. Physicians may be able to use the magnitude and location of high stress regions, offered by numerical simulation, to assess risk of rupture vulnerable plaque and abdominal aortic aneurysms. Pathological vessel wall conditions of vulnerable plaque and abdominal aortic aneurysm remodel the vessel geometry and alter the vessel wall composition. Both VP and AAA may contain calcifications and ILT. The presence of these components with the vessel wall remodeling alters the geometry and thus the flow conditions.

In FSI simulations, wall shear stress and pressure is transmitted to generate stresses and deformation of the solid domain. Stresses that develop in these geometries are from the contribution of vessel geometry and vessel wall material property. Realistic representation of blood vessel material property needs to consider collagen fibers and their role in generating preferred direction of stretch.

In addition to material properties, the role of geometry was studied. Parametric numerical simulations were used to study the contribution of iliac bifurcation and neck angle to the stresses generated in the vessel wall.

Lastly, the ability of numerical simulation to identify rupture location, location of material failure, was considered in reconstructed geometries of ruptured AAA. Patient specific parameters, AAA geometry and vessel wall stresses were used to construct rupture potential index.

- Presences of micro calcification in vulnerable plaques amplify the stresses in the fibrous cap and contribute to elevating rupture risk.
- Anisotropic material property produced higher stresses than isotropic material description of abdominal aortic aneurysm.
- Simulations conducted in ideal AAA geometries show correlation between iliac angle and vessel wall stress.
- Certain bifurcation angles minimize the vessel wall stresses which may reduce the vessel wall stresses and risk of rupture.
- The thinner and stiffer healthy vessel wall tissue was more sensitive to presence of calcification than ILT tissue.
- Location of AAA rupture was identified as one of the regions of high stress, indicating a correlation between high stress region and location of rupture.

IV. Conclusion

Advanced numerical tools were developed and employed to investigate challenging pathological flow problems that underlie and characterize cardiovascular diseases. These tools were used for representative cardiovascular disease conditions present in blood vessels and flow conditions present in cardiovascular devices. Conditions present in AAA and VP were used to represent pathological blood vessels and prosthetic heart valves (PHV) representing pathological flow conditions. The results from these simulations and the subsequent post processing techniques can aid optimizing the design of future cardiovascular devices and to augment clinical diagnostics of cardiovascular pathologies.

References

1. Bonow, R.O., B.A. Carabello, C. Kanu, A.C. de Leon, Jr., D.P. Faxon, M.D. Freed, W.H. Gaasch, B.W. Lytle, R.A. Nishimura, P.T. O'Gara, R.A. O'Rourke, C.M. Otto, P.M. Shah, J.S. Shanewise, S.C. Smith, Jr., A.K. Jacobs, C.D. Adams, J.L. Anderson, E.M. Antman, V. Fuster, J.L. Halperin, L.F. Hiratzka, S.A. Hunt, R. Nishimura, R.L. Page, and B. Riegel, *ACC/AHA 2006 guidelines for the management of patients with valvular heart disease: a report of the American College of Cardiology/American Heart Association Task Force on Practice Guidelines (writing committee to revise the 1998 Guidelines for the Management of Patients With Valvular Heart Disease): developed in collaboration with the Society of Cardiovascular Anesthesiologists: endorsed by the Society for Cardiovascular Angiography and Interventions and the Society of Thoracic Surgeons.* Circulation, 2006. **114**(5): p. e84-231.
2. Schoen, F.J., *Cardiac valves and valvular pathology: update on function, disease, repair, and replacement.* Cardiovasc Pathol, 2005. **14**(4): p. 189-94.
3. Yoganathan, A.P., K.B. Chandran, and F. Sotiropoulos, *Flow in prosthetic heart valves: state-of-the-art and future directions.* Ann Biomed Eng, 2005. **33**(12): p. 1689-94.
4. Gott, V.L., D.E. Alejo, and D.E. Cameron, *Mechanical heart valves: 50 years of evolution.* Ann Thorac Surg, 2003. **76**(6): p. S2230-9.
5. DeWall, R.A., N. Qasim, and L. Carr, *Evolution of mechanical heart valves.* Ann Thorac Surg, 2000. **69**(5): p. 1612-21.
6. Senthilnathan, V., T. Treasure, G. Grunkemeier, and A. Starr, *Heart valves: which is the best choice?* Cardiovasc Surg, 1999. **7**(4): p. 393--397.
7. Butany, J., M.S. Ahluwalia, C. Munroe, C. Fayet, C. Ahn, P. Blit, C. Kepron, R.J. Cusimano, and R.L. Leask, *Mechanical heart valve prostheses: identification and evaluation.* Cardiovasc Pathol, 2003. **12**(1): p. 1-22.
8. Bluestein, D., *Towards optimization of the thrombogenic potential of blood recirculating cardiovascular devices using modeling approaches.* Expert Rev Med Devices, 2006. **3**(3): p. 267-70.
9. Butchart, E.G., A. Ionescu, N. Payne, J. Giddings, G.L. Grunkemeier, and A.G. Fraser, *A new scoring system to determine thromboembolic risk after heart valve replacement.* Circulation, 2003. **108 Suppl 1**: p. II68-74.
10. Goldsmith, I., A.G.G. Turpie, and G.Y.H. Lip, *ABC of antithrombotic therapy - Valvar heart disease and prosthetic heart valves.* British Medical Journal, 2002. **325**(7374): p. 1228-1231.
11. Leytin, V., D.J. Allen, S. Mykhaylov, L. Mis, E.V. Lyubimov, B. Garvey, and J. Freedman, *Pathologic high shear stress induces apoptosis events in human platelets.* Biochem Biophys Res Commun, 2004. **320**(2): p. 303-10.

12. Hellums, J.D., *1993 Whitaker Lecture: biorheology in thrombosis research.* Ann Biomed Eng, 1994. **22**(5): p. 445-55.
13. Bluestein, D., L. Niu, R.T. Schoephoerster, and M.K. Dewanjee, *Fluid mechanics of arterial stenosis: relationship to the development of mural thrombus.* Ann Biomed Eng, 1997. **25**(2): p. 344-56.
14. Bodnar, E., *The Medtronic Parallel valve and the lessons learned.* J Heart Valve Dis, 1996. **5**(6): p. 572-3.
15. Bluestein, D.Y.W.A.K.J.J., *Flow-Induced Platelet Activation in a Mechanical Heart Valve.* J. Heart Valve Dis, 2004. **13**(No. 3): p. 501-508.
16. Boreda, R., F. Rs, and S.E. Rittgers, *Potential for platelet stimulation in critically stenosed carotid and coronary arteries.* J Vasc Invest, 1995. **1**: p. 26-37.
17. Boryczko, K., W. Dzwinel, and D.A. Yuen, *Dynamical clustering of red blood cells in capillary vessels.* J Mol Model (Online), 2003. **9**(1): p. 16-33.
18. Hellums, J.D., D.M. Peterson, N.A. Stathopoulos, J.L. Moake, and T.D. Giorgio, *Studies on the mechanisms of shear-induced platelet activation*. Hartman, A ed. Cerebral ischemia and hemorheology. 1987, New York: Springer and Verlag.
19. Shandas, R., J. Kwon, and L. Valdes-Cruz, *A method for determining the reference effective flow areas for mechanical heart valve prostheses: in vitro validation studies.* Circulation, 2000. **101**(16): p. 1953-9.
20. Fogelson, A.L., *Continuum Models of Platelet-Aggregation - Formulation and Mechanical-Properties.* Siam Journal on Applied Mathematics, 1992. **52**(4): p. 1089-1110.
21. Tuszynski, G.P., V.L. Rothman, A. Murphy, K. Siegler, and K.A. Knudsen, *Thrombospondin promotes platelet aggregation.* Blood, 1988. **72**(1): p. 109-15.
22. Merten, M., T. Chow, J.D. Hellums, and P. Thiagarajan, *A new role for P-selectin in shear-induced platelet aggregation.* Circulation, 2000. **102**(17): p. 2045-50.
23. Janes, S.L., D.J. Wilson, N. Chronos, and A.H. Goodall, *Evaluation of whole blood flow cytometric detection of platelet bound fibrinogen on normal subjects and patients with activated platelets.* Thromb Haemost, 1993. **70**(4): p. 659-66.
24. Bevers, E.M., P. Comfurius, and R.F. Zwaal, *Mechanisms involved in platelet procoagulant response.* Adv Exp Med Biol, 1993. **344**: p. 195-207.
25. Travis, B.R., H.L. Leo, P.A. Shah, D.H. Frakes, and A.P. Yoganathan, *An analysis of turbulent shear stresses in leakage flow through a bileaflet mechanical prostheses.* J Biomech Eng, 2002. **124**(2): p. 155-65.
26. Liu, J.S., P.C. Lu, and S.H. Chu, *Turbulence characteristics downstream of bileaflet aortic valve prostheses.* J Biomech Eng, 2000. **122**(2): p. 118-24.
27. Hung, T.C., R.M. Hochmuth, J.H. Joist, and S.P. Sutera, *Shear-induced aggregation and lysis of platelets.* Trans Am Soc Artif Intern Organs, 1976. **22**: p. 285-91.

28. Ramstack, J.M., L. Zuckerman, and L.F. Mockros, *Shear-induced activation of platelets.* J Biomech, 1979. **12**(2): p. 113-25.
29. Bluestein, D., Y.M. Li, and I.B. Krukenkamp, *Free emboli formation in the wake of bi-leaflet mechanical heart valves and the effects of implantation techniques.* J Biomech, 2002. **35**(12): p. 1533-40.
30. King, M.J., T. David, and J. Fisher, *Three-dimensional study of the effect of two leaflet opening angles on the time-dependent flow through a bileaflet mechanical heart valve.* Med Eng Phys, 1997. **19**(3): p. 235-41.
31. Kelly, S.G., P.R. Verdonck, J.A. Vierendeels, K. Riemslagh, E. Dick, and G.G. Van Nooten, *A three-dimensional analysis of flow in the pivot regions of an ATS bileaflet valve.* Int J Artif Organs, 1999. **22**(11): p. 754-63.
32. Krafczyk, M., M. Cerrolaza, M. Schulz, and E. Rank, *Analysis of 3D transient blood flow passing through an artificial aortic valve by Lattice-Boltzmann methods.* J Biomech, 1998. **31**(5): p. 453-62.
33. Grigioni, M., C. Daniele, C. Del Gaudio, U. Morbiducci, A. Balducci, G. D'Avenio, and V. Barbaro, *Three-dimensional numeric simulation of flow through an aortic bileaflet valve in a realistic model of aortic root.* Asaio J, 2005. **51**(3): p. 176-83.
34. Apel, J., R. Paul, S. Klaus, T. Siess, and H. Reul, *Assessment of hemolysis related quantities in a microaxial blood pump by computational fluid dynamics.* Artif Organs, 2001. **25**(5): p. 341-7.
35. Redaelli, A., H. Bothorel, E. Votta, M. Soncini, U. Morbiducci, C. Del Gaudio, A. Balducci, and M. Grigioni, *3-D simulation of the St. Jude Medical bileaflet valve opening process: fluid-structure interaction study and experimental validation.* J Heart Valve Dis, 2004. **13**(5): p. 804-13.
36. Ge, L., L.P. Dasi, F. Sotiropoulos, and A.P. Yoganathan, *Characterization of hemodynamic forces induced by mechanical heart valves: Reynolds vs. viscous stresses.* Ann Biomed Eng, 2008. **36**(2): p. 276--297.
37. Ge, L., H.L. Leo, F. Sotiropoulos, and A.P. Yoganathan, *Flow in a mechanical bileaflet heart valve at laminar and near-peak systole flow rates: CFD simulations and experiments.* J Biomech Eng, 2005. **127**(5): p. 782-97.
38. Ge, L., S.C. Jones, F. Sotiropoulos, T.M. Healy, and A.P. Yoganathan, *Numerical simulation of flow in mechanical heart valves: grid resolution and the assumption of flow symmetry.* J Biomech Eng, 2003. **125**(5): p. 709-18.
39. Krishnan, S., H.S. Udaykumar, J.S. Marshall, and K.B. Chandran, *Two-dimensional dynamic simulation of platelet activation during mechanical heart valve closure.* Ann Biomed Eng, 2006. **34**(10): p. 1519-34.
40. Dumont, K., J.A. Vierendeels, P. Segers, G.J. Van Nooten, and P.R. Verdonck, *Predicting ATS Open Pivot heart valve performance with computational fluid dynamics.* J Heart Valve Dis, 2005. **14**(3): p. 393-9.
41. Lai, Y.G., K.B. Chandran, and J. Lemmon, *A numerical simulation of mechanical heart valve closure fluid dynamics.* J Biomech, 2002. **35**(7): p. 881-92.

42. Makhijani, V.B., J.M. Siegel, and N.H.C. Hwang, *Numerical study of squeeze-flow in tilting disc mechanical heart valves.* Journal of Heart Valve Disease, 1996. **5**(1): p. 97-103.
43. Cheng, R., Y.G. Lai, and K.B. Chandran, *Three-dimensional fluid-structure interaction simulation of bileaflet mechanical heart valve flow dynamics.* Ann Biomed Eng, 2004. **32**(11): p. 1471-83.
44. Alemu, Y. and D. Bluestein, *Flow-induced platelet activation and damage accumulation in a mechanical heart valve: numerical studies.* Artif Organs, 2007. **31**(9): p. 677-88.
45. Grigioni, M., C. Daniele, G. D'Avenio, and V. Barbaro, *The influence of the leaflets' curvature on the flow field in two bileaflet prosthetic heart valves.* J Biomech, 2001. **34**(5): p. 613-21.
46. Maymir, J.C., S. Deutsch, R.S. Meyer, D.B. Geselowitz, and J.M. Tarbell, *Mean velocity and Reynolds stress measurements in the regurgitant jets of tilting disk heart valves in an artificial heart environment.* Annals of Biomedical Engineering, 1998. **26**(1): p. 146-156.
47. Chandran, K.B. and S. Aluri, *Mechanical valve closing dynamics: relationship between velocity of closing, pressure transients, and cavitation initiation.* Ann Biomed Eng, 1997. **25**(6): p. 926-38.
48. Aluri, S. and K.B. Chandran, *Numerical simulation of mechanical mitral heart valve closure.* Ann Biomed Eng, 2001. **29**(8): p. 665-76.
49. Kini, V., C. Bachmann, A. Fontaine, S. Deutsch, and J.M. Tarbell, *Flow visualization in mechanical heart valves: Occluder rebound and cavitation potential.* Annals of Biomedical Engineering, 2000. **28**(4): p. 431-441.
50. Makhijani, V.B., H.Q. Yang, A.K. Singhal, and N.H. Hwang, *An experimental-computational analysis of MHV cavitation: effects of leaflet squeezing and rebound.* J Heart Valve Dis, 1994. **3 Suppl 1**: p. S35-44; discussion S44-8.
51. Arora, D., M. Behr, and M. Pasquali, *A Tensor-based Measure for Estimating Blood Damage.* Artificial Organs, 2004. **28**(11): p. 1002-1015.
52. Pinotti, M. and E.S. Rosa, *Computational Prediction of Hemolysis in a Centrifugal Ventricular Assist Device.* Artificial Organs, 1995. **19**(3): p. 267-273.
53. Goubergrits, L. and K. Affeld, *Numerical estimation of blood damage in artificial organs.* Artif Organs, 2004. **28**(5): p. 499-507.
54. Jones, S.A., *A relationship between Reynolds stresses and viscous dissipation: implications to red cell damage.* Ann Biomed Eng, 1995. **23**(1): p. 21-8.
55. Bludszuweit, C., *Model for a general mechanical blood damage prediction.* Artif Organs, 1995. **19**(7): p. 583--589.
56. Davies, M.J. and A.C. Thomas, *Plaque fissuring--the cause of acute myocardial infarction, sudden ischaemic death, and crescendo angina.* Br Heart J, 1985. **53**(4): p. 363-73.
57. Virmani, R., F.D. Kolodgie, A.P. Burke, A. Farb, and S.M. Schwartz, *Lessons from sudden coronary death: a comprehensive morphological*

classification scheme for atherosclerotic lesions. Arterioscler Thromb Vasc Biol, 2000. **20**(5): p. 1262-75.
58. Davies, M.J., *Stability and instability: two faces of coronary atherosclerosis. The Paul Dudley White Lecture 1995.* Circulation, 1996. **94**(8): p. 2013-20.
59. Falk, E., *Why do plaques rupture?* Circulation, 1992. **86**(6 Suppl): p. III30-42.
60. Kolodgie, F.D., A.P. Burke, A. Farb, H.K. Gold, J. Yuan, J. Narula, A.V. Finn, and R. Virmani, *The thin-cap fibroatheroma: a type of vulnerable plaque: the major precursor lesion to acute coronary syndromes.* Curr Opin Cardiol, 2001. **16**(5): p. 285-92.
61. Smith, S.C., Jr., *Risk-reduction therapy: the challenge to change. Presented at the 68th scientific sessions of the American Heart Association November 13, 1995 Anaheim, California.* Circulation, 1996. **93**(12): p. 2205-11.
62. Stone, P.H., A.U. Coskun, Y. Yeghiazarians, S. Kinlay, J.J. Popma, R.E. Kuntz, and C.L. Feldman, *Prediction of sites of coronary atherosclerosis progression: In vivo profiling of endothelial shear stress, lumen, and outer vessel wall characteristics to predict vascular behavior.* Curr Opin Cardiol, 2003. **18**(6): p. 458-70.
63. Schaar, J.A., J.E. Muller, E. Falk, R. Virmani, V. Fuster, P.W. Serruys, A. Colombo, C. Stefanadis, S. Ward Casscells, P.R. Moreno, A. Maseri, and A.F. van der Steen, *Terminology for high-risk and vulnerable coronary artery plaques. Report of a meeting on the vulnerable plaque, June 17 and 18, 2003, Santorini, Greece.* Eur Heart J, 2004. **25**(12): p. 1077-82.
64. Libby, P., *Inflammation in atherosclerosis.* Nature, 2002. **420**(6917): p. 868-74.
65. Loree, H.M., R.D. Kamm, R.G. Stringfellow, and R.T. Lee, *Effects of fibrous cap thickness on peak circumferential stress in model atherosclerotic vessels.* Circ Res, 1992. **71**(4): p. 850-8.
66. MacIsaac, A.I., J.D. Thomas, and E.J. Topol, *Toward the quiescent coronary plaque.* J Am Coll Cardiol, 1993. **22**(4): p. 1228-41.
67. Richardson, P.D., M.J. Davies, and G.V. Born, *Influence of plaque configuration and stress distribution on fissuring of coronary atherosclerotic plaques.* Lancet, 1989. **2**(8669): p. 941-4.
68. Chau, A.H., R.C. Chan, M. Shishkov, B. MacNeill, N. Iftimia, G.J. Tearney, R.D. Kamm, B.E. Bouma, and M.R. Kaazempur-Mofrad, *Mechanical analysis of atherosclerotic plaques based on optical coherence tomography.* Ann Biomed Eng, 2004. **32**(11): p. 1494-503.
69. Stary, H.C., A.B. Chandler, R.E. Dinsmore, V. Fuster, S. Glagov, W. Insull, Jr., M.E. Rosenfeld, C.J. Schwartz, W.D. Wagner, and R.W. Wissler, *A definition of advanced types of atherosclerotic lesions and a histological classification of atherosclerosis. A report from the Committee on Vascular Lesions of the Council on Arteriosclerosis, American Heart Association.* Circulation, 1995. **92**(5): p. 1355-74.

70. Virmani, R., A.P. Burke, A. Farb, and F.D. Kolodgie, *Pathology of the unstable plaque.* Prog Cardiovasc Dis, 2002. **44**(5): p. 349-56.
71. Falk, E., P.K. Shah, and V. Fuster, *Coronary plaque disruption.* Circulation, 1995. **92**(3): p. 657-71.
72. Ravn, H.B. and E. Falk, *Histopathology of plaque rupture.* Cardiol Clin, 1999. **17**(2): p. 263-70, vii.
73. Lilly, L.S. and H.M. School, *Pathophysiology of heart disease : a collaborative project of medical students and faculty*. 3rd ed. 2003, Philadelphia: Lippincott Williams & Wilkins.
74. Ku, D.N., *Blood flow in arteries.* Annual Review of Fluid Mechanics, 1997. **29**: p. 399-434.
75. Wootton, D.M. and D.N. Ku, *Fluid mechanics of vascular systems, diseases, and thrombosis.* Annu Rev Biomed Eng, 1999. **1**: p. 299-329.
76. Nakashima, Y., A.S. Plump, E.W. Raines, J.L. Breslow, and R. Ross, *ApoE-deficient mice develop lesions of all phases of atherosclerosis throughout the arterial tree.* Arterioscler Thromb, 1994. **14**(1): p. 133-40.
77. Malek, A.M., S.L. Alper, and S. Izumo, *Hemodynamic shear stress and its role in atherosclerosis.* Jama, 1999. **282**(21): p. 2035-42.
78. Ross, R., *Atherosclerosis--an inflammatory disease.* N Engl J Med, 1999. **340**(2): p. 115-26.
79. Libby, P., *Current concepts of the pathogenesis of the acute coronary syndromes.* Circulation, 2001. **104**(3): p. 365-72.
80. Springer, T.A., *Traffic signals for lymphocyte recirculation and leukocyte emigration: the multistep paradigm.* Cell, 1994. **76**(2): p. 301--314.
81. Wasserman, E.J. and N.M. Shipley, *Atherothrombosis in acute coronary syndromes: mechanisms, markers, and mediators of vulnerability.* Mt Sinai J Med, 2006. **73**(1): p. 431-9.
82. Kristensen, S.D., H.B. Ravn, and E. Falk, *Insights into the pathophysiology of unstable coronary artery disease.* American Journal of Cardiology, 1997. **80**: p. E5-E9.
83. Corti, R. and J.J. Badimon, *Biologic aspects of vulnerable plaque.* Curr Opin Cardiol, 2002. **17**(6): p. 616-25.
84. Libby, P., *What happens inside an atherosclerotic plaque?* International Congress Series, 2004. **1262**: p. 253-256.
85. Shah, P.K., *Mechanisms of plaque vulnerability and rupture.* J Am Coll Cardiol, 2003. **41**(4 Suppl S): p. 15S-22S.
86. Schroeder, A.P. and E. Falk, *Vulnerable and dangerous coronary plaques.* Atherosclerosis, 1995. **118 Suppl**: p. S141-9.
87. Agrotis, A., N. Kalinina, and A. Bobik, *Transforming growth factor-beta, cell signaling and cardiovascular disorders.* Curr Vasc Pharmacol, 2005. **3**(1): p. 55-61.
88. Werb, Z., M.J. Banda, and P.A. Jones, *Degradation of connective tissue matrices by macrophages. I. Proteolysis of elastin, glycoproteins, and collagen by proteinases isolated from macrophages.* J Exp Med, 1980. **152**(5): p. 1340--1357.

89. Cheng, G.C., H.M. Loree, R.D. Kamm, M.C. Fishbein, and R.T. Lee, *Distribution of circumferential stress in ruptured and stable atherosclerotic lesions. A structural analysis with histopathological correlation.* Circulation, 1993. **87**(4): p. 1179-87.
90. Lee, R.T., H.M. Loree, G.C. Cheng, E.H. Lieberman, N. Jaramillo, and F.J. Schoen, *Computational structural analysis based on intravascular ultrasound imaging before in vitro angioplasty: prediction of plaque fracture locations.* J Am Coll Cardiol, 1993. **21**(3): p. 777-82.
91. Corti, R., M.E. Farkouh, and J.J. Badimon, *The vulnerable plaque and acute coronary syndromes.* Am J Med, 2002. **113**(8): p. 668-80.
92. Feldman, C.L. and P.H. Stone, *Intravascular hemodynamic factors responsible for progression of coronary atherosclerosis and development of vulnerable plaque.* Curr Opin Cardiol, 2000. **15**(6): p. 430-40.
93. Richardson, P.D., *Biomechanics of plaque rupture: progress, problems, and new frontiers.* Ann Biomed Eng, 2002. **30**(4): p. 524-36.
94. Huang, H., R. Virmani, H. Younis, A.P. Burke, R.D. Kamm, and R.T. Lee, *The impact of calcification on the biomechanical stability of atherosclerotic plaques.* Circulation, 2001. **103**(8): p. 1051-6.
95. Vengrenyuk, Y., S. Carlier, S. Xanthos, L. Cardoso, P. Ganatos, R. Virmani, S. Einav, L. Gilchrist, and S. Weinbaum, *A hypothesis for vulnerable plaque rupture due to stress-induced debonding around cellular microcalcifications in thin fibrous caps.* Proc Natl Acad Sci U S A, 2006. **103**(40): p. 14678-83.
96. Holzapfel, G.A., T.C. Gasser, and R.W. Ogden, *A new constitutive framework for arterial wall mechanics and a comparative study of material models.* Journal of Elasticity, 2000. **61**(1-3): p. 1-48.
97. Tang, D., C. Yang, J. Zheng, P.K. Woodard, G.A. Sicard, J.E. Saffitz, and C. Yuan, *3D MRI-based multicomponent FSI models for atherosclerotic plaques.* Ann Biomed Eng, 2004. **32**(7): p. 947-60.
98. Doyle, B.J., P.A. Grace, E.G. Kavanagh, P.E. Burke, F. Wallis, M.T. Walsh, and T.M. McGloughlin, *Improved assessment and treatment of abdominal aortic aneurysms: the use of 3D reconstructions as a surgical guidance tool in endovascular repair.* Ir J Med Sci, 2009. **178**(3): p. 321-8.
99. Vorp, D.A. and J.P. Vande Geest, *Biomechanical determinants of abdominal aortic aneurysm rupture.* Arterioscler Thromb Vasc Biol, 2005. **25**(8): p. 1558-66.
100. Raghavan, M.L., D.A. Vorp, M.P. Federle, M.S. Makaroun, and M.W. Webster, *Wall stress distribution on three-dimensionally reconstructed models of human abdominal aortic aneurysm.* J Vasc Surg, 2000. **31**(4): p. 760-9.
101. Finet, G., J. Ohayon, and G. Rioufol, *Biomechanical interaction between cap thickness, lipid core composition and blood pressure in vulnerable coronary plaque: impact on stability or instability.* Coron Artery Dis, 2004. **15**(1): p. 13-20.
102. Versluis, A., A.J. Bank, and W.H. Douglas, *Fatigue and plaque rupture in myocardial infarction.* J Biomech, 2006. **39**(2): p. 339-47.

103. Yang, C., D. Tang, S. Kobayashi, J. Zheng, P.K. Woodard, Z. Teng, R. Bach, and D.N. Ku, *Cyclic Bending Contributes to High Stress in a Human Coronary Atherosclerotic Plaque and Rupture Risk: In Vitro Experimental Modeling and Ex Vivo MRI-Based Computational Modeling Approach.* Mol Cell Biomech, 2008. **5**(4): p. 259-274.
104. Vardulaki, K.A., N.M. Walker, N.E. Day, S.W. Duffy, H.A. Ashton, and R.A. Scott, *Quantifying the risks of hypertension, age, sex and smoking in patients with abdominal aortic aneurysm.* Br J Surg, 2000. **87**(2): p. 195-200.
105. Brown, L.C. and J.T. Powell, *Risk factors for aneurysm rupture in patients kept under ultrasound surveillance. UK Small Aneurysm Trial Participants.* Ann Surg, 1999. **230**(3): p. 289-96; discussion 296-7.
106. Blanchard, J.F., H.K. Armenian, and P.P. Friesen, *Risk factors for abdominal aortic aneurysm: results of a case-control study.* Am J Epidemiol, 2000. **151**(6): p. 575-83.
107. Lindholt, J.S., N.H. Heegaard, S. Vammen, H. Fasting, E.W. Henneberg, and L. Heickendorff, *Smoking, but not lipids, lipoprotein(a) and antibodies against oxidised LDL, is correlated to the expansion of abdominal aortic aneurysms.* Eur J Vasc Endovasc Surg, 2001. **21**(1): p. 51-6.
108. Lederle, F.A., G.R. Johnson, and S.E. Wilson, *Abdominal aortic aneurysm in women.* J Vasc Surg, 2001. **34**(1): p. 122-6.
109. Singh, K., K.H. Bonaa, B.K. Jacobsen, L. Bjork, and S. Solberg, *Prevalence of and risk factors for abdominal aortic aneurysms in a population-based study : The Tromso Study.* Am J Epidemiol, 2001. **154**(3): p. 236-44.
110. Brady, A.R., S.G. Thompson, F.G. Fowkes, R.M. Greenhalgh, and J.T. Powell, *Abdominal aortic aneurysm expansion: risk factors and time intervals for surveillance.* Circulation, 2004. **110**(1): p. 16-21.
111. Thompson, R.W., P.J. Geraghty, and J.K. Lee, *Abdominal aortic aneurysms: basic mechanisms and clinical implications.* Curr Probl Surg, 2002. **39**(2): p. 110-230.
112. Alcorn, H.G., S.K. Wolfson, Jr., K. Sutton-Tyrrell, L.H. Kuller, and D. O'Leary, *Risk factors for abdominal aortic aneurysms in older adults enrolled in The Cardiovascular Health Study.* Arterioscler Thromb Vasc Biol, 1996. **16**(8): p. 963-70.
113. Juvela, S., K. Poussa, and M. Porras, *Factors affecting formation and growth of intracranial aneurysms: a long-term follow-up study.* Stroke, 2001. **32**(2): p. 485-91.
114. Wanhainen, A., D. Bergqvist, K. Boman, T.K. Nilsson, J. Rutegard, and M. Bjorck, *Risk factors associated with abdominal aortic aneurysm: a population-based study with historical and current data.* J Vasc Surg, 2005. **41**(3): p. 390-6.
115. Thompson, R.W., *Detection and management of small aortic aneurysms.* N Engl J Med, 2002. **346**(19): p. 1484-6.
116. Gillum, R.F., *Epidemiology of aortic aneurysm in the United States.* J Clin Epidemiol, 1995. **48**(11): p. 1289-98.

117. Lederle, F.A., G.R. Johnson, S.E. Wilson, E.P. Chute, F.N. Littooy, D. Bandyk, W.C. Krupski, G.W. Barone, C.W. Acher, and D.J. Ballard, *Prevalence and associations of abdominal aortic aneurysm detected through screening. Aneurysm Detection and Management (ADAM) Veterans Affairs Cooperative Study Group.* Ann Intern Med, 1997. **126**(6): p. 441-9.
118. Holmes, D.R., S. Liao, W.C. Parks, and R.W. Thompson, *Medial neovascularization in abdominal aortic aneurysms: a histopathologic marker of aneurysmal degeneration with pathophysiologic implications.* J Vasc Surg, 1995. **21**(5): p. 761-71; discussion 771-2.
119. Shah, P.K., *Inflammation, metalloproteinases, and increased proteolysis: an emerging pathophysiological paradigm in aortic aneurysm.* Circulation, 1997. **96**(7): p. 2115-7.
120. Crawford, E.S. and E.S. Cohen, *Aortic aneurysm: a multifocal disease. Presidential address.* Arch Surg, 1982. **117**(11): p. 1393-400.
121. Wolinsky, H. and S. Glagov, *A lamellar unit of aortic medial structure and function in mammals.* Circ Res, 1967. **20**(1): p. 99-111.
122. Lopez-Candales, A., D.R. Holmes, S. Liao, M.J. Scott, S.A. Wickline, and R.W. Thompson, *Decreased vascular smooth muscle cell density in medial degeneration of human abdominal aortic aneurysms.* Am J Pathol, 1997. **150**(3): p. 993-1007.
123. Lakatta, E.G., J.H. Mitchell, A. Pomerance, and G.G. Rowe, *Human aging: changes in structure and function.* J Am Coll Cardiol, 1987. **10**(2 Suppl A): p. 42A--47A.
124. Baxter, B.T., G.S. McGee, V.P. Shively, I.A. Drummond, S.N. Dixit, M. Yamauchi, and W.H. Pearce, *Elastin content, cross-links, and mRNA in normal and aneurysmal human aorta.* J Vasc Surg, 1992. **16**(2): p. 192-200.
125. Sakalihasan, N., A. Heyeres, B.V. Nusgens, R. Limet, and C.M. Lapiere, *Modifications of the extracellular matrix of aneurysmal abdominal aortas as a function of their size.* Eur J Vasc Surg, 1993. **7**(6): p. 633-7.
126. Herron, G.S., E. Unemori, M. Wong, J.H. Rapp, M.H. Hibbs, and R.J. Stoney, *Connective tissue proteinases and inhibitors in abdominal aortic aneurysms. Involvement of the vasa vasorum in the pathogenesis of aortic aneurysms.* Arterioscler Thromb, 1991. **11**(6): p. 1667-77.
127. Longo, G.M., W. Xiong, T.C. Greiner, Y. Zhao, N. Fiotti, and B.T. Baxter, *Matrix metalloproteinases 2 and 9 work in concert to produce aortic aneurysms.* J Clin Invest, 2002. **110**(5): p. 625--632.
128. Pyo, R., J.K. Lee, J.M. Shipley, J.A. Curci, D. Mao, S.J. Ziporin, T.L. Ennis, S.D. Shapiro, R.M. Senior, and R.W. Thompson, *Targeted gene disruption of matrix metalloproteinase-9 (gelatinase B) suppresses development of experimental abdominal aortic aneurysms.* J Clin Invest, 2000. **105**(11): p. 1641--1649.
129. Allaire, E., R. Forough, M. Clowes, B. Starcher, and A.W. Clowes, *Local overexpression of TIMP-1 prevents aortic aneurysm degeneration and rupture in a rat model.* J Clin Invest, 1998. **102**(7): p. 1413--1420.

130. Sakalihasan, N., R. Limet, and O.D. Defawe, *Abdominal aortic aneurysm.* Lancet, 2005. **365**(9470): p. 1577--1589.
131. Schermerhorn, M.L., S.R.G. Finlayson, M.F. Fillinger, J. Buth, C. van Marrewijk, and J.L. Cronenwett, *Life expectancy after endovascular versus open abdominal aortic aneurysm repair: results of a decision analysis model on the basis of data from EUROSTAR.* J Vasc Surg, 2002. **36**(6): p. 1112--1120.
132. Cronenwett, J.L., T.F. Murphy, G.B. Zelenock, W.M. Whitehouse, Jr., S.M. Lindenauer, L.M. Graham, L.E. Quint, T.M. Silver, and J.C. Stanley, *Actuarial analysis of variables associated with rupture of small abdominal aortic aneurysms.* Surgery, 1985. **98**(3): p. 472-83.
133. Darling, R.C., C.R. Messina, D.C. Brewster, and L.W. Ottinger, *Autopsy study of unoperated abdominal aortic aneurysms. The case for early resection.* Circulation, 1977. **56**(3 Suppl): p. II161-4.
134. Nicholls, S.C., J.B. Gardner, M.H. Meissner, and H.K. Johansen, *Rupture in small abdominal aortic aneurysms.* J Vasc Surg, 1998. **28**(5): p. 884-8.
135. Fillinger, M.F., J. Racusin, R.K. Baker, J.L. Cronenwett, A. Teutelink, M.L. Schermerhorn, R.M. Zwolak, R.J. Powell, D.B. Walsh, and E.M. Rzucidlo, *Anatomic characteristics of ruptured abdominal aortic aneurysm on conventional CT scans: Implications for rupture risk.* J Vasc Surg, 2004. **39**(6): p. 1243-52.
136. Simpson, C.F., *Sotalol for the protection of turkeys from the development of -aminopropionitrile-induced aortic ruptures.* Br J Pharmacol, 1972. **45**(3): p. 385--390.
137. Wolters, B.J., M.C. Rutten, G.W. Schurink, U. Kose, J. de Hart, and F.N. van de Vosse, *A patient-specific computational model of fluid-structure interaction in abdominal aortic aneurysms.* Med Eng Phys, 2005. **27**(10): p. 871-83.
138. Scotti, C.M., A.D. Shkolnik, S.C. Muluk, and E.A. Finol, *Fluid-structure interaction in abdominal aortic aneurysms: effects of asymmetry and wall thickness.* Biomed Eng Online, 2005. **4**: p. 64.
139. Di Martino, E.S., G. Guadagni, A. Fumero, G. Ballerini, R. Spirito, P. Biglioli, and A. Redaelli, *Fluid-structure interaction within realistic three-dimensional models of the aneurysmatic aorta as a guidance to assess the risk of rupture of the aneurysm.* Medical Engineering & Physics, 2001. **23**(9): p. 647-655.
140. Venkatasubramaniam, A.K., M.J. Fagan, T. Mehta, K.J. Mylankal, B. Ray, G. Kuhan, I.C. Chetter, and P.T. McCollum, *A comparative study of aortic wall stress using finite element analysis for ruptured and non-ruptured abdominal aortic aneurysms.* Eur J Vasc Endovasc Surg, 2004. **28**(2): p. 168-76.
141. Gosman, A.D. and E. Ioannides, *Aspects of computer simulation of liquid-fuelled combustors.* AIAA J Energy, 1983. **7**(6): p. 482-90.
142. Hinze, J.O., *Turbulence*. 1987: McGraw-Hill, New York.
143. Pope, S.B., *Turbulent Flows* 2000: Cambridge University Press.

144. Wilcox, D.C., *Simulation of transition with a two-equation turbulence model.* AIAA J, 1994. **32**(2): p. 247-55.
145. Yeleswarapu, K.K., J.F. Antaki, M.V. Kameneva, and K.R. Rajagopal, *A mathematical model for shear-induced hemolysis.* Artif Organs, 1995. **19**(7): p. 576-82.
146. Gear, A.R., *Rapid platelet morphological changes visualized by scanning-electron microscopy: kinetics derived from a quenched-flow approach.* Br J Haematol, 1984. **56**(3): p. 387-98.
147. Sims, P.J. and T. Wiedmer, *Unraveling the mysteries of phospholipid scrambling.* Thromb Haemost, 2001. **86**(1): p. 266-75.
148. Anand, M. and K.R. Rajagopal, *A mathematical model to describe the change in the constitutive character of blood due to platelet activation.* Comptes Rendus Mecanique, 2002. **330**(8): p. 557-562.
149. Silverthorn, D.U., *Human Physiology: an integrated approch*. 3rd ed. 2004.
150. Dumont, K., J. Vierendeels, R. Kaminsky, G. Van Nooten, P. Verdonck, and D. Bluestein, *Comparison of the hemodynamic and thrombogenic performance of two bileaflet mechanical heart valves using a CFD/FSI model.* Journal of Biomechanical Engineering-Transactions of the Asme, 2007. **129**(4): p. 558-565.
151. Batar, P. and G.L. Dale, *Platelet Turnover and Aging* Platelets, ed. A.D. Michelson. 2002: Academic Press.
152. Corash, L., B. Shafer, and M. Perlow, *Heterogeneity of human whole blood platelet subpopulations. II. Use of a subhuman primate model to analyze the relationship between density and platelet age.* Blood, 1978. **52**(4): p. 726-34.
153. Rissland, P., Y. Alemu, S. Einav, J. Ricotta, and D. Bluestein, *Abdominal Aortic Aneurysm Risk of Rupture: Patient-Specific FSI Simulations Using Anisotropic Model.* J Biomech Eng, 2009. **131**(3): p. 031001.
154. Sonesson, B., F. Hansen, H. Stale, and T. Lanne, *Compliance and diameter in the human abdominal aorta--the influence of age and sex.* Eur J Vasc Surg, 1993. **7**(6): p. 690-7.
155. Raz, S., S. Einav, Y. Alemu, and D. Bluestein, *DPIV prediction of flow induced platelet activation-comparison to numerical predictions.* Ann Biomed Eng, 2007. **35**(4): p. 493-504.
156. Bluestein, D., C. Gutierrez, M. Londono, and R.T. Schoephoerster, *Vortex shedding in steady flow through a model of an arterial stenosis and its relevance to mural platelet deposition.* Ann Biomed Eng, 1999. **27**(6): p. 763-73.
157. Yin, W., Y. Alemu, K. Affeld, J. Jesty, and D. Bluestein, *Flow-induced platelet activation in bileaflet and monoleaflet mechanical heart valves.* Ann Biomed Eng, 2004. **32**(8): p. 1058-66.
158. Bluestein, D., E. Rambod, and M. Gharib, *Vortex shedding as a mechanism for free emboli formation in mechanical heart valves.* J Biomech Eng, 2000. **122**(2): p. 125-34.
159. Travis, B.R., U.M. Marzec, J.T. Ellis, P. Davoodi, T. Momin, S.R. Hanson, L.A. Harker, and A.P. Yoganathan, *The sensitivity of indicators of*

thrombosis initiation to a bileaflet prosthesis leakage stimulus. J Heart Valve Dis, 2001. **10**(2): p. 228-38.
160. Leo, H.L., H.A. Simon, L.P. Dasi, and A.P. Yoganathan, *Effect of hinge gap width on the microflow structures in 27-mm bileaflet mechanical heart valves.* Journal of Heart Valve Disease, 2006. **15**(6): p. 800-808.
161. Aoyagi, S., K. Arinaga, S. Fukunaga, E. Tayama, T. Kosuga, and H. Akashi, *Leaflet movement of the ATS valve in the aortic position: Unique behavior observed in 19-mm valves.* Annals of Thoracic Surgery, 2006. **82**(3): p. 853-857.
162. Bluestein, D., Y. Alemu, I. Avrahami, M. Gharib, K. Dumont, J.J. Ricotta, and S. Einav, *Influence of microcalcifications on vulnerable plaque mechanics using FSI modeling.* J Biomech, 2008. **41**(5): p. 1111--1118.
163. Imoto, K., T. Hiro, T. Fujii, A. Murashige, Y. Fukumoto, G. Hashimoto, T. Okamura, J. Yamada, K. Mori, and M. Matsuzaki, *Longitudinal structural determinants of atherosclerotic plaque vulnerability: a computational analysis of stress distribution using vessel models and three-dimensional intravascular ultrasound imaging.* J Am Coll Cardiol, 2005. **46**(8): p. 1507-15.
164. Virmani, R., A.P. Burke, F.D. Kolodgie, and A. Farb, *Pathology of the thin-cap fibroatheroma: a type of vulnerable plaque.* J Interv Cardiol, 2003. **16**(3): p. 267-72.
165. Vande Geest, J.P., M.S. Sacks, and D.A. Vorp, *The effects of aneurysm on the biaxial mechanical behavior of human abdominal aorta.* J Biomech, 2006. **39**(7): p. 1324-34.
166. Fillinger, M.F., S.P. Marra, M.L. Raghavan, and F.E. Kennedy, *Prediction of rupture risk in abdominal aortic aneurysm during observation: wall stress versus diameter.* J Vasc Surg, 2003. **37**(4): p. 724-32.
167. Papaharilaou, Y., J.A. Ekaterinaris, E. Manousaki, and A.N. Katsamouris, *A decoupled fluid structure approach for estimating wall stress in abdominal aortic aneurysms.* J Biomech, 2007. **40**(2): p. 367-77.
168. Ricotta, J.J., J. Pagan, M. Xenos, Y. Alemu, S. Einav, and D. Bluestein, *Cardiovascular disease management: the need for better diagnostics.* Med Biol Eng Comput, 2008. **46**(11): p. 1059-68.
169. Vande Geest, J.P., D.H. Wang, S.R. Wisniewski, M.S. Makaroun, and D.A. Vorp, *Towards a noninvasive method for determination of patient-specific wall strength distribution in abdominal aortic aneurysms.* Ann Biomed Eng, 2006. **34**(7): p. 1098-106.

Appendix A – Procedures for injection of particles and extraction of particle data from Fluent Discrete Phase simulations

Creating injections for Discrete Phase Modeling (DPM)

1. Create injection plane

`Surface →Plane`

Define location of injection plane

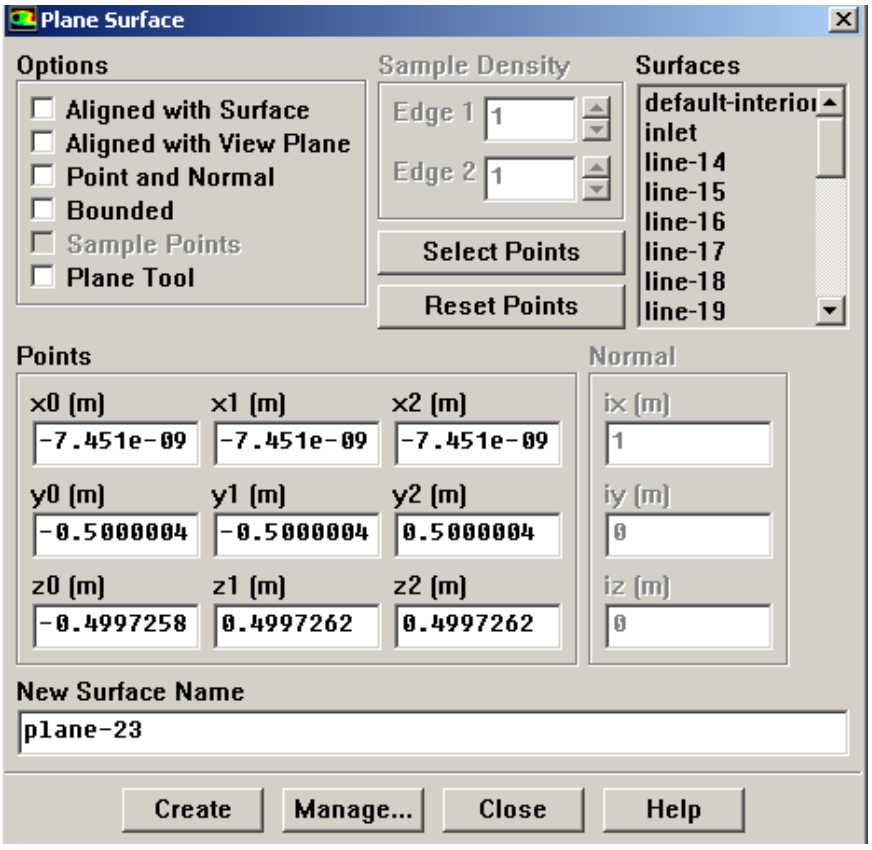

2. Create injection

`Define → Injections`

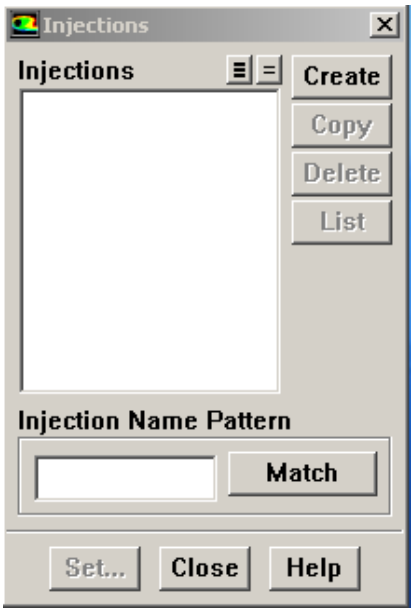

Click on `Create`

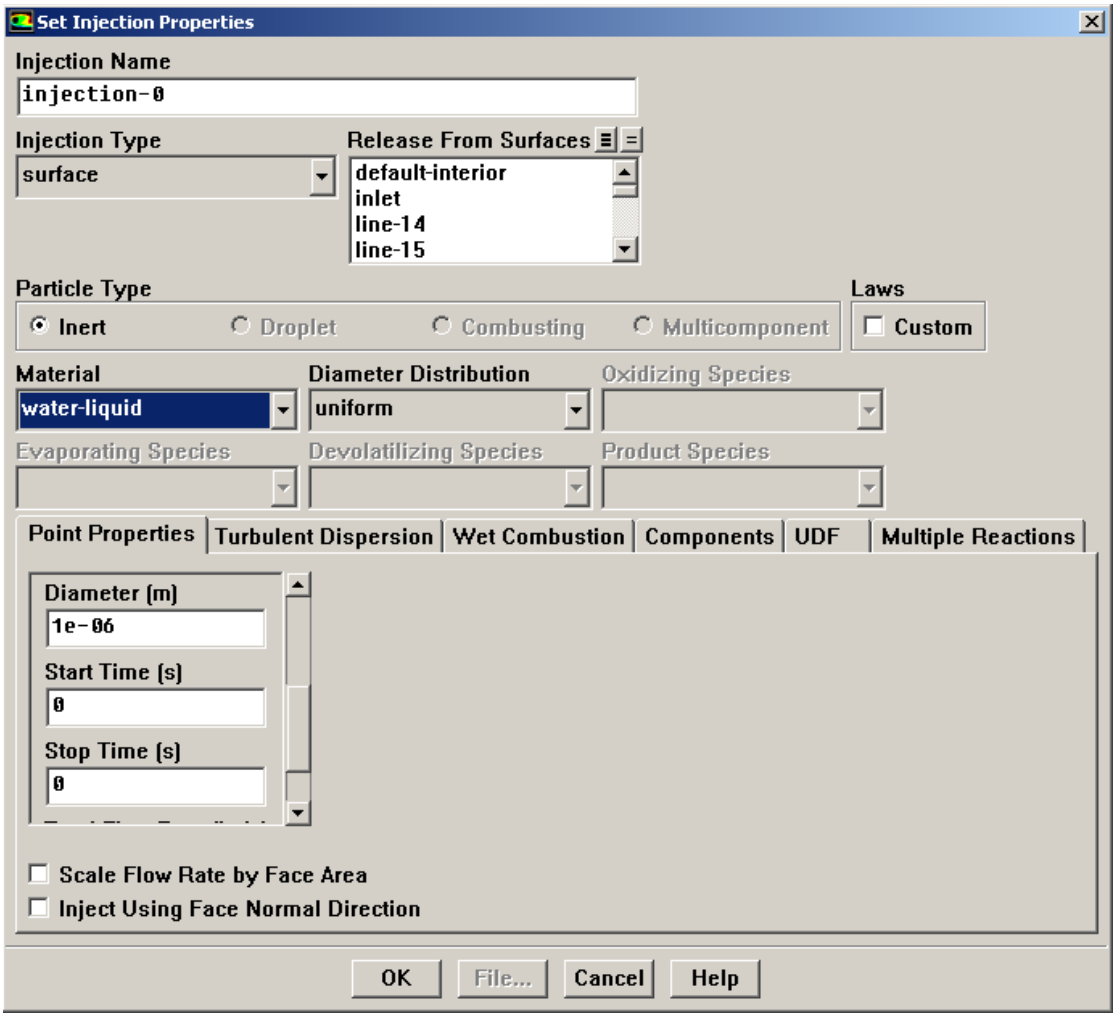

Under `Injection Type` select `surface` and choose the surface where particles are injected

Under `Material` select `water-liquid`

Under `Point Properties` define particle diameter, injection start and end times

Note: If conducting turbulent simulation, the following steps are also needed

Click the `Turbulent Dispersion` tab

Click on `Discrete Random Walk Model` under `Stochastic Tracking` section

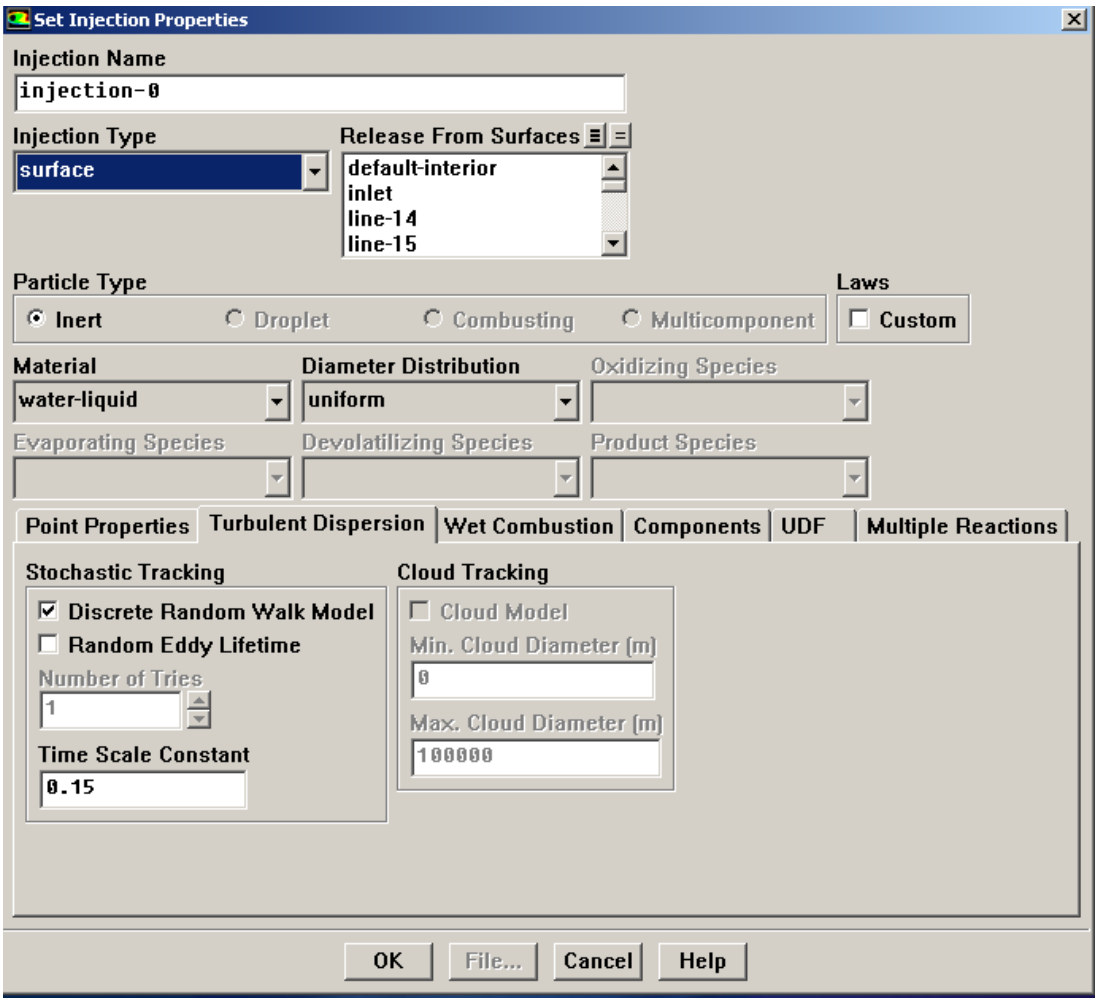

3. Define discrete phase model

`Define` → `Models` → `Discrete Phase`

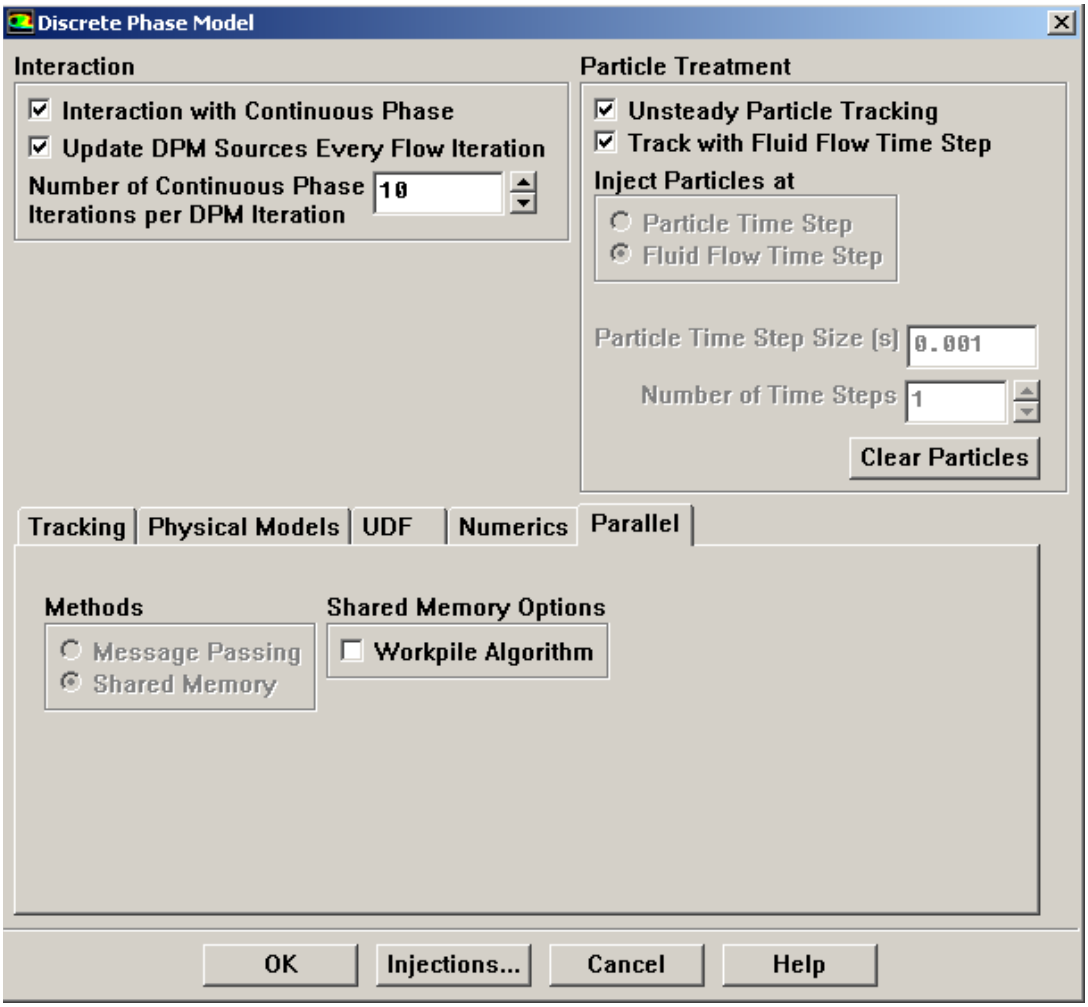

Check `Interaction with Continuous Phase`

Go to `Parallel` tab and check `Workpile Algorithm` in `Shared Memory Options`

Note: at the start of the simulation, check if the `Workpile Algorithm` in `Shared Memory Options` is still selected.

Extracting stress information

4. Incorporate “function5.txt.scm” file into .cas file

Open Fluent and the .cas file

Go to `Define` → `Custom Field Functions`

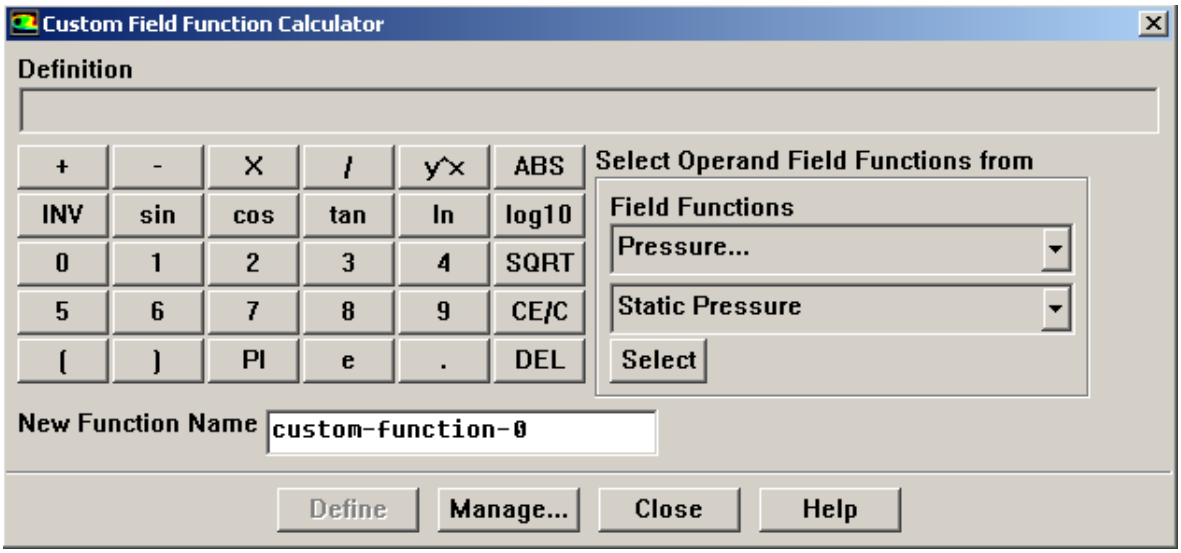

Click on `Manage`

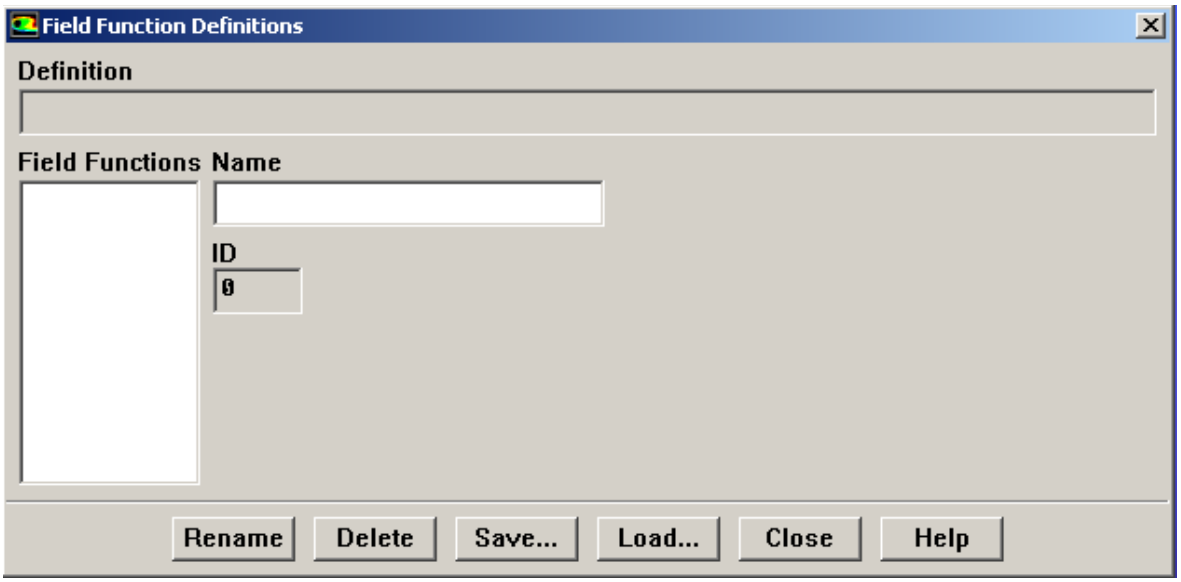

Click on `Load` to load `function5.txt.scm`

File `function5.txt.scm`, used to calculate the laminar, turbulent and total stress values for each particle.

Note: There is no need to modify this file.

The total stress tensor includes both the mean and the turbulent stresses components:

$$\bar{\tau}_{ij} = \mu\left(\frac{\partial u_i}{\partial x_j} + \frac{\partial u_j}{\partial x_i}\right) - \rho\,\overline{u_i' u_j'}$$

$\bar{\tau}_{ij}$ – stress tensor, μ – viscosity

$\frac{\partial u_i}{\partial x_j}$ – mean velocity gradient, ρ – density

$\overline{u_i' u_j'}$ – turbulent/Reynlods stress

Boussinesq approximation was substituted for the Reynolds stress component of the total stress tensor accordingly:

$$\bar{\tau}_{ij} \approx \mu\left(\frac{\partial u_i}{\partial x_j} + \frac{\partial u_j}{\partial x_i}\right) + \frac{2}{3}\rho\, k\delta_{ij} - \mu^t\left(\frac{\partial u_i}{\partial x_j} + \frac{\partial u_j}{\partial x_i}\right)$$

k – turbulent kinetic energy

μ^t – turbulent viscosity

The following two components of the tensor are given to show the general form of all tensor components.

$$\bar{\tau}_{11} \approx \mu\left(\frac{\partial u_1}{\partial x_1} + \frac{\partial u_1}{\partial x_1}\right) + \frac{2}{3}\rho\, k - \mu^t\left(\frac{\partial u_1}{\partial x_1} + \frac{\partial u_1}{\partial x_1}\right)$$

$$= \quad 2\mu\left(\frac{\partial u_1}{\partial x_1}\right) + \frac{2}{3}\rho\, k - 2\mu^t\left(\frac{\partial u_1}{\partial x_1}\right)$$

$$\bar{\tau}_{12} \approx \mu\left(\frac{\partial u_1}{\partial x_2} + \frac{\partial u_2}{\partial x_1}\right) - \mu^t\left(\frac{\partial u_1}{\partial x_2} + \frac{\partial u_2}{\partial x_1}\right)$$

The values of viscosity, turbulent viscosity, turbulent kinetic energy and components of mean velocity gradient were extracted accordingly for pertinent platelet trajectories in which the stress accumulation was computed. Components of the stress tensor were then rendered into a scalar stress value based on the formulation outlined by J. Apel et al. (Artif Organs 2001;25:341–7)

$$\sigma = \frac{1}{\sqrt{3}}\sqrt{\tau_{11}^2 + \tau_{22}^2 + \tau_{33}^2 - \tau_{11}\tau_{22} - \tau_{22}\tau_{33} - \tau_{11}\tau_{33} + 3\left(\tau_{12}^2 + \tau_{23}^2 + \tau_{13}^2\right)}$$

σ – scalar stress

5. Create journal files – similar to macro script (stress, position)

Two journal files, one for position and another for stress, are required for stress accumulation calculation. These journals are "constructed" using the following methods. The procedures outlined below are for unsteady (transient) simulations.

Stress journal construction

Load the .cas file in, and one of the data files.

Start journal file

Go to `File` → `Write` → `Start Journal`

Go to `Display` → `Particle Tracks`

Under the `Color by` option choose type of stress (laminar, turb, total) interested in extracting

In the `Release from injections`, highlight injection of interest

Under `Options`, check the `XY Plot`, and click on `Display`

Under `Options`, check the `Write to File`, and click on `Write`

Write the file (name should be in the form "stress_%t.dat"), the "%t" will be replaced by the current data file number

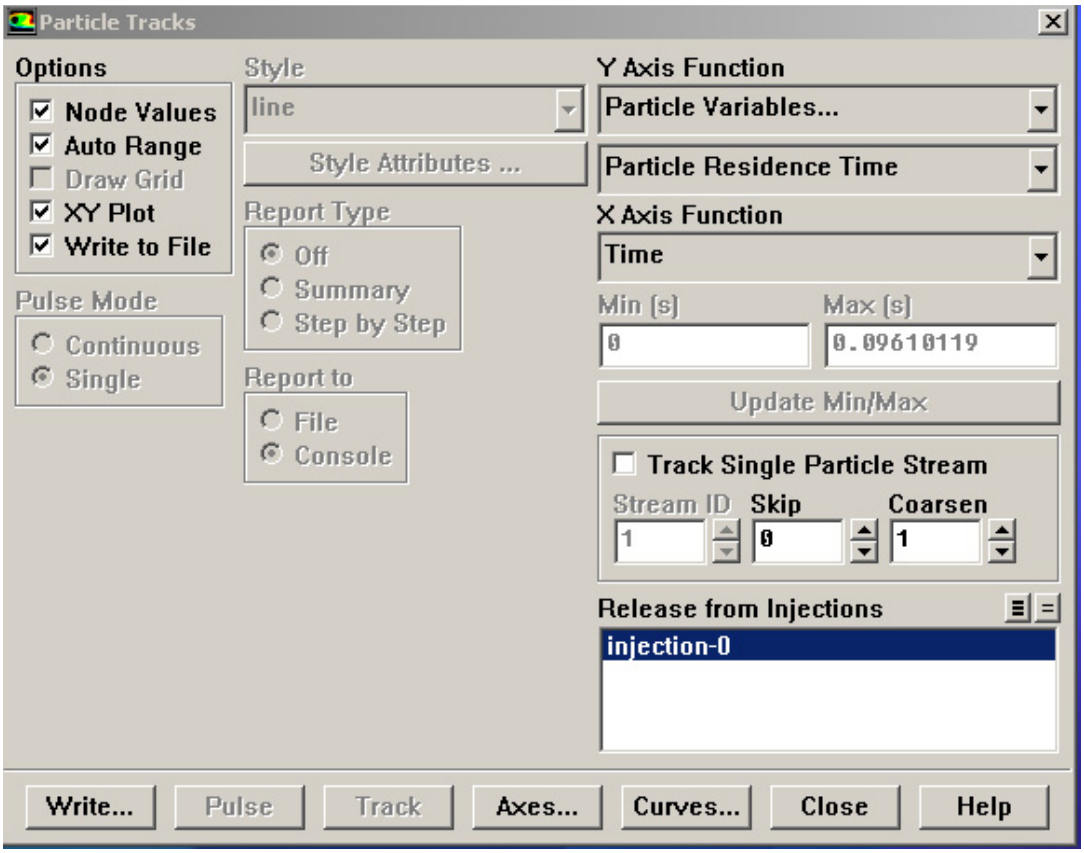

Go to `File` → `Write` → `Stop Journal`

Open the journal file in text/vi editor and remove the last line dealing with the `"stop journal"` statement.

exit from fluent

Position journal construction

Load the .cas file in, and one of the data files.

Start journal file

Go to `File` → `Write` → `Start Journal`

Go to `Display` → `Particle Tracks`

Under the `Color by` option choose `Particle Variables` and `Particle ID` from the lower drop down menu

In the `Release from injections`, highlight injection of interest

Choose `Summary` from the `Report Type` section

From the `Report to` section, choose `File`

Click on `Write` to write the file

Note: the file name is “file.part” and set by Fluent and cannot be modified

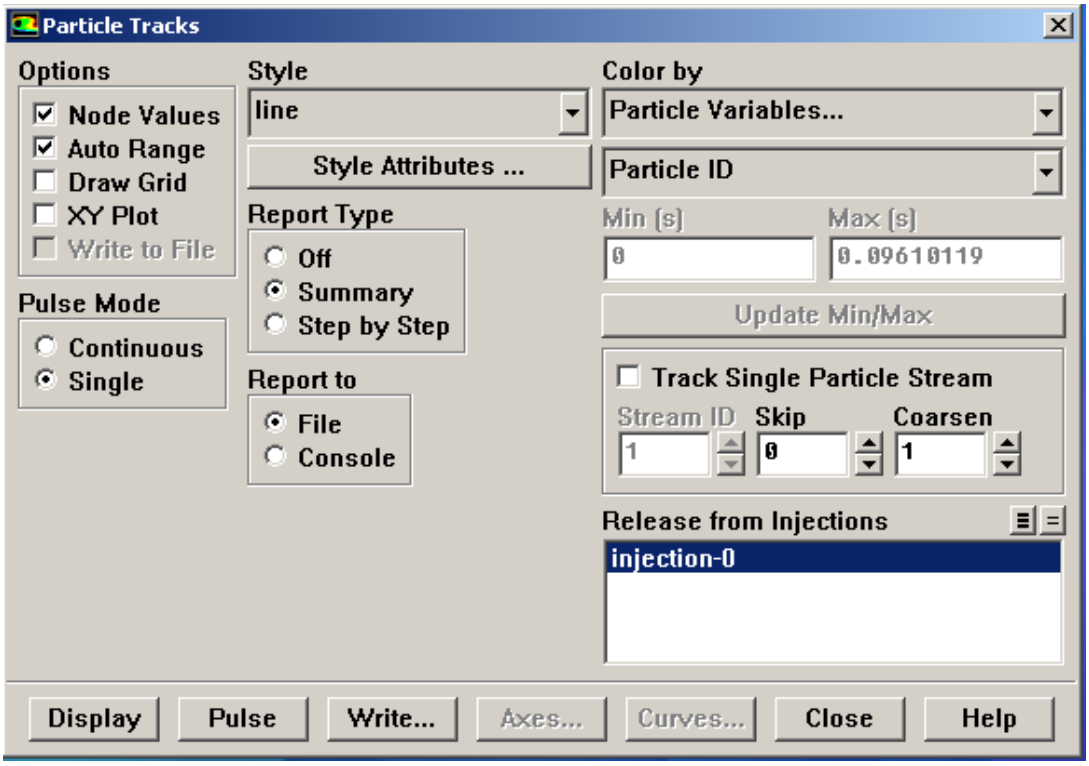

Go to `File` → `Write` → `Stop Journal`

Open the journal file in text/vi editor and remove the last line dealing with the `“stop journal”` statement.

exit from fluent

6. To (load “anim1.scm”) file in Fluent

Open the .cas file, then in the console type `(load “anim1.scm”)`

Type `(auto-animate “data_file_name” start end “journal_file_name”)`

`data_file_name` is the common repeating part of the data files

`journal_file_name` is the name of the macro-type script

`start` = start time number

`end` = end time number

File “anim1.scm”, this is animator file which is used to open and close the transient data files.

CODE	COMMENT
;; ;; Function to read (last-first) data files named ;; ;; base000first.dat.gz ;; base000......dat.ga ;; base0000last.dat.gz ;; ;; where first last are integers, base is a string and journal-file-name ;; is a journal file to create an image for animation from the data file ;; (define (auto-animate base first last journal-file-name) (if (<= first last) (begin ; Create index (string) padded with zeros (define padded-index (pad-zeros (number->string first) 4)) ; Create data file string name (define name (string-append (string-append (string-append base) padded-index) ".dat.gz")) ; Read data file (read-data name) ; Read animation journal file (ti-read-journal journal-file-name) ; Recursively call function... (auto-animate base (+ first 20) last journal-file-name)	← adjust the “pad-zeros” based on the data file names ← adjust the “auto-animate base” based on the increment data

) (begin (display "Auto-animate is done."))))	files.

For stress data extraction, run the animator and journal file as described above. For the position data extraction, it is bit more involved and requires constant watch by the user.

Note: The file name for the extracted position information is “file.part” and this needs to be changed to some other name by the user every time it is created. If not, the file will be overwritten, data lost, and animator will issue error messages.